Electrically Charged Thermal Energy Storage Systems for Grid-Level Electricity Storage

by

Laureen Meroueh

B.S., Mechanical Engineering
B.S., Civil Engineering
University of Florida, 2014

Submitted to the Department of Mechanical Engineering
in Partial Fulfillment of the Requirements for the Degree

of

Master of Science in Mechanical Engineering

at the

Massachusetts Institute of Technology

February 2018

Signature of Author: Signature redacted
Department of Mechanical Engineering
December 13, 2017

Certified by: Signature redacted
Dr. Gang Chen
Carl Richard Soderberg Professor of Power Engineering
Thesis Supervisor

Accepted by: Signature redacted
Professor Rohan Abeyaratne
Chairman, Committee for Graduate Students

Electrically Charged Thermal Energy Storage Systems For Grid-Level Electricity Storage

by

Laureen Meroueh

Submitted to the Department of Mechanical Engineering
on December 13,2017, in Partial Fulfillment of the
Requirements for the Degree of
Master of Science in Mechanical Engineering

ABSTRACT

Unlike most other commodities, electricity produced at any given time must match the electricity being consumed or the stability of the electric grid is jeopardized. Electricity demand changes throughout the day result in required generation ramp-ups that strain power plants, reduce cycle efficiency and increase CO_2 emissions. This problem is exacerbated when renewable sources such as wind and solar are integrated into the grid, due to their intermittency. A change in methods of energy production globally that allows synergistic coupling of renewable and fossil fuels is needed. Currently, pumped hydroelectric and compressed air energy storage are the two most common methods of storage, but are highly geographic dependent systems and thus of limited applicability. There exists a strong demand for grid-scale energy storage that are cost-effective and without geographic constraints. In this thesis, storage systems that are charged by electricity and discharged to produce electricity at times of high demand, are theoretically evaluated. Various types of storage such as chemical, thermal, and mechanical, are reviewed to determine the most ideal method for grid-level energy storage. Thermal energy storage systems using phase change materials are most attractive on a cost and energy density basis. Two system designs are evaluated that can couple to both existing and future power plants since they are electrically charged, via joule heating for example, and later discharged to produce electricity using the plant's turbomachinery. Described within is a novel system in which silicon is used as the storage medium and energy release is predominantly through radiative heat transfer. Another design based on the eutectic alloy $Al_{0.88}Si_{0.12}$ and other sensible energy storage materials is also evaluated. As an example, the energy storage systems are coupled to a power plant operating according to a supercritical Rankin cycle, and their performance is compared to that of a boiler. Additionally, system cost is compared to existing storage technologies. Although storing electricity as heat and back to electricity is thermodynamically unfavorable, we present an analysis to show that this approach can be cost competitive and provides a segue from fossil fuels to renewable energy.

Thesis Supervisor: Gang Chen
Title: Carl Richard Soderberg Professor of Power Engineering

Acknowledgements

To Professor Chen, for all of the late evenings spent pushing me towards understanding. I learned more within those panicked few months than I thought possible. Thank you. I look forward to our continued journey and our shared future successes.

Thank you dearest family for your unwavering support, patience, and love. I cannot fathom better role models than yourselves.

“The barriers are not erected which can say to aspiring talents and industry ‘Thus far and no farther’"—Ludwig van Beethoven

Table of Contents

Chapter 1 Introduction......15

1.1. Current State of Power Plants......15

1.1.1. Power Plant Efficiencies......17

1.1.2. Supercritical Water Power Plants......19

1.2. The Environmental Role......21

1.3. Existing Energy Storage Technologies......22

1.3.1. Batteries......22

1.3.2. Supercapacitors (Electrochemical Double-Layer Capacitor)......33

1.3.3. Fuel Cells......33

1.3.4. Superconducting Magnetic Energy Storage......34

1.3.5. Flywheel Energy Storage......35

1.3.6. Pumped Hydroelectric Energy Storage......37

1.3.7. Compressed Air Energy Storage......38

1.3.8. Thermal Energy Storage......39

1.4. Summary......42

1.5. Outline of Thesis......49

Chapter 2 Supercritical Water Power Plant Integration......52

2.1. Integration with Fossil Fuel-Fired Power Plants......52

2.2. Integration with Renewable-based Power Plants 57

2.3. Thermal Energy Storage Parameters 60

Chapter 3 Radiation Based Thermal Energy Storage 64

3.1. Introduction 64

3.2. Electrical Heating Methods 64

3.3. Molten Silicon Container and HTF Tubes 70

3.4. Non-negligible Modes of Heat Transfer 75

3.4.1. Phase Change in Silicon 78

3.4.2. Radiation versus Natural Convection 82

3.4.3. Radiation from Graphite Surface 85

3.4.4. Conduction through Membrane Wall 87

3.4.5. Radiation to Membrane Wall 89

3.4.6. Forced Convection 91

3.5. Radiation between Differential Elements 95

3.6. Approximate Heat Transfer Model during Discharge 99

3.6.1. System of Equations 101

3.6.2. Radiative TERS Performance versus Supercritical Boilers 106

3.7. Heat Transfer Analysis of Storage Conditions 108

3.7.1. Displacement Ventilation of Enclosure 111

3.7.2. System of Equations 114

3.8. System Efficiency and Dimensions 124

3.8.1. Storage Efficiency....................124

3.8.2. Unit Sizing 126

Chapter 4 Conduction based Thermal Energy Storage 129

4.1. Overview 129

4.2. Design....................133

4.3. Heat Transfer Characteristics 137

Chapter 5 Cost Analysis 141

Chapter 6 Summary and Future Work 148

Appendix....................152

List of Figures

Figure 1-1 Variation in electricity demand for state of New York over course of 4 days in February of 2017. 15

Figure 1-2. Relative efficiency of power plant with respect to relative load. 16

Figure 1-3. Capacity of subcritical, supercritical, and ultra-supercritical power plants in major countries according to study by IEA. 19

Figure 1-4. Average efficiency of coal-fired power plants including subcritical, supercritical, and ultra-supercritical generation units. 20

Figure 1-5. Energy storage technologies with respect to round-trip efficiency of the device. 44

Figure 1-6. Energy storage technologies with respect to cost of device, for upper bounds exceeding 500 $/kWh 45

Figure 1-7. Energy storage technologies with respect to cost of device, for upper bounds below 500 $/kWh 46

Figure 1-8. Energy storage technologies with respect to gravimetric energy density 47

Figure 2-1. Illustration of TERS coupled to coal-fired power plant for peak shaving, load leveling, and reduction of fuel consumption. 53

Figure 2-2. Hourly Demand Balance for state of New York.. 55

Figure 2-3. Revenue-maximizing operation of TERS in current energy market. 56

Figure 2-4. TERS charged by renewable energies 59

Figure 2-5. Thermal conductivity of silicon in solid state and liquid state 63

Figure 3-1. Typical submerged arc furnace for silicon smelting. 66

Figure 3-2. Illustration of an induction cold crucible furnace for silicon melting, adapted from Muhlbauer[109].. 68

Figure 3-3. Electrical resistance of silicon through phase change from solid to liquid. 70

Figure 3-4. Wetting process of silicon on graphite from solid to liquid phase transition. 72

Figure 3-5. Oxidation of high-impurity IG-110 graphite. 73

Figure 3-6. Waterwall configurations in typical boilers. 74

Figure 3-7. Assembly of components in radiative TERS.. 75

Figure 3-8. Illustration of various modes of heat transfer occurring during system discharge. .. 77

Figure 3-9. Illustration of heat transfer through silicon following initial simplification. 79

Figure 3-10. Illustration of length of silicon $ls(t)$. 82

Figure 3-11. Approximate heat transfer coefficient for natural convection between the contained silicon and membrane wall. 84

Figure 3-12. Energy balance of control volume analysis on contained silicon. 86

Figure 3-13. Conduction through membrane wall. 89

Figure 3-14. Energy balance of control volume analysis on membrane wall. 90

Figure 3-15. Properties of water upon transition to the supercritical state. 92

Figure 3-16. Forced convection heat transfer coefficient with respect to fluid temperature. 95

Figure 3-17. Control volume taken to perform an energy balance on contained silicon (CV_1) and fin (CV_2). 96

Figure 3-18. Geometric variables for derivation of view factor between a finite area and differential area. 97

Figure 3-19. Discretized silicon unit and membrane wall. 100

Figure 3-20. Control volume considered to approximate rate of heat transfer, Q_{1-2} , from contained silicon to membrane wall. 101

Figure 3-21. Process flow diagram implemented numerically to estimate rate of heat transfer in units of watts per meter, per control volume. 105

Figure 3-22. Contour plot of fin parameter with respect to fin thickness and length. 106

Figure 3-23. Optimized heat flux to heat transfer fluid during discharge. 107

Figure 3-24. Final design and dimensions of radiation based thermal energy storage system.. 108

Figure 3-25. Isolated system including membrane wall, silicon unit, backside insulation, and enclosure. 111

Figure 3-26. Open system harnessing buoyancy-driven flow for passive cooling during storage hours.......... 112

Figure 3-27. Parameters for buoyancy-driven displacement ventilation. 113

Figure 3-28. Path of heat transfer during hours of storage. 116

Figure 3-29. Effect of increasing resistance to conduction by microporous insulation on interface temperature with respect to firebrick thickness. 119

Figure 3-30. Effect of average fluid temperature on heat transfer. 120

Figure 3-31. Steady state temperature of air between firebrick and membrane wall, with increasing port width. 122

Figure 3-32 Example of customizable degree of feedwater preheating or hot water generation as a function of insulation barrier thickness and preheating duration. 123

Figure 3-33. Thickness of insulation and storage efficiency with varying microporous insulation thickness.......... 125

Figure 3-34. Sensitivity analysis of resulting rate of heat transfer to various parameters. 128

Figure 4-1. Schematic of latent heat thermal energy storage system commonly adopted in literature. 130

Figure 4-2. Design of thermal energy storage system utilizing liquid metal to charge the PCM, and producing superheated water vapor upon discharge. 131

Figure 4-3. Photo of HTF tubes imbedded in concrete storage system at DLR[161] 132

Figure 4-4. Heat Transfer Configurations for TERS Unit. 134

Figure 4-5. Illustration of conduction based TERS unit for solid sensible TES media or phase change materials.. 136

Figure 4-6. Illustration of conduction based TERS assembly for solid sensible or phase change storage media, designed for ease of retrofitting into existing sites... 136

Figure 4-7. Illustration of heat transfer domain considered in conduction based TERS. 138

Figure 5-1. Comparison of gravimetric energy density between energy storage media. 142

Figure 5-2. Cost breakdown of radiation based TERS having a storage efficiency of 97%. 144

Figure 5-3. Cost comparison between estimated TERS versus a variety of energy storage systems. 146

Figure A-1. Temperature gradient in fin with respect to fin parameter, $mLfin$. 153

List of Tables

Table 1. Thermodynamic Properties and Cycle Efficiency 18

Table 2. Properties of Various Battery Chemistries 32

Table 3. Main Characteristics of Sensible Heat TES reprinted from Kousksou et al.[51] 40

Table 4. Material Properties of Metal Alloy PCMs reprinted from Gasanaliev, et al.[67] 41

Table 5. Solid and Liquid Sensible Material Properties 62

Table 6. Phase Change Material Properties 62

Table 7. Radiative TERS Cost vs. Efficiency (feedwater preheating not considered) 145

Table 8. Material and Technology Cost 147

Chapter 1 Introduction

1.1. Current State of Power Plants

Two central issues can be identified that give rise to problems our electric grid currently faces: the need for dispatchable energy, and managing the periods of fluctuation in how much dispatchable energy is required throughout a 24-hour timespan, illustrated in Figure 1-1. Power plants based on sources such as coal or nuclear, i.e. baseload plants, cannot meet the fluctuating conditions of the electrical grid. Rather, another type of power plant, known as peaker plants, are used to manage peak hours of demand. These power plants normally consume natural gas as their energy supply, contribute to emissions, and can have a higher levelized cost of generation compared to cleaner energy storage systems[1].

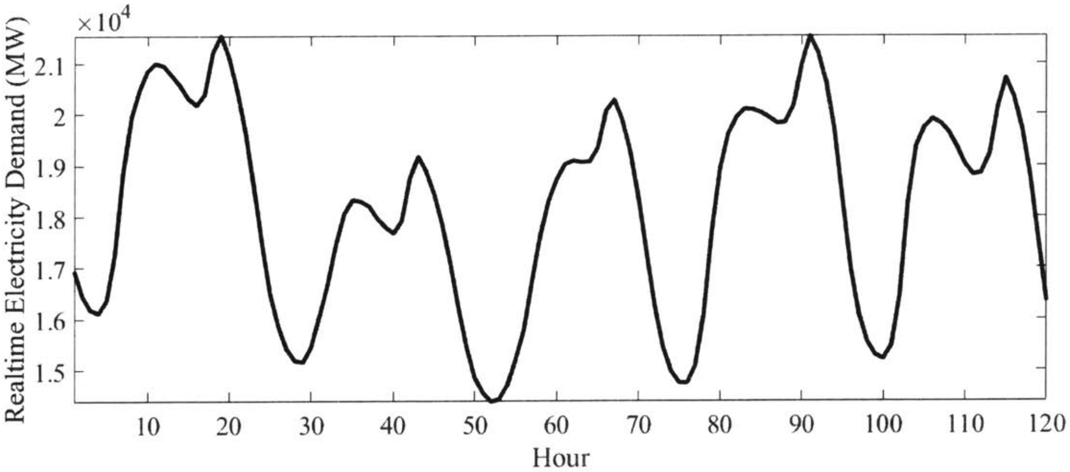

Figure 1-1 Variation in electricity demand for state of New York over course of 4 days in February of 2017. Data obtained from NYISO[2].

Although peaker plants alleviate high demand on baseload plants, baseload plants are still subject to operating at partial load and cycling. Fluctuations in energy demand throughout a day induce stress and reduced efficiency on generation units. Often, plant operators must operate generation units at minimal capacity during periods of low demand to avoid the cost of start-ups, thus emitting CO_2 at unnecessary cost to our environment. Operation of boilers at minimal capacity also contributes to thermal stress on the system, considering base-load boilers were designed to operate continuously at maximum rated capacity[3–5]. Bergh et al. studied the effect of partial load operation on efficiency for different types of power plants, with the resulting trends from his study provided in Figure 1-2[6].

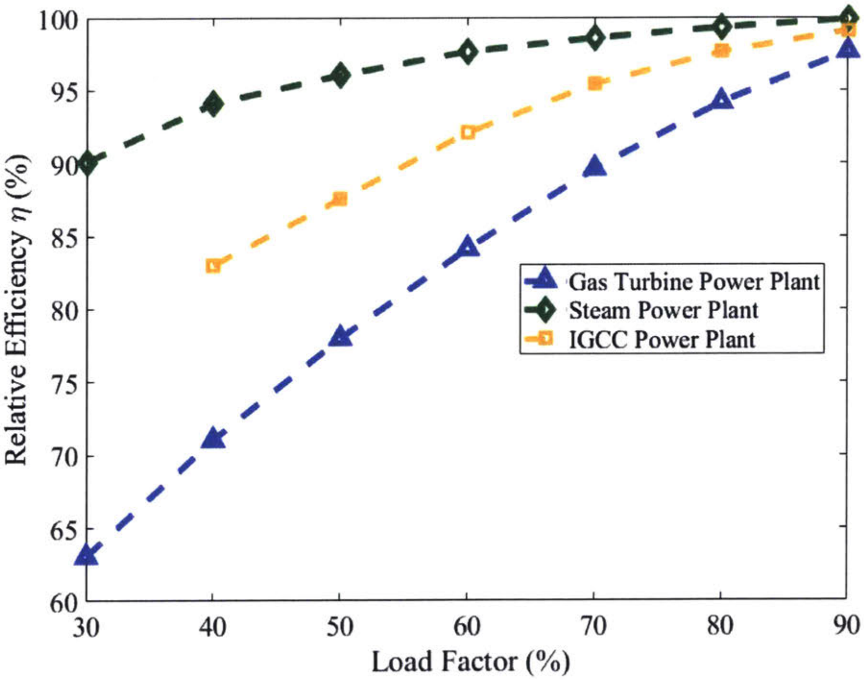

Figure 1-2. Relative efficiency of power plant with respect to relative load. Load factor refers to the output relative to the maximum rated capacity. IGCC stands for integrated gasification combined cycle (IGCC) using both gas turbine and steam turbine. Data adapted from Bergh et al[6–8].

Renewable energies, such as wind and solar thermal or solar photovoltaics, introduce further aggravation upon the grid due to the intrinsic intermittency of these sources. Oversupply of electricity generated during peak hours has led to negative pricing in some regions[9–12]. In other regions, there is a mismatch between hours in which renewable energies are most available and hours of peak electricity demand[13]. Beyond hourly demand balancing, energy stored for durations on the order of months is attractive. Because the earth does not revolve around the sun in a perfectly circular path, and its axis of rotation is tilted with respect to earth's orbit about the sun, the intensity and distribution of solar radiation incident upon earth's surface varies over the course of a year. Hence, seasonal energy storage is of great interest for year-round utilization of solar energy.

1.1.1. Power Plant Efficiencies

Fossil fuel power plants operating on the Rankine cycle have been increasing their efficiency since the 1950's with the introduction of superheated and supercritical steam[14]. Governing the efficiency (η) across all power plants, irrespective of energy source, is the Carnot efficiency for ideal heat engines, $\eta = 1 - T_L/T_H$, where T_L is temperature of the cold reservoir, and T_H is temperature of the hot reservoir, which conveys the simple relation of higher working fluid temperatures leading to higher efficiencies. Considering mechanical components of the power cycle, specifically turbines, have essentially reached the maximum efficiency attainable[15], other methods of increasing overall plant efficiency are sought after. Thus, the temperature of the fluid fed into steam turbines has been progressively increasing with the development of materials that can withstand such high temperatures without loss in structural integrity.

Supercritical water power plants operate with pressures around 250 bar and temperatures of 540-560°C, resulting in efficiencies as high as 50% under ideal conditions[16,17]. Ultra-supercritical water power plants operate at even higher temperatures and pressures, upwards of 580°C and 250 bar, respectively. Given such thermodynamic conditions, ultra-supercritical plants have potential to reach efficiencies greater than 54% under ideal conditions, yet have not been implemented to the extent that supercritical plants have due to the higher cost of materials that can withstand such temperatures[17,18]. Supercritical CO_2 Brayton cycles are also gaining attention due to the high temperatures such cycles can reach, over 600°C, and corresponding high efficiencies around 50%[19,20]. The thermodynamic cycle with the highest practical efficiency is that of an integrated gasification combined cycle (IGCC) using both gas turbine and steam turbine, able to achieve efficiencies around 60%[21]. A summary of thermodynamic conditions and efficiencies of common cycles are provided in Table 1.

Table 1. Thermodynamic Properties and Cycle Efficiency

Power Plant Cycle	Thermodynamic Properties	Plant Efficiency under Ideal Conditions
Subcritical Steam Rankine Cycle	$P<220$ bar, T up to 565°C	$\eta \approx 46\%$
Supercritical Water Rankine Cycle[16,17]	$P \sim 250$ bar, $T = 540\text{-}560$°C	$\eta \approx 50\%$
Ultra-supercritical Water Rankine Cycle[17]	$P \sim 250$ bar, T upwards of 580°C	$\eta > 54\%$
Supercritical CO_2 Brayton Cycle[19,20]	$T > 600$ °C	$\eta \approx 50\%$
Integrated Gasification Combined Cycle with both gas and steam turbine[21]		$\eta \approx 60\%$

1.1.2. Supercritical Water Power Plants

Coal remains to be the largest source of public power generation in most countries, including China, the United States, India, Germany, the UK and Ireland, Korea, and Australia[22]. Many countries continue to see growth in coal-fired generation and although from a global perspective current deployment of supercritical and ultra-supercritical technologies is low relative to subcritical units (Figure 1-3, adapted from IEA[23]), supercritical technologies are rapidly populating coal-fired fleets, especially in China[17].

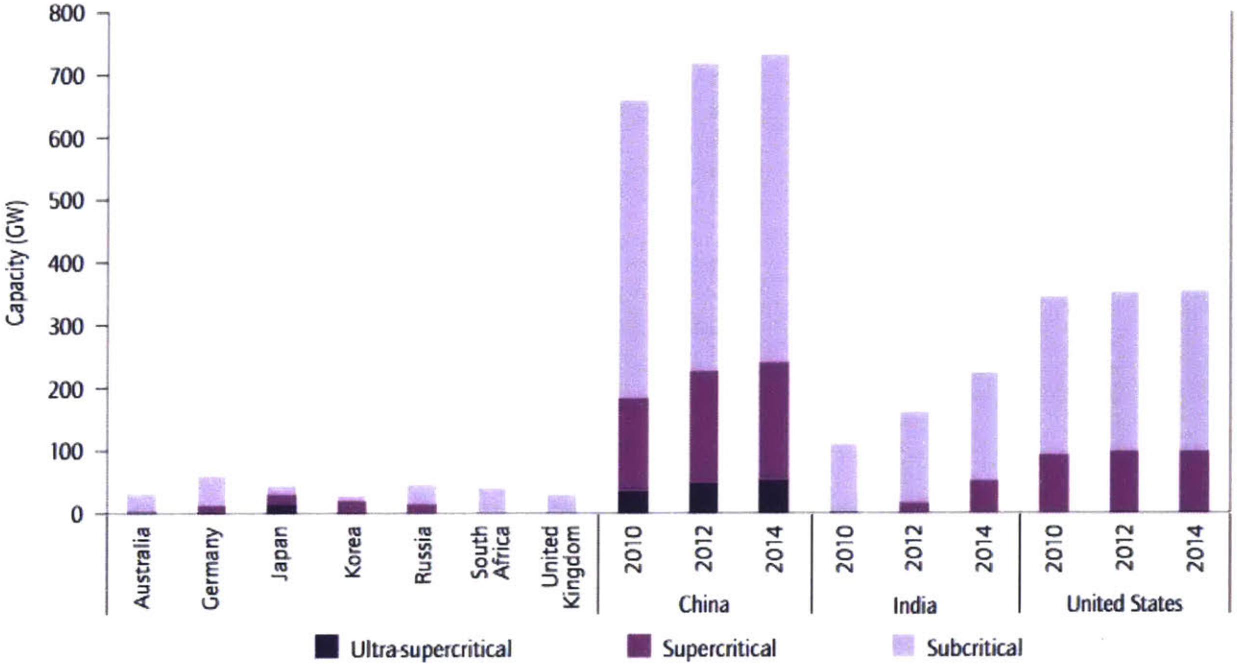

Figure 1-3. Capacity of subcritical, supercritical, and ultra-supercritical power plants in major countries according to study by IEA. Japan and South Korea own the majority of supercritical and ultra-supercritical power plants (over 68%) out of all countries shown. Figure adapted from IEA, data by Platts[23,24].

This increase in supercritical technologies has resulted in increase of coal-fired power production efficiencies in many countries. For example, Japan and Korea's supercritical power plants have average efficiencies greater than 40% on a lower heating value (LHV) basis[17]. An efficiency of 41.5% can readily be achieved by supercritical power plants[25,26]. France has an average coal-fired power efficiency of 43% including subcritical, supercritical and ultra-supercritical plants[22]. Ultra-supercritical power plants have already achieved high efficiencies in practice, such as the Yuhuan, Skaerbaek 3, Nordjylland, and Avedore power plants with efficiencies from 47-49%[16,27]. A summary by ECOFYS of average coal-fired power efficiency is provided in Figure 1-4[22].

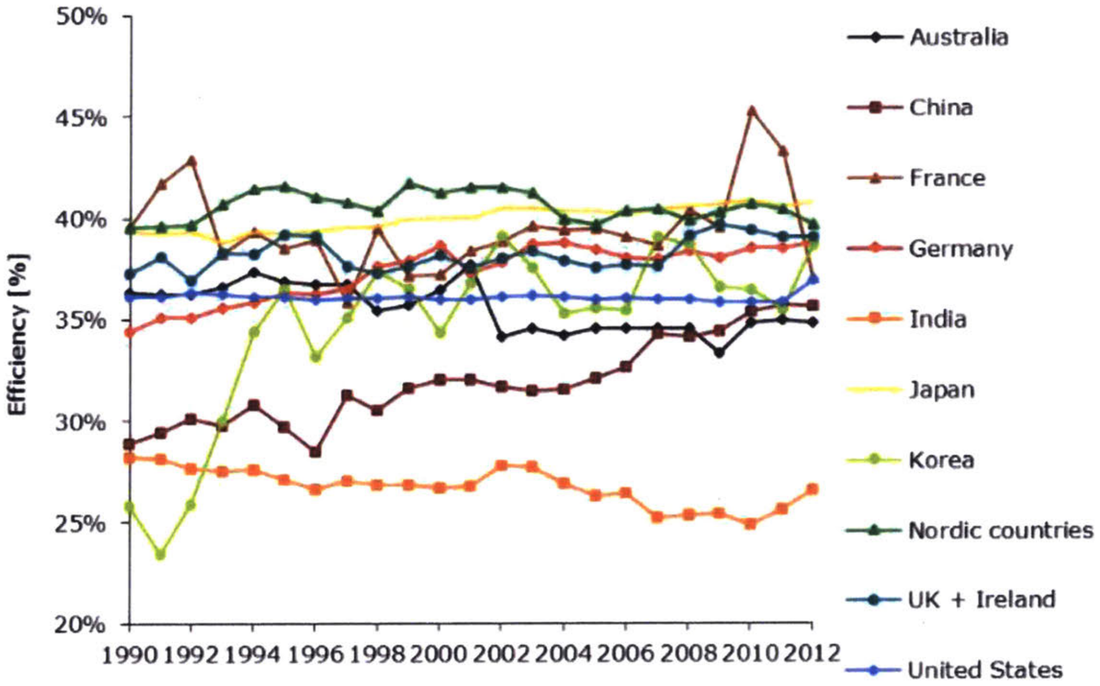

Figure 1-4. Average efficiency of coal-fired power plants including subcritical, supercritical, and ultra-supercritical generation units. Figure adapted from ECOFYS[22].

1.2. The Environmental Role

The detrimental effects that carbon dioxide (CO_2) emissions are imparting upon our planet are well recognized[28–34]. Though implementing new policies could lead to a decrease in future CO_2 emissions than would occur under current policies, an increased rate in emissions has nevertheless been predicted by the year 2035 compared to the current rate[35]. The Paris climate accord is also motivating an effort towards further change in our methods of global energy production. The introduction of renewable energy into the grid has indeed helped, however renewables inherently have problematic characteristics that must also be addressed. Accordingly, we pursue a more sustainable framework for energy production that can be met by both developed countries as well as fossil-fuel-dependent developing.

The causal relation between CO_2 emissions and economic growth can explain temporal trends of CO_2 emissions, albeit to different degrees depending upon region of interest. As countries in the Organization for Economic Cooperation and Development (OECD) work to meet the standards set by the Kyoto Protocol, countries outside of the OECD are in fact increasing their coal consumption and CO_2 emissions. Jinke et al. studied the trends and effects of OECD and non-OECD countries versus economic growth, concluding a unidirectional causality between GDP and coal consumption in, but not limited to, Japan and China[36]. Thus, it is simply unrealistic to perceive the global switch from fossil fuels to renewable technologies as a near-term achievable goal, in agreement with the principle of "Common but Differentiated Responsibility and Respective Capabilities". This principle is also acknowledged in the Paris Agreement. Rather, we introduce a system that will mitigate the amount of fossil fuel consumption necessary without jeopardizing the economic growth of such countries. This is possible by a system that is electrically charged, capable of coupling to both existing fossil-fuel fired power plants and renewable energy-based power plants. It should be emphasized that such an energy storage system is not limited to coal-fired plants, the example case in this study. Gas powered plants and nuclear power plants can similarly gain benefits from the storage system described herein.

1.3. Existing Energy Storage Technologies

Various energy storage technologies have been developed; however the main factor affecting wide scale application of these technologies for grid-level energy storage is cost. Nevertheless, there are other important characteristics that contribute to the feasibility of an energy storage technology being applied. Such characteristics include the necessity of high durability and reliability, long life, resistance to cycling, and high round-trip efficiency. Each energy storage technology discussed has its respective advantages and disadvantages, described in this review, and thus may be suitable for certain applications where a differing technology is not. A comprehensive review of energy storage technologies, including those still under research and those already implemented, is performed to determine which energy storage method to pursue. Following the description of all technologies, a summary of key properties is provided, including efficiency, energy density, and cost.

1.3.1. Batteries

Batteries, or electrochemical accumulators, store electricity in the form of chemical energy, alternating between charge and discharge phases to store and release electricity. The discharge phase consists of redox reaction of electrodes converting the stored chemical energy into electrical energy, with the reverse process occurring during the charging phase. An electrochemical cell consists of two half-cells, each with an electrode and electrolyte, which transfer electrons through the electrode via oxidation-reduction reactions. The main advantages of batteries include high energy densities, flexible power and energy characteristics, low maintenance, and pollution-free operation. The main disadvantage of batteries is their low durability when subject to large-amplitude cycling, and contribution to pollutions during the manufacturing process.[37] Following a brief overview of various types of batteries, a summary of properties is provided in Table 2.

1.3.1.1. Lithium-ion

Lithium ions in lithium-ion (Li-ion) batteries move between the anode and cathode to produce a current, with concomitant oxidation and reduction processes occurring at the two electrodes. The electrical energy is stored in electrodes made of Li-intercalation compounds.[38] The advantages of Li-ion batteries include energy-to-weight ratio, long cycle life and rate capability, no memory effect, and low self-discharge. The benefits of the Li-electrochemistry that induced interested in Li-ion technologies are low molecular weight, resulting in use for portable applications; small ionic radius, benefiting diffusion; and high cell potentials and thus high-energy densities. Due to the high energy density of Li-ion batteries, they are currently being used for electric vehicles. Recent testing of the Li-ion battery for stationary applications most prominently implements a battery pack unit consisting of 6-8 prismatic cells with or without an integrated cooling system, depending on the size of the energy storage.[38]

Compared to Ni-Metal Hydride (Ni-MH) or Ni-Cd batteries, Li-ion batteries have double the energy density on a per kilogram basis. Furthermore, the ratio of specific energy density to specific power density of Li-ion batteries exceed that of Ni-MH, Ni-Cd, and lead-acid by at least a factor of 2.5, indicating superior performance of delivered energy at high specific power.[39]

The cost of Li-ion batteries remains an issue and hindrance to application for medium- and large-scale energy storage. Currently, the cost of the Tesla Powerpack with a 200 kWh (kilo-Watt hour) capacity is around ~\$400[40]. Li-ion batteries based on $LiFePO_4$ have gained attention due to attractive cost and safety features. Nonetheless, the limited lithium resources will increase raw material costs. Furthermore, the internal resistance produces internal heat-up and failure, thus requiring a battery management system to couple with the Li-ion battery system.[41]

1.3.1.2. Lithium-air

Lithium-air batteries convert chemical energy in lithium and oxygen into electrical energy during discharge. Lithium is the anode while oxygen is the cathode. The electrical energy is stored by the splitting of $Li-O_2$ discharge products. As of now, Li-air batteries still have a considerable amount of research and development before commercialization, though have at least been proven on a laboratory scale. The most common application suggested for Li-air batteries is that of replacing Li-ion batteries in electric vehicles[42,43]. Li-Air batteries are deemed impractical for grid-level energy storage due to their low power density, poor cycling capability, and low energy efficiency[39].

1.3.1.3. Lithium-Sulfur

Lithium-sulfur (Li-S) batteries seem attractive due to the advantageous characteristics of elemental Sulfur, such as abundance low cost, and a 3-5 fold higher theoretical energy density compared to Li-ion. Because of this higher density, efforts have gone into addressing the fundamental challenges with Li-S batteries such as understanding sulfur redox chemistry and speciation in the cell[44,45]. However, Li-S batteries are still far from application in grid-level energy storage due to poor cyclability, low coulombic efficiency, and current lack of a scalable approach to the materials design, among other issues.[42,45]

1.3.1.4. Sodium-Sulfur

Sodium Sulfur (Na-S) batteries are a high-temperature battery that reversibly charge and discharge electricity through sodium ion transport across a β"-Al_2O_3 solid electrolyte that is doped with Li^+ or Mg^{2+}.[38] The β-alumina ceramic tubes are the key to determining the battery operation and cost. Although large-scale production of β-alumina has been established, production yields and costs remain major concerns. The Na-S chemistries are quite mature, first being developed in the late 1960s. Various MWh systems have been demonstrated on the electrical grid. The world's largest energy storage system uses Na-S, with a power rating of 34MW and total reserve capacity of 238 MWh, designed to support a 51MW wind farm in northern Japan.[46,38] Na-S batteries appear to be an economic option for both power quality and peak shaving.[47]

Currently, Na-S ranks highly amongst the various battery technologies. Advantages of Na-S batteries include high power and energy density, high coulombic efficiency, good temperature stability, low maintenance requirements, long cycle life, quick reversibility between charging and discharging, and suitability for high volume mass production. Na-S batteries have a cycle life of up to 2500 cycles at 100% depth of discharge, and up to 5000 cycles at 90% depth of discharge.[46] The discharge power rating is high and comparative to that of flow batteries and lead acid batteries, being up to 10MW for several hours. In operation lifetime, Na-S batteries surpass lead-acid batteries,, being able to operate daily for as long as 15 years, with an energy density comparable to lead-acid. The cost of Na-S is expected to decrease as production increases.

A possible disadvantage of Na-S batteries is that they must be heated externally to 300°C-360°C for optimal operation. However, when coupled with solar thermal energy, this can be easily achieved. Furthermore, the safe operation and cost reduction of Na-S batteries requires integration of scientific advancements to create new electrode architectures and chemistries.[39]

1.3.1.5. ZEBRA: Sodium Nickel-Chloride

The most common and commercialized ZEBRA battery is a battery that operates on the Na-$NiCl_2$ chemistry, where ZEBRA stands for Zero-Emission Battery Research Activities. These Na-$NiCl_2$ ZEBRA batteries have gained prominence due to the advantages they have over Na-S batteries. Compared to Na-S batteries, Na-$NiCl_2$ ZEBRA batteries have a higher cell voltage, better safety characteristics, low operating temperature, and ability to withstand overcharge and discharge. Disadvantages compared to Na-S batteries include its lower power and energy density. Further disadvantages include high cost and self-discharge issues. The Na-$NiCl_2$ ZEBRA battery may only be produced by the company Beta R&D in the UK, which has been continuously developing improved versions of the ZEBRA for various applications.[48] In order to make the Na-$NiCl_2$ ZEBRA battery a largely promising energy storage system for large-scale stationary energy-storage, the cost must be reduced and the cycle life must be improved. The technology is currently used for electric vehicles and submarines.[47]

A novel ZEBRA battery based on Na-$FeCl_2$ has been studied that aims to mitigate some of the disadvantages incurred with Na-$NiCl_2$, such as high cost. The main source of high cost for Na-$NiCl_2$ cells is the cathode material, Ni. By replacing Ni with Fe in the cell, a cost reduction of 61% is estimated. The Na-$FeCl_2$ battery uses polysulfide additives to allow for inexpensive pretreatment and discharged state assembly processes for the cathode at intermediate temperatures. The performance results of the Na-$FeCl_2$ ZEBRA battery includes high overall energy efficiency >92%, sustainable battery performances, promising output voltages, and inherent safety.[49]

1.3.1.6. Lead-Acid Battery

Lead-acid batteries are the most technologically mature of all rechargeable batteries. A lead-acid (Pb-acid) battery cell is composed of lead dioxide as the active material at the anode, Pb as the negative active material, sulfuric acid as the electrolyte, and Pb as the current collector. During discharge, both electrolytes are converted to lead sulfate, with the reverse occurring during charging.[41] A valve-regulated design has been introduced to the lead-acid battery, leading to the valve-regulated lead-acid (VRLA) battery. The VRLA battery, compared to traditional lead-acid batteries, offers reduced maintenance, reduced footprint, and improved performance.[38]

Although the lead-acid battery is most mature, numerous disadvantages restrict the use of lead-acid batteries for grid-level energy storage. Lead-acid batteries have a limited cycle life, low energy density due to the lead current collectors, poor low-temperature performance, are difficult to transport due to being heavy and bulky, and require maintenance due to the corrosion of lead. Lead specifically presents numerous hazards to the environment, including pollution, explosions, poisoning, etc[50]. Furthermore, like lithium but to a more severe degree, the world supply of lead is limited and thus lead-acid batteries are not a sustainable solution.

1.3.1.7. Lead-Carbon UltraBattery

A lead-carbon (PbC) battery is an evolved version of a lead-acid battery, with the lead-anode replaced to some degree by carbon for improved performance and reduced life-cycle cost. An ultrabattery is a PbC battery with a split negative electrode, half of it as lead and the remaining half as carbon. The PbC ultrabattery combines a Pb-acid battery and PbC asymmetric supercapacitor into one unit.

Ultrabatteries exceed discharge power behavior of lead-acid batteries by 50%, and charge power by 60%. They also have a longer life cycle than lead-acid batteries, lasting roughly 2.7 times longer than traditional Pb-acid batteries. Ultrabatteries are currently commercialized but testing must be performed to determine the length of a deep cycle life.. Disadvantages of the ultrabattery include high capital cost and slow ramp rate[38].

1.3.1.8. Nickel-Cadmium Battery

Nickel-Cadmium (NiCd) batteries use nickel oxide hydroxide as the positive electrode and metallic cadmium as the negative electrode, immersed in an electrolyte.

NiCd batteries are advantageous over lead-acid batteries due to their higher energy density, robustness to deep discharges, and longer cycle life. Nonetheless, NiCd batteries are far more expensive than Pb-acid and remain inferior to Li-ion and Nickel-metal hydride (NiMH) chemistries. Compared to NiMH, NiCd batteries have a short life cycle, more pronounced memory effect, complex recycling procedure, low energy density, and thermal runaway issues in voltage-controlled charging.[41] Furthermore, the cost of NiCd batteries resultant to expensive manufacturing processes is a major drawback, at ~1000$/kWh as of 2008.[48] NiCd batteries are most suitable for portable and few industrial applications, which require high power output, however the high environmental hazard of NiCd batteries must be considered.[51]

1.3.1.9. Nickel-Metal Hydride Battery

Nickel-Metal hydride (NiMH) batteries use nickel oxide hydroxide as the positive electrode and a hydrogen-absorbing alloy as the negative electrode.

NiMH batteries have recently gained more attention over NiCd batteries due to their energy density, performance and environmental advantages compared to NiCd batteries. NiMH batteries are currently being applied to electric vehicles due to their high energy density.

Advantages of NiMH include a high power density, proven safety, good abuse tolerance, and long life cycle at a partial state of charge.[41]

Disadvantages of NiMH batteries include high self-discharge, hydrogen buildup, which can cause cell rupture, and capacity reduction if overdischarged. NiMH batteries are not a suitable option for long term energy storage due to their high self-discharge rate.[51]

1.3.1.10. Redox Flow Batteries

Redox flow cells use two circulating soluble redox couples as the electroactive species that are oxidized and reduced to store or deliver power. Unlike many electrochemical energy storage systems, flow batteries decouple total stored energy from rated power, allowing the flow batteries to provide large amounts of power and energy required by utilities. The system power is determined by the size of cell stacks, while the system capacity is determined by the size of the electrolyte tanks.

Advantages of redox-flow batteries include high and flexible power and energy capacity, fast recharge by replacing exhausted electrolyte, long life cycle enabled by easy electrolyte replacement, full discharge capability, use of nontoxic materials, and low temperature operation. Furthermore, the fact that power and energy are decoupled allows design flexibility with respect to capacity and power. The low cost of redox-flow batteries is enticing but application requires further development of the technology. [41,52]

Unlike Na-S and lead-acid batteries, redox-flow batteries are relatively new and in the early stages of development. There have been very few field tests and currently have limited solubility, contributing to the low energy density of 25 Wh kg^{-1}. Currently, Vanadium redox battery (VRB) and Polysulfide-bromine flow battery are the most mature of flow batteries and have been tested for stationary energy storage, with VRB's going onto peak shaving, load-leveling and renewable storage installations [53,54]. VRB Disadvantages of redox-flow batteries include the requirement of pumps, thus possibilities of mechanical failures, limited concentration of redox couples leading to low energy densities, low power density, and lack of an appropriate membrane for controlling long-term ion cross-over effects.[39]

Recently, a semi-solid lithium redox-flow battery has been developed, with much higher energy densities than typical redox-flow batteries, and lower cost of manufacturing compared to lithium-ion batteries. A very preliminary systems-level estimate of cost results in \$40-\$80 kWh^{-1} for the active materials and electrolytes, not including manufacturing costs. This figure is indeed attractive compared to existing batteries, though other types of storage such as thermal can achieve even lower cost [39,55].

In summary, flow batteries have been deemed suitable for long-term storage due to their high-power and high-capacity discharge, rapid and deep cycling, and low operating costs when idle. Specific services that flow batteries could provide include voltage and frequency regulation, load leveling, and peak power support.[51]

Table 2. Properties of Various Battery Chemistries

Battery Chemistry	Efficiency %	Energy Density (Wh/kg)	Power Density (W/kg)	Operating Temp °C	Cycle Life (cycles)	Durability (years)	Self Discharge (20°C)	Maturity	Power (MW)	Discharge duration	Capital Cost ($/kW)	Cost Bounds ($/kWh)	
												lower	upper
ZEBRA Na-NiCl2	75-90	100-140	130-245	300-350	3,000 deep; 2,500-3,000	8-14	15% per day	Demo.	0.001-1	mins-8hrs	150-300	100	200
ZnBr Flow	75-80	60-85	50-150	-	~2000	5-20	-	Dev.	0.025-1	up to 4hrs	700-2500	150	1000
Vanadium Redox	65-85	10-75	-	10 to 40	5,000 deep; >13,000	10-20	3-9% per month	Demo	0.005-1.5	up to 8hrs	600-1500	150	1000
Lead Acid	70-90	30-50	75-300	-40 to 60	500-1,000 deep cycles	5-15	4-50% per month	Mature	0-40	up to 8hrs	300-600	200	400
NaS	75-90	150-240	150-230	300 to 350	4,000 deep; 2,000-5,000	15	negligible	Comm.	0.05-34	5-8 hrs	1000-3000	300	500
Fe/Cr Redox Flow	75	-	-	-	>10,000	-	-	R&D	1	4 hrs	1200-1600	300	400
Zn/Air	75	1086	-	-	4500	-	-	R&D	1	5.4 hrs	1750-1900	325	350
Li-Ion	85-90	75-200	100-5000	-	1,000-10,000	5-20	0.1-0.3% per day	Demo.	0.1-50	0.1-5 hrs	1200-4000	500	2500
Lead-carbon ultrabatteries	-	25-40	-	-40 to 60	3000 deep	-	-	Comm.	-	up to 4 hrs	-	500	
Advanced Pb-Acid	75-90	-	-	-	4500	-	-	Demo.	1 to 12	3.2-4 hrs	2000-4600	625	1150
Ni-Cd	60-70	50-75	140-180	-10 to 45	2,000 deep; 1,000-2,500	10-20	5-20% per month	Comm.	0-40	up to 4 hrs	500-1500	800	1500
Li-ion Carbon anode LiCoO2 cathode	94-99	155	-	-25 to 40	1,000 deep	-	2% per month	R&D	-	up to 4 hrs	-	900	1700
Li-ion Li4Ti5012 anode LiFePO4 cathode	94-99	50-70	-	-25 to 40	4,000 deep	-	2% per month	R&D	-	up to 4 hrs	-	900	1700
Ni-MH	60-66	30-110	250-2000	-	200-1,500	3-15	High	Dev.	0.01 to 1	secs to hrs	-	-	-
Li-Polymer	70	200	250-1000	-	>1,200	-	Medium	-	-	-	-	-	-

Sources: ZEBRA[38,47–49], ZnBr Flow[39,47], Vanadium Redox[38,47], Lead Acid[38,47,51,62], NaS[38,47], Fe/Cr Redox[39], Zn-air[39,75], Li ion[41,47,62], Lead-carbon ultrabattery[38], Advanced Pb-Acid[39], Ni-Cd[38,41,51,62], Li-ion variations[38], Ni-MH[41,47], Li-polymer[41]

1.3.2. Supercapacitors

Supercapacitors, formerly known as electrochemical double-layer capacitors (EDLCs), store energy in the electrochemical capacitor by simple charge separation, thus no Faradic processes occur. Supercapacitors can store a relatively large amount of energy at the collector surface by using porous carbon as the current collector, maximizing the electrode surface area.

Advantages of supercapacitors include high capacitance ratings, long cycle life due to lack of chemical changes on the electrode, high efficiency and power density, and low-voltage-withstand capability. They are specifically attractive for voltage regulation, uninterruptible power supplies, hybrid vehicles, and high-power applications that require very short discharge durations. However, supercapacitors have low energy density, high cost, high self-discharge rate, and their ability to be completely discharged gives rise to the possibility of large voltage swings .[41,51]

1.3.3. Fuel Cells

Fuel cells have gained more attention with the proposed hydrogen economy, in which hydrogen is stored as a gaseous fuel to generate electricity for future needs. Fuel cells (FCs) are electrochemical conversion devices that produce water and electricity through the consumption of hydrogen and oxygen. Regenerative fuel cells combine the function of a FC and electrolyser into one device. Technologies based on hydrogen storage are highly applicable for load shifting applications, however they are currently too expensive for implementation and have a low round trip efficiency.[51]

Regenerative FCs reduce system size of an energy storage and production system, and have a high energy density. However, regenerative FCs remain costly. Furthermore, similar to conventional FCs, regenerative FCs experience life degradation in dynamic applications. To minimize these effects, regenerative FCs are coupled with EDLCs or other energy storage systems.[41]

The main issue with unitized regenerative fuel cells (URFC) is their high cost due to the use of platinum group metal catalysts, required by the proton exchange membranes (PEMs) employed in URFC. A low-temperature unitized regenerative fuel cell (URFC) has been developed that utilizes non-precious metal catalysts with alkaline anion exchange membranes (AEMs) in order to significantly reduce the cost of URFC systems. The best precious-metal based PEM URFC has a round trip efficiency of 60%. The round-trip efficiency of the non-precious metal based AEM-URFC reaches 40%, with current densities around 15 mA cm^{-2}. The AEM-URFC is attractive due to its low cost, clean, scalable, and ability to achieve high energy densities. However, the AEM-URFC must undergo further research and development to reach round-trip efficiencies greater than 80% and current densities around 1 A cm^{-2}.[56]

1.3.4. Superconducting Magnetic Energy Storage

Superconducting magnetic energy storage (SMES) utilizes direct current flowing through a superconducting coil without ohmic losses, creating a magnetic field in which the energy is stored. The coil must be cooled to a temperature below its superconducting critical temperature. An example alloy used for storage and transmission is niobium-titanium (NbTi) alloys cooled to liquid helium temperatures[57]. For an NbTi alloy, the refrigeration system required to cool the coil typically consumes approximately 1.5kW per MWh of storage capacity, continuously. Excluding the refrigeration system, the storage efficiency reaches above 90%.[58] Further advantages include the high dynamic response leading to response times within milliseconds, infinite charge and discharge cycles, reliability, low maintenance and relatively large power density than other ESS.[41,59]

With a fast response speed suitable for power grid applications, SMES are best applicable for improving power quality rather behaving as a long-duration energy storage system. The energy/power density of SMES systems has been improved using high-temperature superconductors (HTS). High temperature superconductors include compounds such as $Tl_2Ba_2Ca_2Cu_3O_x$ (TBCCO) which has a critical temperature around 120K[60]. The advantages of a HTS SMES system are response speeds on the order of milliseconds, a large power density, efficiency above 95%, and no mechanically moving parts. Disadvantages of the HTS SMES system include high material cost, high cooling cost, self-discharge in several days, low energy density, and superconductor instability in the loss of cooling power. Future work includes scaling up the current HTS SMES system, however system cost must be reduced dramatically for large-scale applications.[59]

1.3.5. Flywheel Energy Storage

Flywheel energy storage systems (FESSs) store energy in a rotary mass, consisting of a unit that serves as a motor and generator. The maximum rotational speed of the flywheel is the key design factor. Total energy stored in the flywheel is proportional to the square of the rotational speed. Consequently, a flywheel capable of higher speeds provides a higher energy density. The maximum stored energy depends on the flywheel material tensile strength, and the maximum specific energy depends on the ratio of the energy density and material density of the rotating disk material.[51] The two main types of FESS are low-speed (corresponding to high power) and high-speed (corresponding to high energy) flywheel systems.

Advantages of FESSs include ability to provide very high peak power, high power and energy density, long lifetime, lack of environmental detriments, and apparent unlimited life cycles. The useful lifetime of FESS systems are also comparatively long, up to 20 years. However, the more high-speed a FESS is, the more complex, which results in a prohibitively high cost.[41] A major component of the cost is the material in which the flywheel is composed of. Thus, high performance materials at lower cost must be researched and implemented for FESS to become more wide spread. Additional disadvantages of FESS include its relatively low energy density as well as a high self-discharge rate compared to other types of energy storage.[51]

FESSs are mainly being developed for vehicle application and impulse power generation for large-scale storage applications. FESSs are highly efficient when absorbing and releasing energy in short durations. FESSs have been used for various purposes including short-term storage and improving system frequency stability. Currently, the most successful application for FESS is in uninterruptible power systems (UPS). FESS is favored over electrochemical batteries in UPS. For frequency regulation applications, FESS must compete with Li-ion batteries.[61] As previously stated, FESS remain too expensive to be widely implemented for large-scale power system applications.[51]

A wind/hydrogen plant in Utsira-Norway utilizes a 100 kVA grid forming synchronous machine and a 200 kW output power low-speed FESS. The FESS is utilized for short-term energy storage, with a capacity of 5kWh. A power system on the island of Flores-Azores has a FESS capable of 350 kW output power and 5 kWh energy capacity, primarily used to improve system frequency stability. Another example plant implementing FESSs is a wind diesel hybrid system in Australia with a FESS used to smooth fluctuations in available wind power.[61]

1.3.6. Pumped Hydroelectric Energy Storage

Pumped hydroelectric energy storage (PHES) is a mature technology used globally. During periods of low electrical demand, water is pumped from a lower reservoir to an upper reservoir. When demand is high, water flows out of the upper reservoir and activates a turbine(s) to generate electricity during peak hours. Depending on equipment, efficiency is 65-80%. Storage capacity depends on the height of waterfall and volume of water. The main advantage of PHES is that it is readily available where geographically suitable, considering its use of hydroelectric power. PHES also has quick response times allowing control of electrical network frequency.[51] Of all the developed energy storage technologies, PHES is the most mature and reliable storage, and currently most used for high-power applications. Its main disadvantage is geographic limitations due to the need for a site with different water elevation or alternatively a very large body of water. Although PHES is relatively inexpensive and efficient, this geographic constraint leads to the search for energy storage systems that can be implemented globally. Furthermore, the high construction costs and environmental issues are deterrents for further adaption of PHES system.[37,51]

1.3.7. Compressed Air Energy Storage

During off peak hours, electricity is used to compress air, and during peak hours, compressed air is used to operate a combustion turbine along with the burning of natural gas to produce electricity. Aquifer storage is the most cost effective reservoir type for compressed air energy storage (CAES). Advantages of CAES systems include durability and flexible system size, with reduced sizes achievable through increased pressure. For example, the energy density of a CAES system is on the order of 12 $\mathrm{kWh \cdot m^{-3}}$ under 140 bars of pressure (P) and around 5.6 $\mathrm{kWh \cdot m^{-3}}$ under 30 bars, a more common pressure adopted for CAES systems, calculated simply by $h(\mathrm{P}) \cdot \rho(\mathrm{P})/3600$ where h is the specific enthalpy and ρ is the density at 25°C. Disadvantages include high initial capital costs, slow response, and geographic limitations.[47] A constant system temperature is necessary in CAES systems, which is affected by the exothermic and endothermic processes during air compression and expansion, respectively. The most commercially implemented system of managing the system temperature equilibrium uses external power to heat or cool the air.[41] CAES has the lowest cost per kWh of developed energy storage technologies, aside from certain thermal energy storage systems. However, this cost does not consider the cost required to cool and reheat the air, via burning fuel, when storing and releasing the air. CAES and PHS are currently deemed as the only suitable storage options for large-scale power and high energy storage, although CAES is capable of having a lower capital cost (depending on underground conditions and volume required) and minimal impact to the exposed environment if underground CAES is used, rather aboveground.[37,51,62]

1.3.8. Thermal Energy Storage

Thermal energy storage (TES) systems receive energy during charging, store the energy, then release the energy at a later time for use. For large-scale energy storage, the thermal energy is stored as thermochemical, latent heat, and/or sensible heat through a change in the internal energy of the storage medium. They are known for their ability to shift electrical loads between high-peak and off-peak hours, facilitate large-scale switching, ensure energy security, efficiency and environmental quality.[51,63] Main challenges in TES consist of developing low cost, and high temperature systems.[64]

1.3.8.1. Sensible Heat TES

In sensible TES, energy is stored by increasing the temperature of the material without the material undergoing phase change. The amount of thermal energy stored depends on the temperature change, density, specific heat, and volume of the material. The thermal storage material is typically a solid or liquid. Sensible TES systems consist of the storage medium, tank, and inlet/outlet devices. Disadvantages of sensible TES are the large tank size required due to large volume of material required, and the temperature swing produced from the addition and extraction of energy. Increase in storage size results in an increase in cost as well as thermal losses. The main factors affecting performance of sensible TES is the thermal diffusivity, density, and specific heat of the material used. Sensible TES systems utilizing water as the liquid media are primarily used for solar water heating plants. Molten salts have been applied in power tower systems due to their low cost, high temperature range, and non-toxicity.[51] Table 3 introduces material properties of common sensible heat TES materials.

Table 3. Main Characteristics of Sensible Heat TES reprinted from Kousksou et al.[51]

Storage medium	Cold Temperature	Hot Temperature	Average density (kg/m^3)	Average heat conductivity (W/m K)	Average heat capacity (kJ/kg K)	Volume specific heat capacity (kWh$_t$/m^3)	Costs per kg (US\$/kg)	Costs per kWh$_t$ (US\$/kWh$_t$)
Solid storage medium								
Sand-rock-mineral-oil	200	300	1700	1	1.3	60	0.15	4.2
Reinforced concrete	200	400	2200	1.5	0.85	100	0.05	1
NaCl (solid)	200	500	2160	7	0.85	150	0.15	1.5
Cast iron	200	400	7200	37	0.56	160	1	32
Silica fire bricks	200	700	1820	1.5	1	150	1	7
Magnesia fire bricks	200	1200	3000	1	1.15	600	2	6
Liquid storage medium								
HITEC solar salt	120	133	1990	0.6	–	–	–	–
Mineral oil	200	300	770	0.12	2.6	55	0.3	4.2
Synthetic oil	250	350	900	0.11	2.3	57	3	42
Silicon oil	300	400	900	0.1	2.1	52	5	80
Nitrite salts	250	450	1825	0.57	1.5	152	1	12
Nitrate salts	265	565	1870	0.52	1.6	250	0.5	3.7
Carbonate salts	450	850	2100	2	1.8	430	2.4	11
Liquid sodium	270	530	850	71	1.3	80	2	21

1.3.8.2. Latent Heat TES

Latent heat TES utilizes the heat released and absorbed during the phase change of a material. Phase change materials (PCMs) are viewed to be advantageous over sensible heat storage materials due to their higher stored energy density, resulting in less volume and mass of the storage medium required. From a thermodynamic point of view, phase change materials are also attractive as they deliver heat at near-constant temperature. Solid-liquid phase change in PCMs is most suitable for large-scale energy storage, with the three most common types being organic-PCM, inorganic-PCM, and eutectic-PCM. However, there remains developmental issues with most PCMs due to low thermal conductivity, instability of material properties during cycling, material corrosion, and maintaining transition temperatures.[51,63,64] Material properties of studied metal alloy PCMs are presented in Table 4. Recently, elemental silicon has been considered as a thermal storage medium, given its high energy density around 1200 kWh·m^{-3} at the melting temperature of ~1414°C[65,66].

Table 4. Material Properties of Metal Alloy PCMs reprinted from Gasanaliev, et al.[67]

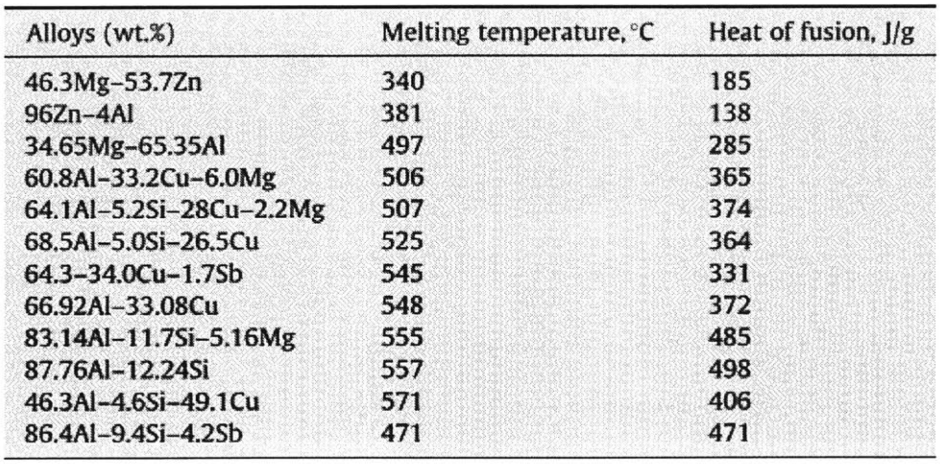

Alloys (wt.%)	Melting temperature, °C	Heat of fusion, J/g
46.3Mg-53.7Zn	340	185
96Zn-4Al	381	138
34.65Mg-65.35Al	497	285
60.8Al-33.2Cu-6.0Mg	506	365
64.1Al-5.2Si-28Cu-2.2Mg	507	374
68.5Al-5.0Si-26.5Cu	525	364
64.3-34.0Cu-1.7Sb	545	331
66.92Al-33.08Cu	548	372
83.14Al-11.7Si-5.16Mg	555	485
87.76Al-12.24Si	557	498
46.3Al-4.6Si-49.1Cu	571	406
86.4Al-9.4Si-4.2Sb	471	471

1.3.8.3. Thermochemical TES

Thermochemical energy storage utilizes the energy released through the breaking of chemical bonds, then recovered through a reversible chemical reaction. The charging of the system is endothermic, storing of the energy does not result in any thermal losses, and discharging of the system is exothermic. Advantages of thermochemical energy storage include higher energy densities than sensible and latent heat storage, on the order of 10^3 – 10^4 kWh·m^{-3} as well as minimal heat loss. Thermochemical energy storage is deemed more optimal for long-term energy storage than sensible or latent heat storage methods due to the minimal heat loss during storage, applicability to both short and long duration storage such as seasonal thermal storage, and higher energy density.[51] That being said, there still remains much work to be done in the material compatibility and system design as thermochemical storage systems require various components such as compressors, heat exchangers, storage tanks, and reactors. This gives rise to high system costs compared to sensible and latent TES systems. Promising thermochemical materials are evaluated based on cost, corrosiveness, cycling abilities, reaction rate and temperature range, energy storage density, non-toxic and non-flammable, and proper heat transfer and flow characteristics. Aside from material selection, reactor design is also a key consideration.[63]

1.4. Summary

To avoid and reduce negative impacts currently imposed upon existing power plants, the economy, as well as the environment, an energy storage solution is needed that can address the above enumerated issues. Namely, energy storage can replace peaker plants as a cleaner alternative to natural gas-fired peaker plants, energy storage can balance variations in demand such that baseload power plants are not forced into operating at partial- nor peak-load, and storage provides a segue from reliance on fossil fuels to renewable energies through hourly and seasonal storage. That being said, energy storage for power plants is not a novel concept to say the least, pumped hydroelectric energy storage has been developed since the 1890's[68,69], various battery chemistries have been proposed to support the grid[39,53,70–72], among other technologies reviewed. To emphasize key points from the technology overview, we summarize key points of the major technologies.

Pumped hydroelectric energy storage (PHES) converts off-peak electricity into stored gravitation potential energy via mechanical pumps, having a typical efficiency of 70-85%[47,51,62]. The energy is then converted back to electric through turbines during times of peak demand. PHES has been the main method of energy storage for fossil fuel fired power plants of high power generation, though the applicability of this method is highly dependent upon geographic location[37]. Compressed air energy storage (CAES) utilizes electricity to pressurize air and thus store the molecular energy to be later converted back to electricity through expansion, having a typical efficiency of 70-89% for underground CAES and only 50% for aboveground CAES[39,41,62]. Just as PHES, CAES is also limited by geographic location, albeit to a less severe extent for aboveground CAES. Among the energy storage technologies under research, batteries are being pursued the most [39,49,71–74], however the cost of such technologies are still too high to be practical for large-scale applications. Batteries can use off-peak electricity to charge and store energy in the form of chemical energy, then use chemical reactions to create a flow of electricity, having efficiencies that range from 60% to as high as 99%[38,48]. Even more expensive than batteries are technologies such as super magnetic energy storage, supercapacitors, flywheels, etc. [39,47,51,62]. All of the above methods of energy storage convert electricity already produced by other means, into another form of energy prior to storage. A summary of efficiencies, energy densities, and cost of the above reviewed technologies is provided in Figure 1-5 through Figure 1-7.

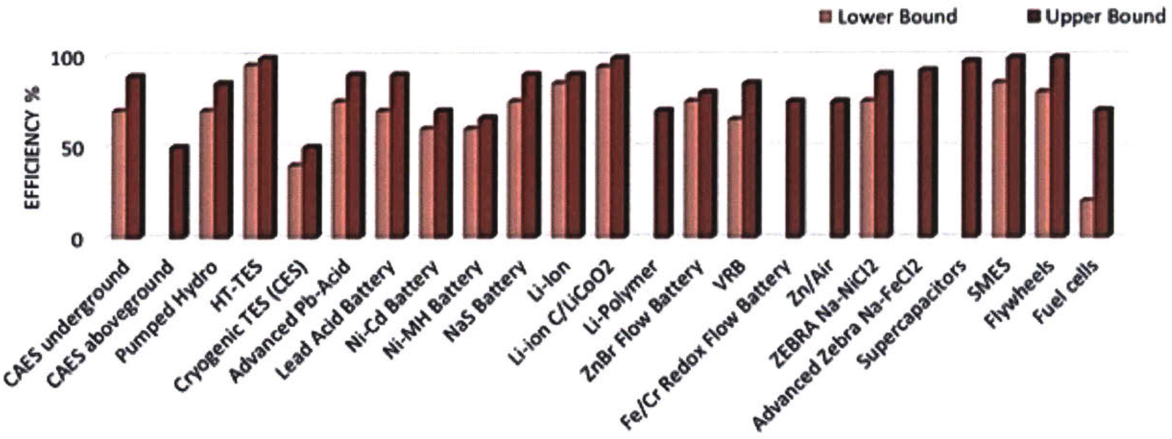

Figure 1-5. Energy storage technologies with respect to round-trip efficiency of the device. Sources: CAES underground and aboveground[41,62], Pumped Hydroelectric (Pumped hydro)[47,51,62], High temperature thermal energy storage (HT-TES) [47,51,62], Cryogenic TES[62], ZEBRA[38,47–49], ZnBr Flow[39,47], Vanadium Redox Battery (VRB)[38,47], Lead Acid[38,47,51,62], NaS[38,47], Fe/Cr Redox[39], Zn-air[39,75], Li ion[41,47,62], Lead-carbon ultrabattery[38], Advanced Pb-Acid[39], Ni-Cd[38,41,51,62], Li-ion Carbon anode, $LiCoO_2$ cathode ($C/LiCoO_2$)[38], Ni-MH[41,47], Li-polymer[41], Supercapacitors[47,62], SMES[47,62], Flywheels[47,62], Fuel cells[47,62]

Efficiency is not the only key characteristic in determining a feasible storage method for power plants; energy density and cost are also critical factors. Of the aforementioned storage options, thermal energy storage has the best chance of competing with PHES in terms of cost per kilowatt-hour due to high energy densities and low material cost, as can be seen from Figure 1-7.

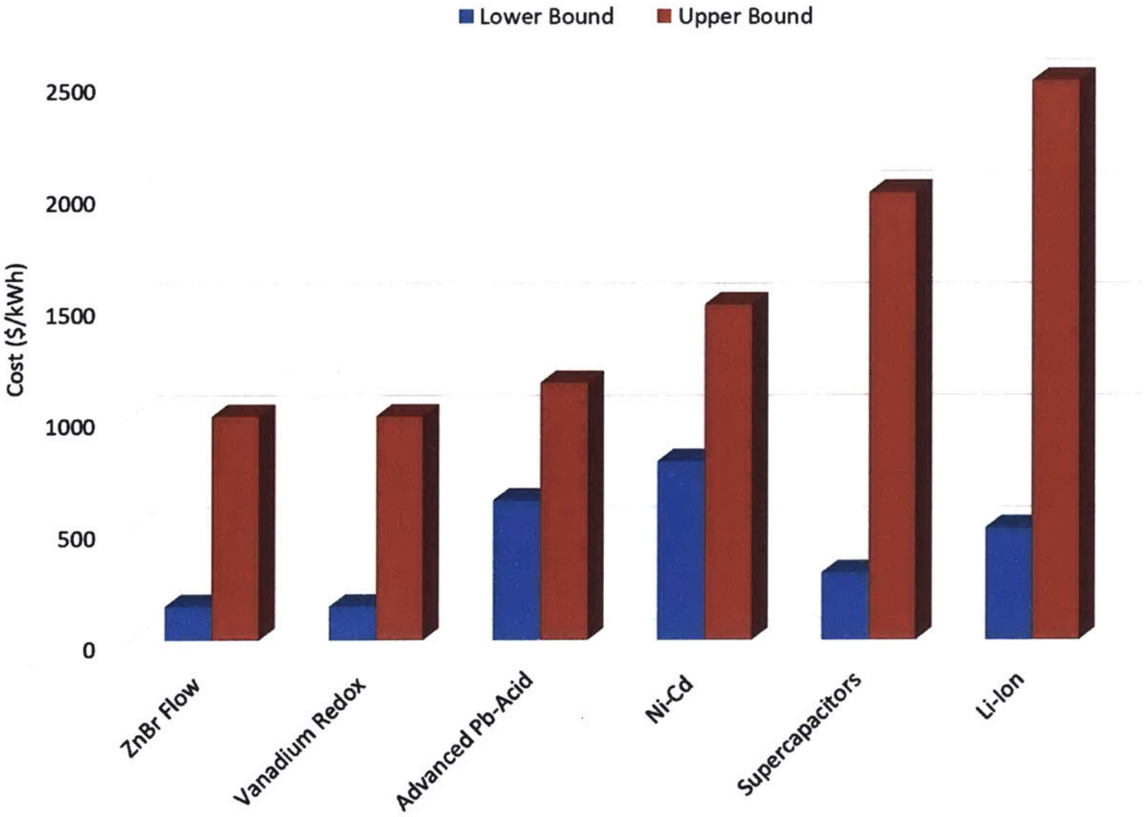

Figure 1-6. Energy storage technologies with respect to cost of device, for upper bounds exceeding 500 $/kWh. Sources: ZnBr Flow[39,47], Vanadium Redox Battery (VRB)[38,47], Li ion[41,47,62], Advanced Pb-Acid[39], Ni-Cd[38,41,51,62], Supercapacitors[47,62]

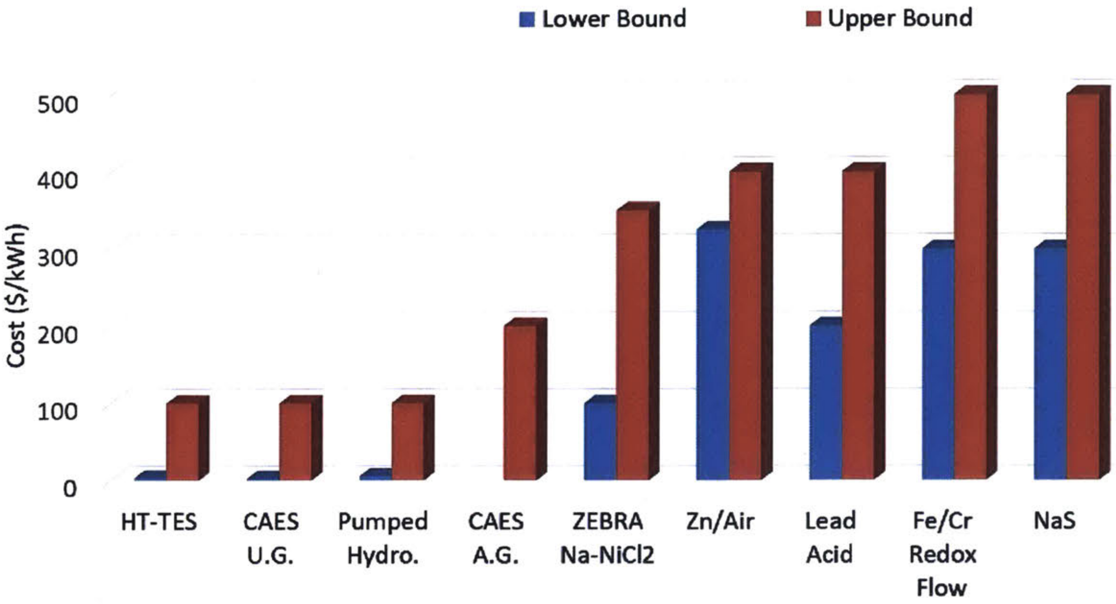

Figure 1-7. Energy storage technologies with respect to cost of device, for upper bounds below 500 $/kWh. Sources: CAES underground and aboveground[41,62], Pumped Hydroelectric (Pumped hydro)[47,51,62], High temperature thermal energy storage (HT-TES) [47,51,62], Lead Acid[38,47,51,62], NaS[38,47], Fe/Cr Redox[39], Zn-air[39,75], ZEBRA[38,47–49]

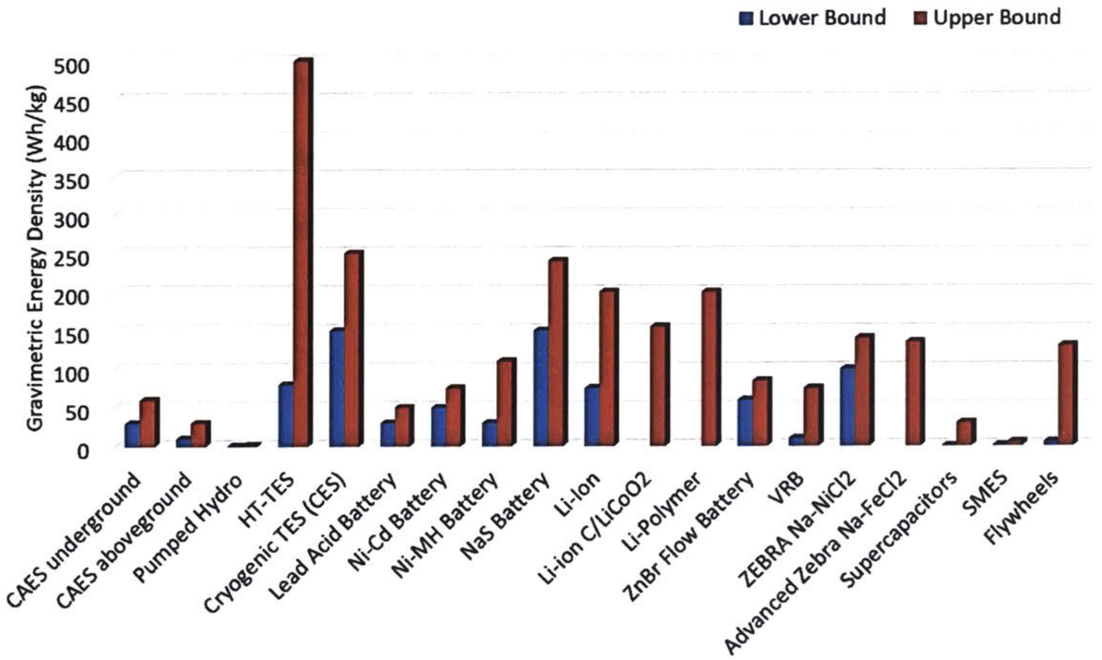

Figure 1-8. Energy storage technologies with respect to gravimetric energy density. Sources: CAES underground and aboveground[41,62], Pumped Hydroelectric (Pumped hydro)[47,51,62], High temperature thermal energy storage (HT-TES) [47,51,62], Cryogenic TES[62], ZEBRA[38,47–49], ZnBr Flow[39,47], Vanadium Redox Battery (VRB)[38,47], Lead Acid[38,47,51,62], NaS[38,47], Fe/Cr Redox[39], Zn-air[39,75], Li ion[41,47,62], Lead-carbon ultrabattery[38], Advanced Pb-Acid[39], Ni-Cd[38,41,51,62], Li-ion Carbon anode, $LiCoO_2$ cathode ($C/LiCoO_2$)[38], Ni-MH[41,47], Li-polymer[41], Supercapacitors[47,62], SMES[47,62], Flywheels[47,62], Fuel cells[47,62]

For regions in which PHES or CAES is not an option due to geographical constraint thermal energy storage (TES) presents itself as a complete solution and is, in fact, the main method of energy storage for solar thermal power plants in the form of sensible heat[76–80]. That being said, TES requires further development towards fulfilling storage needs across the spectrum of power plants (e.g. renewable energy, pulverized coal, nuclear, etc.). Existing large-scale TES systems in practice directly store thermal energy rather utilizing electricity already produced by existing power plants. Unlike these existing TES systems, an energy storage system must be developed that can couple with both renewable, nuclear energy and existing fossil-fuel dependent plants, otherwise global adoption does not seem to be feasible for present efforts to mitigate climate change. Electrically charging a TES system gives rise to system flexibility with respect to coupling to different types of energy sources.

In theory, electrical heating can produce temperatures as high as desired, given material compatibility, thereby allowing high Carnot efficiencies. Furthermore, utilizing electricity via resistive heating to 'charge' a thermal energy storage unit has negligible losses, i.e. ~100% efficient, since all current supplied to the resistive heating element will be converted into heat dissipated into the surrounding TES medium. The round trip efficiency using TES is hence essentially determined by the thermal-to-electrical power plant machinery such as condensers and turbines, and any losses from the storage unit to the environment, which are later proved negligible. Considering that the mentioned thermal power plant efficiencies (ref section 1.1) have included exhaust losses, while a TES does not have exhaust loss, it is reasonable to expect that TES systems based on supercritical Rankine cycle can achieve round-trip efficiencies above ~42%. Such TES systems are absent of geographical restraints and can take advantage of the existing power conversion block in a typical power plant for reduced capital cost. They can provide a universal storage solution to numerous issues presently threatening the stability of the electric grid as well as the environment. Whether electrical heating of sensible or latent heat-based materials proves most cost effective presents a more involved question to be pursued.

As TES is well known to convert thermal to electrical energy, small scale systems have been implemented which convert electricity to thermal energy (i.e. electrical load management in buildings, TES for cooling capacity, home water heaters)[81–84]. Only recently has there been work published on conversion of electricity to thermal energy then back to electricity, including: the conversion of electricity from wind turbines into sensible heat stored in rocks then back to electricity via steam turbines by Siemens [85]; possible conversion of electricity into latent and sensible heat stored in silicon then back to electricity via thermophotovoltaic cells by Datas et al.[65]; and possible conversion of electricity into latent and sensible heat stored in silicon then back to electricity via Brayton cycle by the Australian company 1414 Degrees[86]

We aim to evaluate a cycle connecting these two cycles—systematic conversion of electrical to thermal back to electrical energy, using thermal energy storage in the form of latent or sensible heat. From a thermodynamic perspective, converting electrical energy into thermal energy, then back to electrical is not favorable. Nonetheless, such a method is deserving of consideration on large scales, since the widely adopted systems of PHS and CAES also demand such energy conversions as depicted in, yet do not present themselves as global solutions to the energy crisis.

1.5. Outline of Thesis

In this thesis, an evaluation is performed on the potential integration schemes of an electrically heated thermal energy release and storage system (TERS) into existing fossil fuel-fired plants as well as renewable energy-based plants. For high-temperature, high-pressure power blocks, such as those utilizing supercritical water or supercritical CO_2, we introduce a version of TERS based off radiative heat transfer between the TES medium and the water pipes. We also introduce versions of TERS that utilize conduction to release stored heat, through direct contact between TES units and water pipes, which is capable of producing supercritical fluids but more ideal for lower pressure systems due to safety aspects to be discussed.

It is important to note that for any system being developed with the goal of implementation in mind, attention during conception must be paid not only to the technical aspects, but also to the economic, social, and environmental aspects of the system. Candidate energy storage materials are evaluated based on metrics such as ease of integration, environmental impact, operating temperatures, and cost. The objective of this work is not to perform a detailed whole-system analysis, but rather to provide a sound argument that such TES systems have the potential to provide a cost-effective solution for grid-level energy storage in the near-term, for both renewable-based and fossil-fuel dependent plants, rather one or the other. A sustainable framework of energy production for immediate action against climate change must allow for, and be built upon, nuclear, fossil, and renewable energy sources working synergistically, as also acknowledged by Forsberg[87].

Chapter 2 describes the overall schematic of an electrically charged thermal energy storage system with supercritical power plants, and lists the power and storage demand of the model power plant considered. The benefits of the system are discussed with respect to both fossil fuel-fired power plants, and renewable energy-based power plants. In chapter 3, the radiation based thermal energy storage system is introduced and the heat transfer model is derived. Likewise, in chapter 4, the conduction based thermal energy storage system is described. Chapter 5 concerns the cost of the electrically charged thermal energy storage systems and how it compares to existing storage methods.

Chapter 2 Supercritical Water Power Plant Integration

2.1. Integration with Fossil Fuel-Fired Power Plants

As previously stated, the thermal energy storage system developed herein can couple to different power blocks and heat fluids to different temperatures depending on restrictions set by the existing infrastructure (e.g. according to turbine specification, maximum temperature and pressure of pipes, etc.). However, since coal is expected to remain a key source for electricity generation, and even grow in demand in developing countries, it is most appropriate to evaluate TERS coupled to a coal-fired power plant[88]. More specifically, we model TERS coupled to a supercritical water power plant (Figure 2-1), as that is the cycle that most recent and future coal-fired power plants adopt.

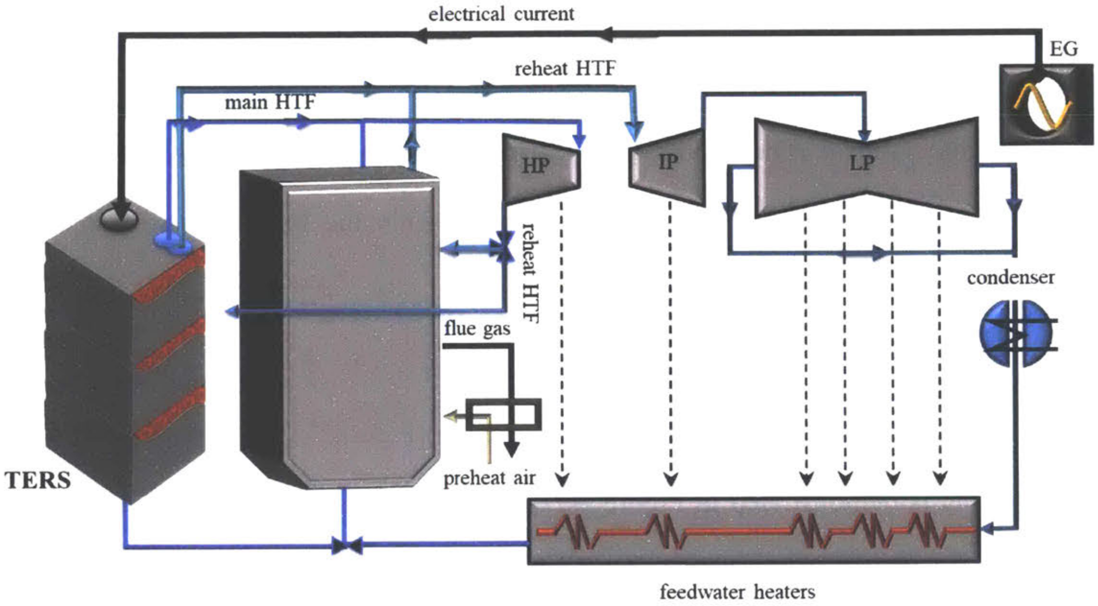

Figure 2-1. Illustration of TERS coupled to coal-fired power plant for peak shaving, load leveling, and reduction of fuel consumption. The same concept may be applied to other power plants such as nuclear.

In the configuration depicted in Figure 2-1, the boiler operates at baseload according to rated capacity, while TERS compensates for variations in demand. TERS can be charged by electricity generated by the plant, or electricity from the grid. Here, dashed flow lines indicate exhaust fluid. The amount of power produced by TERS can be controlled by the mass flow rate of the fluid sent to the subsystem. For a supercritical (SC) water rankine cycle, water shall flow through TERS, reaching temperatures above 575°C at a pressure of 250 bar, thus transitioning to supercritical water prior to the outlet. A separate line of water can flow through the boiler (B), reaching supercritical temperatures within the boiler and rejoining the supercritical water from TERS at the high-pressure (HP) turbine. If the boiler is in operation, air will be preheated by heat exchange with exiting flue gas. Note, there is no flue gas generated by TERS. After the HP turbine, exhaust steam goes through a reheat cycle within the boiler/TERS at constant pressure (no longer in the supercritical regime) to reduce moisture content of the steam and produce further work within the intermediate-pressure (MP) turbine. Exhaust from the MP turbine is sent through the low-pressure (LP) turbine without reheat. The turbines will be used to convert mechanical energy into electrical via the electrical generator (EG). Extraction points within the turbines direct steam to the feedwater heaters for increased plant efficiency.

The hourly operation of TERS in the above configuration (Figure 2-1) to manage load following and peak shaving is demonstrated in Figure 2-2. By operating a thermal energy storage unit as illustrated, boilers can operate at a nearly constant load, reducing thermal stress on the boiler. Such operation solves a number of issues that fossil fuel-fired plants battle. First, it eliminates the need for cyclic operation. The nature of the deregulated market gives rise to operators having to choose between less than ideal unit operations, up to the point of steady electricity production wherein the operator is able to compete in the market again. Supercritical boilers in particular require a considerable amount of fuel for successful startup, and therefore startup is costly for both the plant economy and the environment. Second, cyclic operation (includes load following, on/off operation) of boilers reduces the boiler lifetime, increases operation and maintenance costs, and increases emissions by the reduction in thermal efficiency. Savings achieved with the proposed energy system in supercritical power plants can reach around 100$ per megawatt capacity, per cold start, and around 2$ per megawatt capacity, per load following event assuming a typical normal ramp rate for a coal-fired supercritical power plant. Here, load following event is defined as a change in generation within 32% of gross dependable capacity, beyond which the event is defined according to a warm or cold start[89]. A detailed energy storage dispatch model for assessing the economic benefits introduced with an energy storage system for cycling and load following, specifically with respect to CAES and wind penetration, is provided by Das et al[3]. Though evaluated for CAES with condition of wind penetration, their conclusions support the claims made herein. Mainly, that bulk energy storage greatly benefits the grid through relief of unit cycling thereby increasing system efficiency, and storage reduces the total system CO_2 emissions therefore increasing revenue through elimination of carbon tax and through increased system efficiency.

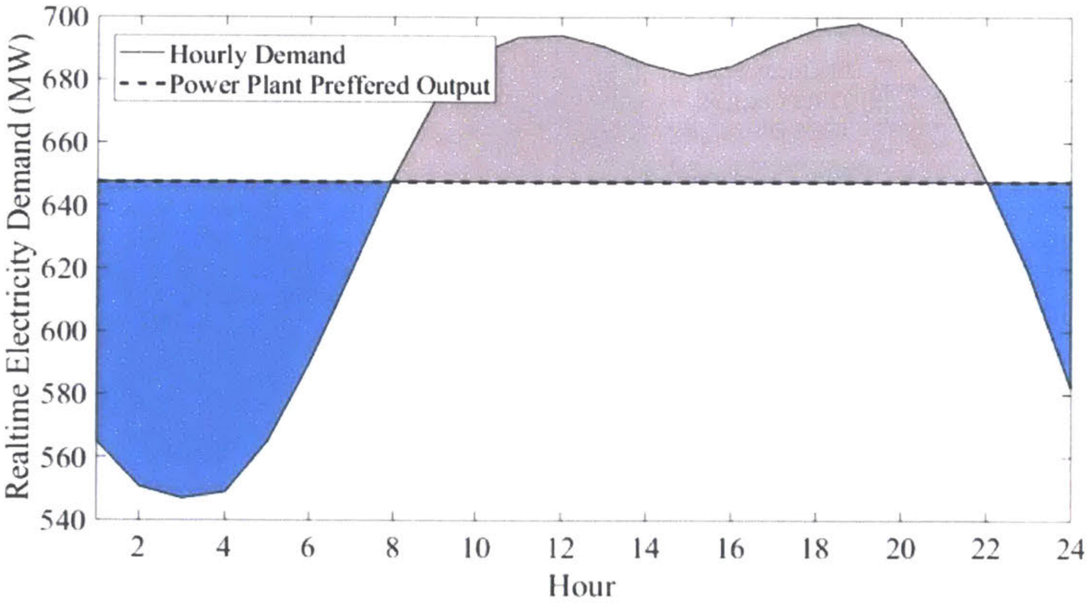

Figure 2-2. Hourly Demand Balance for state of New York. (a) Example operation of TERS over a period of 24 hours, using demand data of February 10th, 2017[2] . During times in which demand falls below base-load operation (shaded blue regions), electricity generated is used to charge TERS. During times in which the electricity demand exceeds base-load operation, TERS is discharged to compensate.

A critical aspect of the system envisaged within is the ability to charge TERS with electricity, an ability that originally made batteries so attractive. With the freedom to charge this system with electricity, operation of TERS is not restricted to optimizing boiler effeciency. Rather, revenue can be maximized by energy arbitrage. Energy arbitrage in this scenario refers to charging TERS during times of low Locational Marginal Price (LMP), and discharging TERS during times at which the LMP is high. In TERS, the discharge is achieved by passing heat transfer fluids through the TERS. An example case based on realtime LMP pricing for the state of New York (NY) over the course of 24 hours is presented in Figure 2-3[90].

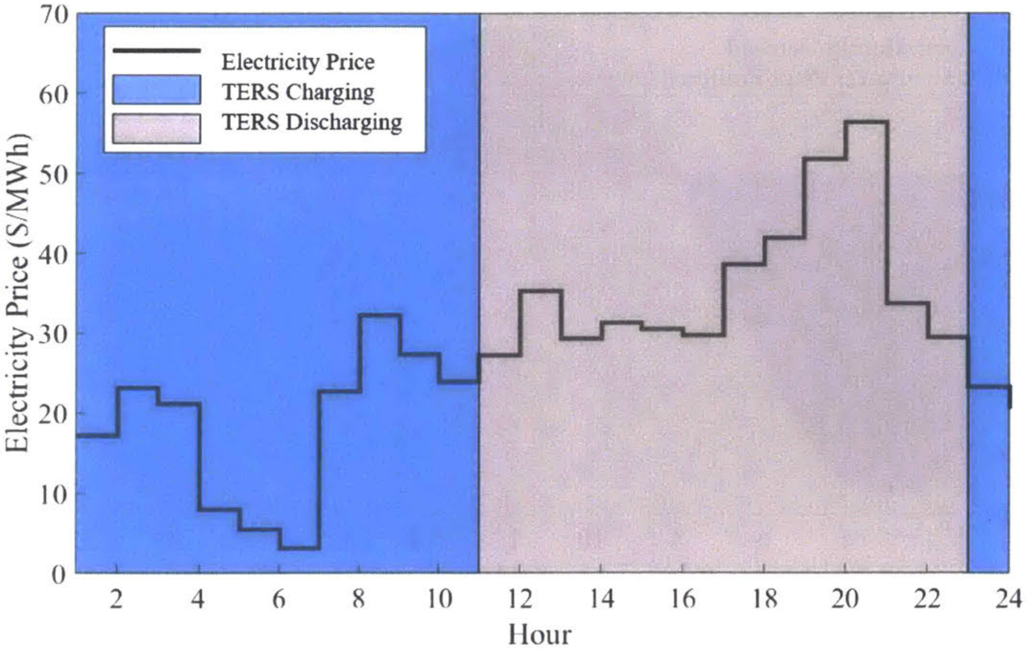

Figure 2-3. Revenue-maximizing operation of TERS in current energy market. Real-time price variation for state of New York over the period of a day (Feb. 10th, 2017) with example distribution of charging and discharging TERS, based on price arbitrage in NY electricity market.

Regardless of whether TERS is charged by purchasing electricity at low LMP from the grid, or charged by electricity generated from the accompanying boiler, an overall profit can be made by optimizing according to hourly variation in the LMP. Although thermal energy storage systems are excluded from their evaluation, Bradbury et al. study the economic potential for energy storage systems in terms of the internal rate of return (IRR), operating based on price arbitrage, and can be reffered to for a detailed economic analysis. Of the systems examined, Bradbury et al. conclude that PHS and CAES have the greatest potential for arbitrage, having the highest IRR due to a combination of low self-discharge rate, high round-trip efficiency, and ability to store 5 or more hours of energy[91]. Based on such conclusions, TERS should also have great potential for price arbitrage, considering it meets the above listed criteria to the same degree, if not better, as CAES and PHS. Indeed, we find that TERS in operation based on price arbitrage such as depicted in Figure 2-3 can create a revenue of 16 $/MWh of electricity during discharge, assuming electricity is purchased from the grid to charge TERS. This estimate is simply calculated by taking the difference in sum revenue during discharge and sum expense during charging, divided by the period of discharge (12 hours). . For power plants charging TERS with electricity produced in-house, this revenue estimate will undoubtedly be greater since on average the cost to produce electricity is less than the price at which it is sold.

2.2. Integration with Renewable-based Power Plants

For regions of the world with large penetration of renewable energies, TERS can be designed such that it supports the grid during times at which renewable energy is not instantly available. Solar energy is a globally available resource, photovoltaics are widely deployed compared to solar thermal, and pathways towards terawatt scale deployment of PV have been identified[92]. Due to the incontrollable intermittency of solar energy, an energy storage system must work synergistically with PV for global adoption. We present an example scenario of TERS coupled with PV to allow further deployment globally, depicted in Figure 2-4. Rather direct distribution into the grid, electricity generated by PV can be stored in TERS, then later converted back to electricity by existing or new power plants. As an inexhaustible source of clean energy, harnessing solar energy through PV is becoming more widely adopted on large scales (i.e. MW PV farms) in various countries, including Spain, Germany, U.S., etc[93]. Specifically, China and Mongolia have constructed PV farms in the desert, and utilize transmission lines to direct the electricity from the desert to populated regions. A system such as TERS can alleviate both frequency regulation issues associated with PV and also allow for more effective use of solar energy[94,95].

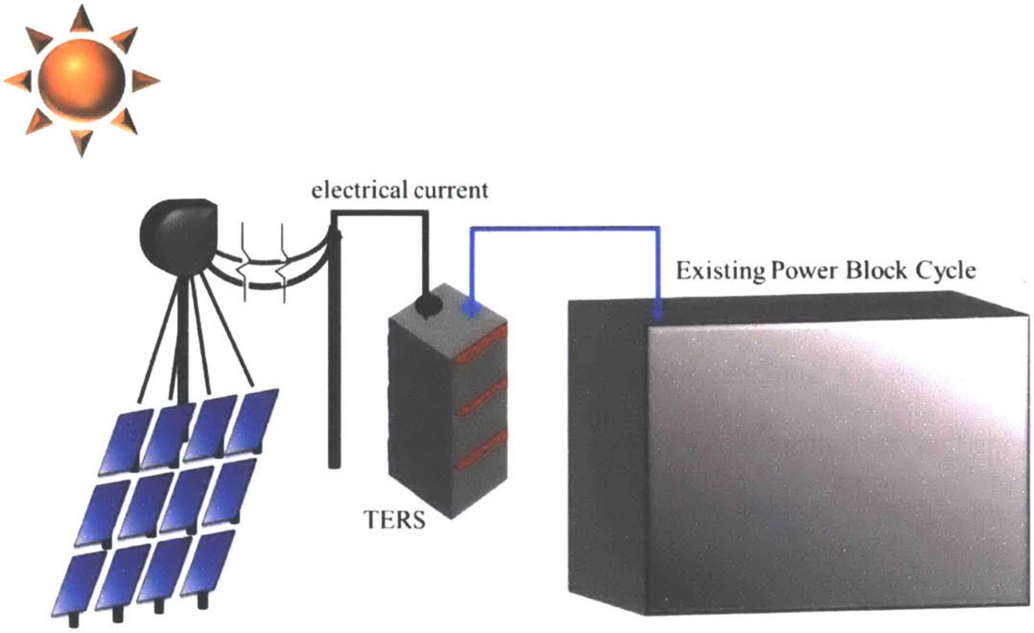

Figure 2-4. TERS charged by renewable energies. Illustration of TERS coupled with PV to resolve the intermittency issue inherent to solar energy and allow deployment of PV for large-scale electricity generation. Section view of TERS provided to illustrate electrical heating elements and water pipes.

To allow deployment of PV for large-scale electricity generation, TERS can be charged by excess electricity from PV, and discharged to produce electricity by utilizing the infrastructure of an existing or new power plant. However, a boiler or combustion chamber is not requisite to produce electricity upon discharge when TERS is coupled to PV.

In 2016, the state of New York generated a total of 62,000 MWh for the month of November, solely from solar photovoltaic technologies. This was a 47% increase from the previous year, and considering the decreasing price of silicon photovoltaic cells, an increase in PV production can be expected[96]. Unfortunately, the price of PV cells is only half the struggle in successful and efficient adoption of PV-based power plants. The other half consists of efficient and economic storage of the electricity, with flexibility to meet dispatch demands. Aside from reduction of emissions and frequency regulation, storage for PV electricity generation can also be used for arbitrage or for increasing revenue by the sale of renewable, as discussed for wind and solar energy by Braff et al.[97]

By storing electricity from renewable energy sources during times of low demand and then discharging this electricity via TERS, PHS, CAES, or batteries during times of high demand, one can undoubtedly mitigate CO_2 emissions.

2.3. Thermal Energy Storage Parameters

To estimate cost of TERS for an example power plant, and thus feasibility, the desired storage capacity must first be set. We consider a typical plant output capacity of 650 MW_e for which charging and discharging may follow that of Figure 2-2. The energy stored in TERS will therefore be the area under the baseload curve bounded by the electricity demand. This results in a total of ~670 MW_ehr of energy stored, and ~ 500 MW_ehr of energy released during discharge. Considering the cycle efficiency, the amount of total thermal energy stored in TERS follows

$$E = 10^3\left[\int_{t=1}^{8}\left(BL - Demand(t)\right)dt + \int_{t=22}^{24}\left(BL - Demand(t)\right)dt\right]\cdot 3600\,/\,\eta \qquad (2\text{-}1)$$

In Eqn. (2-1), E is the amount of stored thermal energy in kilojoules (kj), BL is the constant baseload provided by the boiler (650 MW_e), *Demand(t)* is the hourly demand according to Figure

2-2, *t* is the storage time in hours, and η is the electric-to-thermal efficiency, a function of storage efficiency and power block efficiency.

The efficiency of the storage system is simply given by $\eta_{storage} = 1 - Q_{loss}/Q_{stored}$ where Q_{stored} accounts for the energy put into TERS through resistive heating and Q_{loss} accounts for unwanted convection between the insulation and surroundings, radiation from the insulation, and conduction through the insulation. In fact, Henry et al. has performed the above thermal loss analysis for a thermophotovoltaic block, concluding that heat leakage ultimately depends on the volume to surface area ratio of the system, and thus system sizes must be optimized to minimize loss and maximize efficiency[66]. After performing a similar analysis for TERS, the same conclusion is made, and therefore the efficiency of the storage system can be estimated as 100% for initial modeling. Taking into account that a boiler's flue gas exhaust is accountable for 3-8% of efficiency loss in coal-fired power plants, the efficiency of supercritical fluid generated with TERS will be 3-8% higher than the typical 41.5% - 45% system efficiency of supercritical coal-fired power plants since TERS does not generate exhaust gas[98,99]. Therefore, we can conservatively estimate the entire cycle efficiency η to be that of the cycle efficiency without storage, and without thermal losses by exhaust gas, i.e. ~45%-50% efficiency for supercritical Rankine cycle adopting the lower bound of typical supercritical plant efficiency as discussed in section 1.1.2.

The required volume, in cubic meters, of storage material is then

$$V = \frac{E}{\rho\left(h_L + c_p(T_C - T_D)\right)} \tag{2-2}$$

where ρ is the density of the thermal energy storage medium, h_L and c_p are the latent heat of fusion and heat capacity of the material, respectively, T_C is the charged temperature of the storage medium, and T_D is the discharged temperature of the medium. Since we wish to take advantage of the large latent heat of the phase change materials evaluated, it is not necessary to have a large temperature deviation from the phase change temperature. A temperature difference of 100°C is used in the calculations. The discharge (min. temperature) and charged (max. temperature) temperatures used for sensible storage materials is provided in Table 5. Material properties for all evaluated storage mediums are provided below in Table 5 and Table 6. Phase change materials (PCMs) are selected for evaluation based on the thermal conductivity, as a low thermal conductivity is typically the limiting factor in applying PCMs for thermal storage.

Table 5. Solid and Liquid Sensible Material Properties

Material	Min. Temp (°C)	Max. Temp (°C)	Density (kg m^{-3})	Average Thermal Conductivity (W $m^{-1}K^{-1}$)	Average Heat Capacity (kJ $kg^{-1}K^{-1}$)
Silica Fire Bricks[100]	200	700	1820	1.5	1
Magnesia Fire Bricks[100]	200	1200	3000	1	1.15
Carbonate Salts	450	850	2100	2	1.8

Table 6. Phase Change Material Properties

Material	T_{melt} (°C)	Density (kg m^{-3})	Average Thermal Conductivity (W $m^{-1}K^{-1}$)	Latent Heat of Fusion (kJ kg^{-1})	Average Heat Capacity (kJ $kg^{-1}K^{-1}$)
Silicon[101]	1414	at 1414°C 2520 (liq.)	at 1414°C ~56 (liq.) ~20 (solid)	1800	1.04
$Al_{0.88}Si_{0.12}$[102]	576	2700	160	560	1.741

The thermal conductivity of silicon varies considerably near the melting point, as can be seen in Figure 2-5 adapted from Yamasue 2002. There will therefore be uncertainty in the thermal conductivity used to calculate total heat flux through silicon in the following chapter.

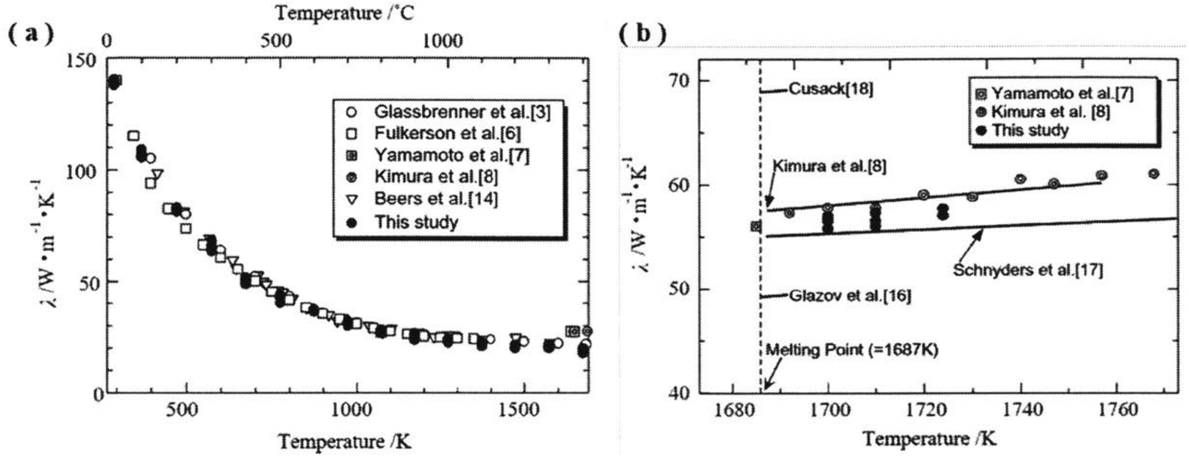

Figure 2-5. Thermal conductivity of silicon in solid state and liquid state. Figure reprinted from Yamasue 2002^{103}.

Chapter 3 Radiation Based Thermal Energy Storage

3.1. Introduction

From Table 6, we find that silicon not only has an exceedingly high latent heat of fusion, but also has a melting point that is an order of magnitude greater than the final heat transfer fluid (HTF) temperature (570°C). This allows us to harness radiative heat transfer from the thermal storage unit to the heat transfer pipes, an attractive mode of heat transfer from a safety aspect. Supercritical fluids are pressurized to over 200 bar, which presents safety challenges when the HTF pipes are immersed in a molten metal. In the case of a pipe cracking after prolonged thermal cycling and fatigue (an inevitable occurrence in boiler furnaces), the pressurized fluid in contact with unpressurized molten metal may create a highly hazardous event. Therefore, we first consider a storage design based on radiative heat transfer between the storage unit and HTF pipes, circumventing any need for intimate contact between pressurized fluid and molten silicon.

As previously stated, a key limiting factor in energy storage systems becoming widely adopted is cost. Although silicon is the second most abundant element in the earth's crust, lending itself as an abundant phase change material at low cost, there are numerous system components that may raise the cost beyond acceptable values. These include the electrical heating elements, container material enclosing silicon, HTF pipes, insulation, etc.

3.2. Electrical Heating Methods

There are multiple methods in which silicon can be electrically heated. In silicon smeltering plants, silicon is typically produced in a submerged electric arc furnace. This method involves immersed carbon electrodes in a crucible filled with quartz and charge, as shown in Figure 3-1. The charge may be a mixture of reductants such as coal, coke and chips which are necessary since solid silicon is not electrically conductive enough on its own. The arc is formed between the electrodes and crucible, through the material. Due to the higher density of pure silicon than silica, upon the main reaction of $SiO_2(s) + 2C(s) \rightarrow Si(\ell) + 2CO(g)$, molten silicon sinks to the bottom of the crucible allowing for separation from the resulting slag. Although electric arc furnaces are capable of reaching temperatures over 2000°C, continuous feeding of charge is impractical for melting silicon in storage applications and will require the silicon to be transported from the arc furnace to a separate container after melting so that the silicon may be separated from remaining solid charge in the crucible.

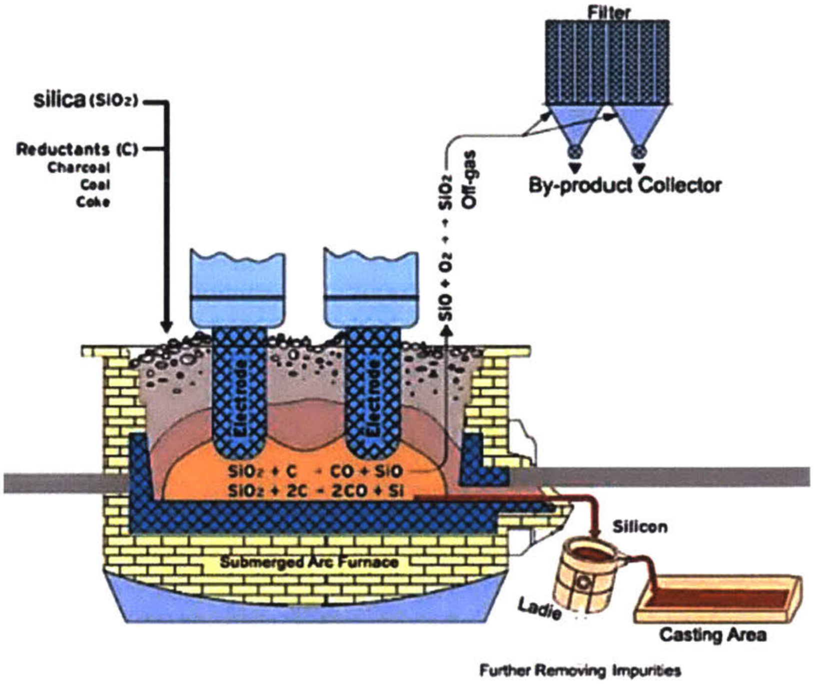

Figure 3-1. Typical submerged arc furnace for silicon smelting. Figure adapted from Southern Africa Analysis & Smelting[104].

A stationary design for the molten silicon is more attractive in thermal storage applications. Therefore, we consider inductive heating or immersed cartridge heaters. Induction heating of silicon is a well-established method in the field of solar cells and microelectronics[105–108]. An example inductive melting method consists of copper coils wound around silicon in a water-cooled metallic crucible. By keeping the crucible cool, a solid layer of silicon will remain between the crucible and molten silicon thus eliminating contamination from the crucible and protects the crucible from the melt. A schematic of an induction cold crucible furnace is provided in Figure 3-2. In the case of storing thermal energy in silicon, the only reason for concern towards silicon reacting with the container is that of reducing the container's structural integrity through diffusion of, for example, carbon from a graphite or silicon carbide container. Aside from being a noncontact method of electrically heating silicon, another advantage of induction heating is that of mixing within the molten silicon by the electromagnetic Lorentz force, resulting in a more uniform body of silicon. The efficiency of inductive heating depends upon the material properties of the crucible. For a graphite crucible, we may expect efficiencies around 90%. One must also consider the size of the sample to be heated and the properties of the sample. For example, since the electrical resistivity of silicon is on the same order as that of graphite, the size of each must be designed such that heating occurs mainly in the silicon rather graphite.

The heat generation rate by induction heating in a cylindrical body of solid silicon can be approximately expressed as

$$Q'_g = \pi^3 B^2 a^4 f^2 / \sigma \qquad (3\text{-}1)$$

where Q'_g is the heat generation rate per unit length of the silicon having units of Watt per meter [W/m], B is the effective magnetic flux density, a is the radius of silicon, f is frequency of the sinusoidal magnetic flux, and σ is the electrical conductivity. Since the electrical conductivity of silicon increases abruptly upon transition from solid to liquid, the heat generation rate is expressed differently in liquid silicon, as

$$Q'_g = 2B^2 a \sqrt{\frac{\pi^3 f}{\mu^3 \sigma}} \qquad (3\text{-}2)$$

where μ is the magnetic permeability[107]. The optimal frequency can be determined by Eqn.3-1 and Eqn.3-2.

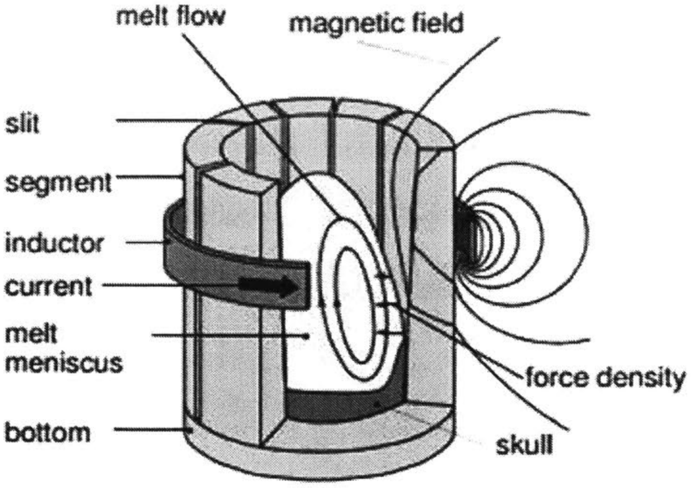

Figure 3-2. Illustration of an induction cold crucible furnace for silicon melting, adapted from Muhlbauer[109]. Skull refers to the solid layer of silicon between the melt and crucible.

In induction heating, eddy currents induced by the electromagnetic field result in joule heating of the silicon. Rather than implementing this direct method of joule heating, one can also implement indirect joule heating through immersed electrical heating elements. The generated heat will conduct into the surrounding silicon in which the thermal energy is stored as latent heat. Resistance heaters are quite common and used in a variety of applications, which includes heating thermal storage media such as refractory bricks to provide residential heating throughout the day. Most heating elements are composed of silicon carbide (SiC), capable of heating up to ~1500°C in an oxidizing atmosphere such as air. One can also use graphite heating elements, similar to the carbon electrodes used in submerged arc furnaces[110]. We use cartridge heaters as the example heating method to estimate system cost since they are more common, flexible in application, and pricing is easily accessible compared to the aforementioned heating methods. The expression for heat generation rate from an electrical heater is much more simple than that by induction, expressed as $P = I^2R_{EH} = Q_g$ where P is the power converted from electrical to thermal energy, I is the current (direct current), R_{EH} is the electrical resistance of the heating element and Q_g is the heat generation rate.

Another option for heating is directly passing current through the silicon. In this case, the main parameter in need of controlling is the overall electrical resistance of silicon, R_{Si}. This resistance is a function of the sample geometry and resistivity of silicon (ρ_{Si}) as $R_{Si} = \rho_{Si}l/A$ where l and A is the length and cross-sectional area, respectively, through which current must pass from the negative to positive electrode. In the case of all four methods, testing must be done to evaluate if it is viable to produce heat using silicon as the electrical resistor. The electrical resistance of silicon from solid to molten form is provided in Figure 3-3. To use direct current heating or electric arc heating without added charge, solid silicon must provide the resistance through which the arc forms. This is the same concept as having a silicon carbide resistance or graphite heater immersed in silicon if all the current isn't dissipated as heat in the heating element. Induction heating seems most attractive as reaction of electrodes with molten silicon will not be a concern. Again, experimental work must be done to prove if it is a viable method given the electrical resistance of silicon.

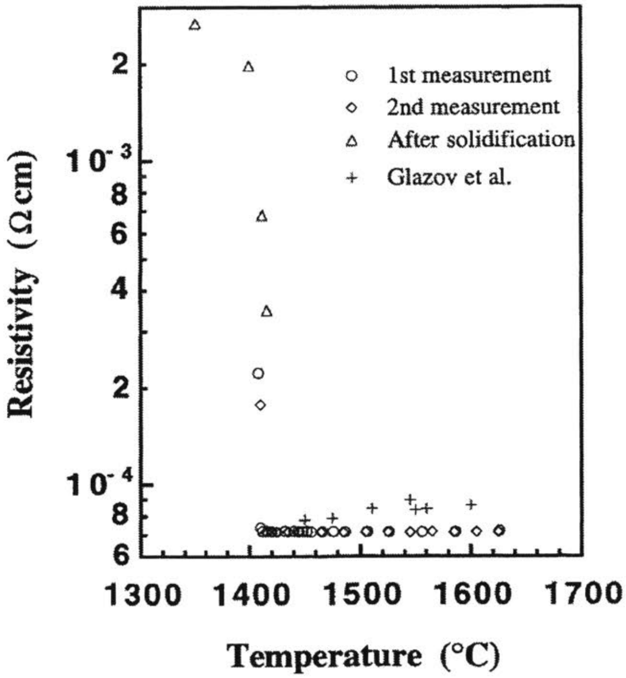

Figure 3-3. Electrical resistance of silicon through phase change from solid to liquid. Figure adapted from Sasaki et al.[106]

3.3. Molten Silicon Container and HTF Tubes

To effectively harness radiative heat transfer as the main mode of heat transfer between the contained silicon and HTF pipes, the container must have high emissivity and high thermal conductivity. The container material is further restricted by compatibility with molten silicon, as molten silicon reacts with most materials. Conveniently, graphite has both a high emissivity and high thermal conductivity, with ample studies previously conducted on the wettability and reaction of molten silicon with graphite since graphite-lined vessels are used in the silicon smelter and photovoltaic industry[111–115].

Molten silicon reacts with graphite to form SiC, though the extent of this reaction is highly dependent upon surface roughness, graphite grade and material structure, atmospheric composition, and oxygen partial pressure, amongst other factors. Although the formation of a SiC layer at the interface of graphite and molten silicon is unavoidable, further infiltration of silicon into graphite can be avoided by using high-density isostatically pressed graphite grades[111]. In fact, molten silicon (Si) itself does not wet a carbon surface, where wetting is characterized by the contact angle θ as shown in Figure 3-4(d) and defined by the Young-Dupré equation as

$$\theta = \cos^{-1}\left[\frac{\gamma_{sg}-\gamma_{sl}}{\gamma_{lg}}\right] \tag{3-3}$$

for a liquid droplet on a flat surface[116]. In Eqn. (3-3) γ_{sg} is the surface energy between solid and gas phases, γ_{sl} is between the solid and liquid phase, and γ_{lg} is between the liquid and gas phase. Rather, the SiC layer is wettable (i.e. $\theta < 90°$) by molten Si and is the primary driving force of infiltration in porous carbon [117].

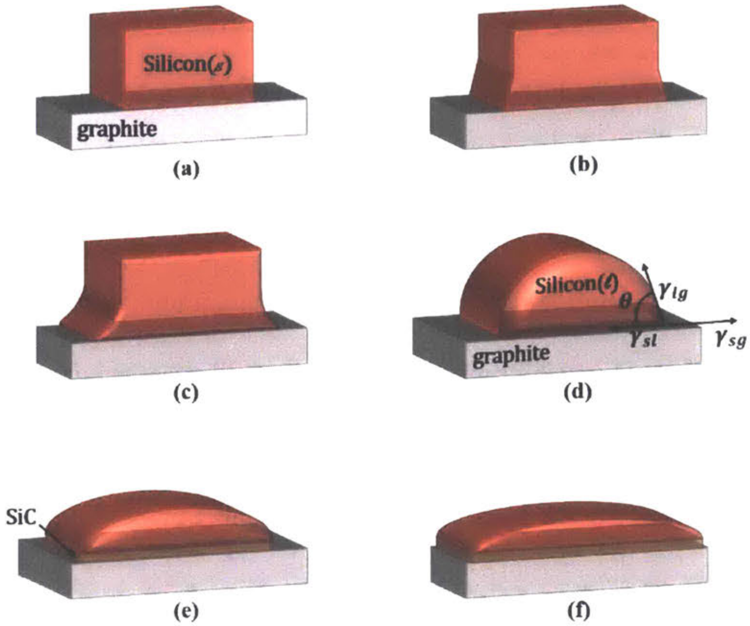

Figure 3-4. Wetting process of silicon on graphite from solid to liquid phase transition. Silicon begins as a solid (a), starts melting (b), begins forming a contact angle (c) and becomes pure liquid (d). Upon formation of silicon carbide layer (e) spreading begins, followed by the final contact angle and stabilization (f).

Numerous experiments have been performed characterizing the reaction kinetics until equilibrium is reached and characterizing the wetting angle by the sessile method, in which a drop of molten silicon is placed on a graphite surface. Once equilibrium is reached, within seconds to a minute, the rate of further reaction between Si and graphite is greatly reduced by the interfacial layer of SiC existing on the order of micrometers[112,117–120].

Another key requirement of the silicon container is that it must be resistant to oxidation, assuming TERS is operated in a normal oxidizing environment. Graphite reacts with oxygen to form carbon monoxide (CO) and/or carbon dioxide (CO_2), depending on graphite temperatures and oxygen flow rate. The rate of reaction further depends on graphite porosity and surface roughness. In general however, for the temperatures considered here (around 1400°C) the reaction of graphite with oxygen is controlled by a boundary layer. The dependence of reaction rate on temperature, and thus reaction regime, is provided in Figure 3-5a. The sample was a high impurity graphite IG-110 tested under 20 ml/min of dry air at room temperature. Oxidation rates for bare graphite of the same composition and oxygen flow rate is provided in Figure 3-5b. In the boundary layer regime, a coating such as silica or silicon carbide may be used to protect the graphite from ingress of oxygen, most commonly studied in the field of high temperature reactors[121–125]. For example, testing has been performed on SiC coatings which were able to withstand thermal cycling and prolonged periods at temperatures up to 1600°C[122]. Future work will consist of testing different coatings that can protect graphite from oxidation without hindering the rate of radiative heat transfer.

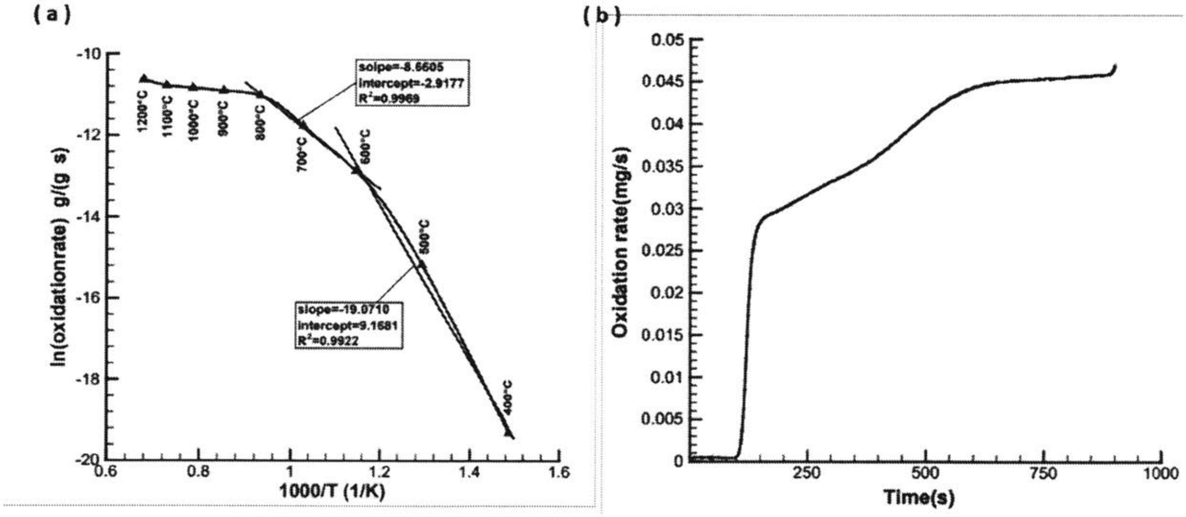

Figure 3-5. Oxidation of high-impurity IG-110 graphite. (a) controlled regimes of graphite oxidation with respect to temperature, and (b) oxidation rate of graphite held at 1500°C. Figure adapted from Xiaowei et al. [126]

Having determined graphite as the ideal container material from which radiation shall emanate, we proceed to discussion of the HTF tubes that shall absorb the radiation. The material for HTF tubes in supercritical boilers is determined based on the maximum operating temperature and pressure, keeping material cost at a minimum as well. We can simply use the same material for the HTF pipes as that in supercritical boilers, namely P91 or P92 steel alloy. Boilers typically adopt one of two configurations for the waterwall, one in which metal strips are welded between the tubes, known as a membrane wall, depicted in Figure 3-6(a), and one in which the tubes are not connected, with a reflective surface behind the tubes Figure 3-6(b). The strips welded between the tubes behave as heat concentrators, conducting any incident radiation into the tubes. For the following system analysis, we adopt the configuration of Figure 3-6(a) to enhance heat transfer to the HTF. The strips are composed of the same material as the tubes, P92 ferritic steel alloy.

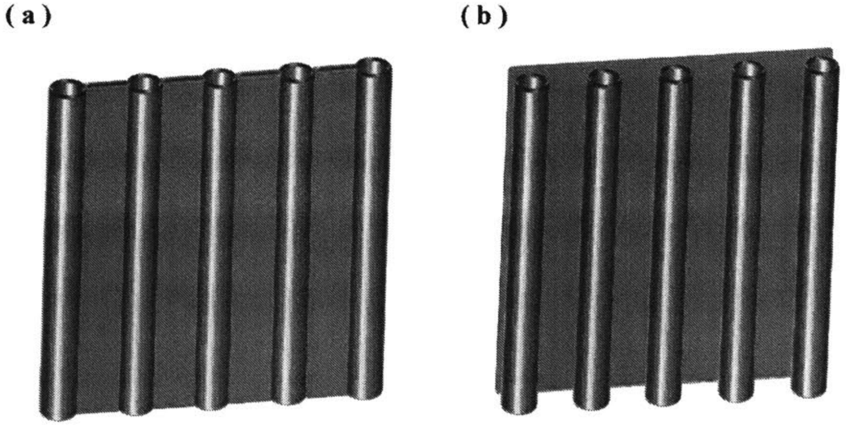

Figure 3-6. Waterwall configurations in typical boilers. (a) Tubes are connected by strips of metal aka membrane wall. (b) Tubes are not connected, with a reflective surface behind the tubes.

3.4. Non-negligible Modes of Heat Transfer

Thus far, we have elemental silicon as the phase change material, cartridge heaters immersed in the silicon, graphite enclosing the silicon, and a bank of finned heat transfer tubes also known as a membrane wall, illustrated in Figure 3-7.

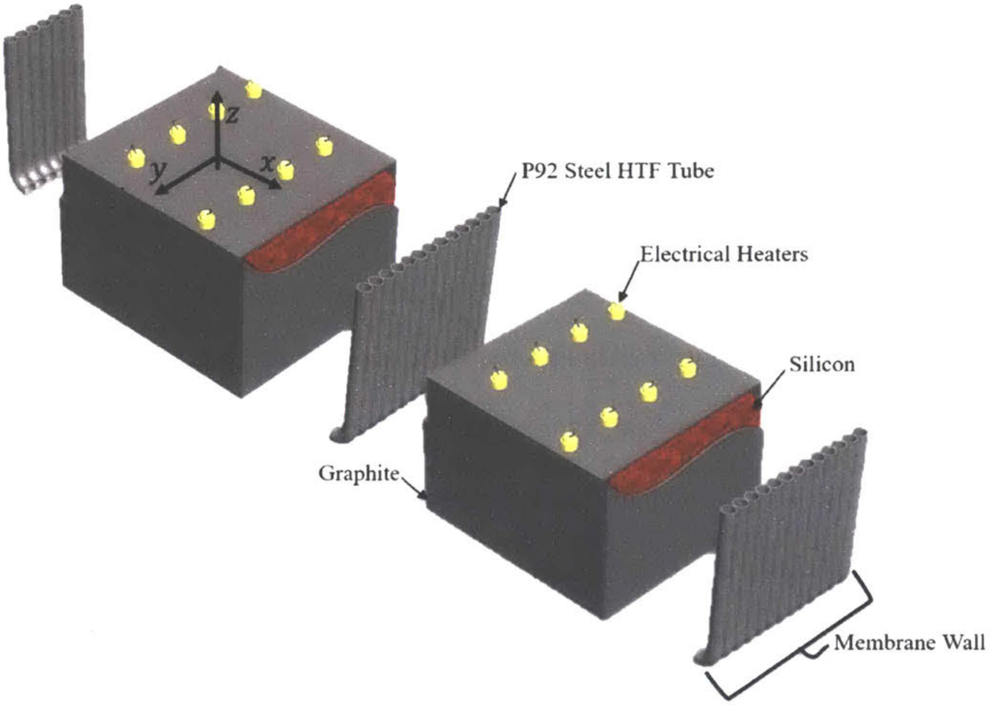

Figure 3-7. Assembly of components in radiative TERS. To charge TERS, electrical heaters such as immersed cartridge heaters are implemented. The energy from the heaters is stored in the form of latent and sensible heat in silicon near its solid to liquid phase change temperature. During hours of discharge, radiative heat transfer from TERS to the bank of tubes produces, for example, supercritical water. In a real system, multiple units of silicon and water tube banks are present, with all components contained within an enclosure open to atmospheric pressure.

To estimate the system cost, the number of required HTF tubes (N) must be known. This quantity is a function of the HTF mass flow rate ($\dot{m}$) and heat transferred (Q) to the HTF by $N = Q/(\dot{m}\Delta h)$ where Δh is the change in enthalpy of the HTF. The HTF mass flow rate is known within some range of Reynold's number such that an acceptable heat transfer coefficient is obtained following correlations for supercritical water, to be discussed. Therefore, the heat transferred from the molten silicon to membrane wall is the central problem to be solved before system cost can be estimated.

To start, let us consider the different heat transfer processes occurring within each component. During discharge of the silicon, a solidification front propagates from the inner graphite surface towards the center of silicon, illustrated in Figure 3-8. The speed, *ds/dt*, at which this solidification front moves is determined by the heat transferred by radiation to the membrane wall, further a function of the HTF flowing through the tubes. Since the initial and final temperature of the water will vary in the z-direction, we expect *ds/dt* to also be a function of z- as illustrated in Figure 3-8(b). Therefore, there will be a larger temperature gradient from the edge of the solidification front to the edge of graphite at $z(0)$ versus $z(>0)$. This leads to conduction heat transfer in both the x- and z- direction, i.e. $Q(x,z,t)$. If the fins (Figure 3-8(a)) are designed such that they are isothermal with a temperature close to that of the tubes, then we can assume that any conduction in the y-direction within the silicon is negligible.

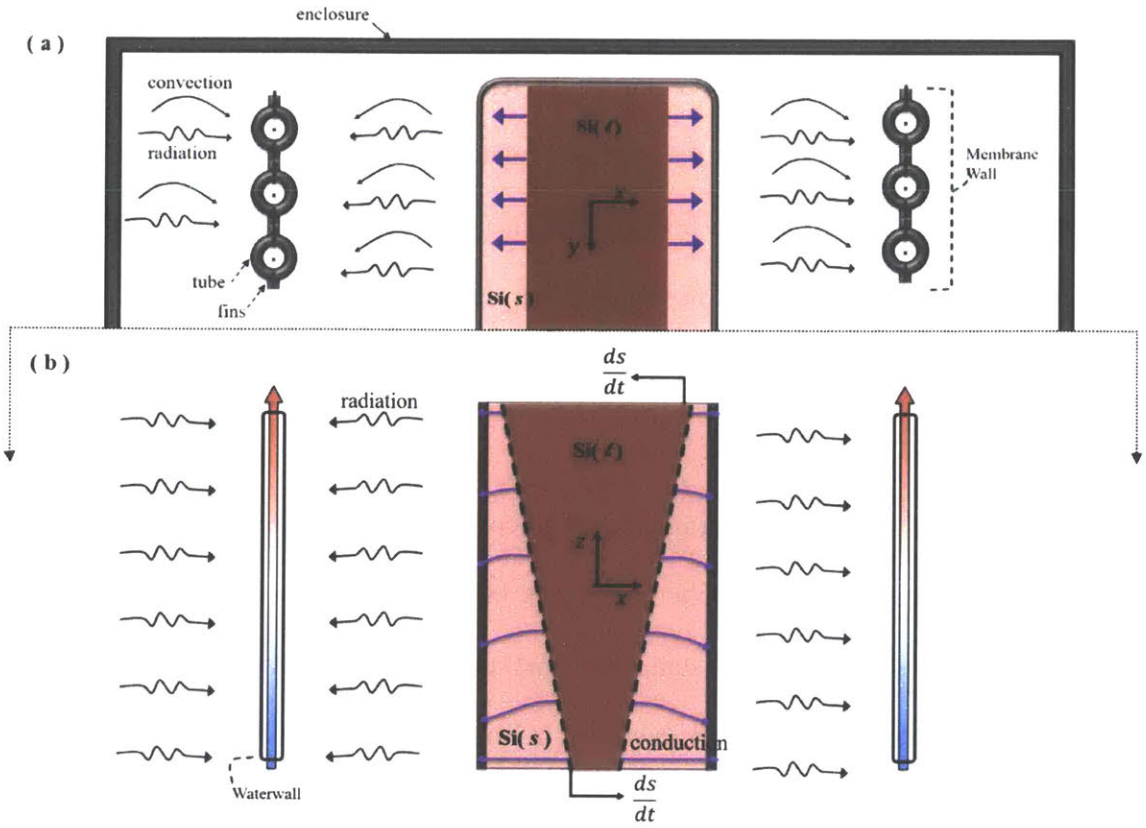

Figure 3-8. Illustration of various modes of heat transfer occurring during system discharge. (a) Top cross-sectional view of system taken at arbitrary position in z-direction. (b) Side cross-sectional view of system at time t when solidification front is at $\pm s$.

It should be noted that natural convective effects within silicon are neglected, resulting in a conservative estimate for the overall heat transfer rate from the silicon to membrane wall. In general, heat transfer performance of energy storage during phase transitions from solid to liquid have been studied and the importance of convection versus conduction in the process has been discussed[127–129]. In the case of Si, this assumption is valid considering the high value of thermal conductivity and consequently low Rayleigh number[130–133]

The molten silicon is at its phase change temperature (T_m) of 1414°C while the HTF is at a temperature between 100°C and 570°C. Given the temperature difference between Si and HTF ($\Delta T \geq 800$), there will be a significant rate of heat transfer through radiation and a contribution by natural convection between the two bodies. The heat transferred to the membrane wall will eventually be transferred to the HTF, heating water to supercritical temperatures.

3.4.1. Phase Change in Silicon

Currently, the rate of heat transfer through solid silicon is two-dimensional and time-dependent, where we have assumed that the molten silicon is initially and uniformly at its phase change temperature and thus has zero resistance to heat transfer (or equivalently infinite thermal conductivity). Therefore, heat transfer in silicon occurs in the solid phase only. In reality, there will be a small temperature gradient across the molten silicon with a boundary layer at the interface between solid and molten silicon.

We can estimate the upper bound of system cost by estimating the lower bound of heat transfer in the system. In approaching the lower bound of heat flux, the contribution of conduction in the z-direction through the solid silicon is neglected, as illustrated in Figure 3-9. Conduction from the upper region of silicon to the lower region will only enhance the heat transfer rate from the silicon to membrane wall, since the temperature difference between the silicon and membrane wall will be greater than the difference when conduction in the z-direction is neglected.

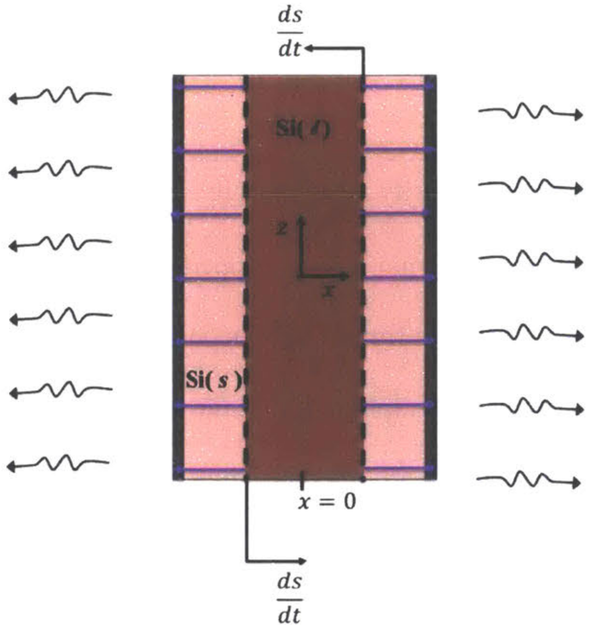

Figure 3-9. Illustration of heat transfer through silicon following initial simplification. Conduction in the z-direction is neglected to simplify 2D conduction into 1D conduction.

This then reduces the problem to a one-dimensional moving boundary problem, known as the Stefan problem[134]:

$$\rho_s c_{p_s} \frac{\partial T_s}{\partial t} = k_s \frac{\partial^2 T_s}{\partial x^2} \tag{3-4}$$

with an initial condition of

$$T_s(x,t) = T_m \ for\ x > 0, t = 0, \tag{3-5}$$

boundary condition

$$-k_s \frac{dT(0,t)}{dt} = q_{gr}, \tag{3-6}$$

and continuity conditions at the moving boundary

$$T_s(s,t) = T_m \ for\ t > 0 \tag{3-7}$$

$$\rho_l h_L \frac{ds(t)}{dt} = k_s \frac{\partial T_s}{\partial x}\bigg|_{s(t)} \tag{3-8}$$

in which ρ_s, c_{p_s}, k_s and T_s are the density, heat capacity, thermal conductivity, and temperature of solid silicon, assuming invariant thermophysical properties of silicon in the liquid or solid. The boundary condition states that the heat flux by conduction through the silicon must be equal to the heat flux by conduction through the graphite, q_{gr}, at the silicon-graphite interface. In Eqn. (3-8), ρ_l is the density of molten silicon and all other variables are defined as before.

Often, to obtain rough estimates of phase change processes, the quasi-static approximation is used to simplify the Stefan problem such that the energy equation in silicon now becomes one of steady-state conduction, i.e. Eqn. (3-4) becomes

$$0 = k_s \frac{\partial^2 T_s}{\partial x^2} \tag{3-9}$$

The Stefan number (during discharge) is defined as $Ste = c_{p_s}(T_C - T_D)/h_L$, with all parameters defined previously in Chapter 2.3. For silicon, the charged temperature T_c is 1500°C and the discharged temperature T_D is around 1400°C, resulting in a Stefan number on the order of ~10^{-2} which is less than the requisite 10^{-1} to justify the use of the quasi-static approximation, implying that the effects of sensible heat are negligible relative to those of latent heat. While the equation defining the temperature distribution in solid silicon is now time-independent, the solidification interface condition is retained which itself is time-dependent and used to estimate the position and velocity of the interface[134].

This system of equations allows us to determine the interface position $s(t)$ through the boundary and initial conditions, and thus temperature distribution in the solid silicon as a function of x, $s(t)$, and $T_{gr\text{-}si}(t)$ where $T_{gr\text{-}si}$ is the temperature at the interface of graphite and silicon. Although we have already made some approximations to simplify the analysis, numerical methods must still be applied to evaluate the above equations. The conduction through graphite is dependent on radiation from the graphite surface, which complicates the analysis of $s(t)$. As a first approximation, we can use scaling analysis to solve Eqn. (3-8) for s(t) as $s(t) \cong \sqrt{2k(T_C - T_m)/\rho_L h_L}$. Future work will consist of numerically solving for the transient temperature profile in silicon during discharge by using COMSOL or applying the finite-difference time-domian (FDTD) method in MATLAB.

The time at which the solidification front has reached the silicon core represents the steady state regime where Eqn. (3-9) applies without any approximation made. At this point, the length of silicon is at its maximum, defined in Figure 3-10. Consequently, the heat flux through silicon is at a minimum, since the resistance to heat conduction through silicon scales as $1/l_s$.

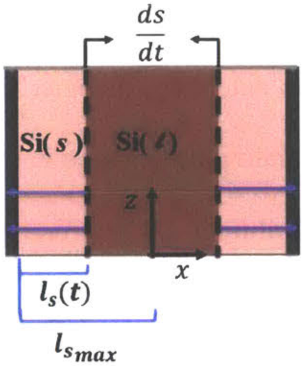

Figure 3-10. Illustration of length of silicon $l_s(t)$. Once solidification front has reached $x = 0$, $l_s(t) = l_{s_{max}}$ and thus resistance to conduction in the x-direction is at a maximum.

We can determine the lowest bound of heat transfer achievable, corresponding to the maximum number of HTF tubes necessary, by evaluating system performance when all latent heat has been discharged and silicon is in its solid state.

3.4.2. Radiation versus Natural Convection

The contained silicon and membrane wall will be close enough such that the height of each is much greater than the distance between. To avoid large hydrostatic pressures on graphite from silicon, the height H is chosen to be 5 m. If this height is at least an order of magnitude greater than the distance between the bodies, then natural convection will behave more like convection within an enclosure (i.e. air circulating between the two bodies) than convection across parallel plates. The Rayleigh number is determined by

$$Ra_s = \frac{g\beta(\overline{T_1}-\overline{T_2})H^3}{\nu^2} Pr \tag{3-10}$$

where H is the height of the water wall and contained silicon, $\overline{T_1}$ is the temperature of the graphite containing silicon averaged along the z-direction, $\overline{T_2}$ is the average temperature of the water wall, β is the thermal coefficient of expansion of air, ν is the kinematic viscosity of air, and Pr is the Prandtl number which compares momentum diffusivity to thermal diffusivity by ν/α where α is the thermal diffusivity. All properties of air are evaluated at the bulk fluid temperature, average of $\overline{T_1}$ and $\overline{T_2}$. We take $\overline{T_1}$ as 1414°C and $\overline{T_2}$ as the average of the water inlet and outlet temperature (100°C and 570°C, respectively) such that a maximum temperature difference is considered in estimating the Rayleigh number.

The Rayleigh number of air in these conditions remains on the order of $\sim 10^{10}$ with increasing water wall, resulting in mixed boundary-layer type flow. This type of flow most notably features laminar to turbulent boundary layers along the vertical walls (graphite surface and membrane wall), and recirculating core cells[135]. The turbulent case greatly complicates the analysis though variation in the resulting heat transfer coefficient is not significant. The Nusselt number correlation used here is as follows[136]

$$Nu_H = 0.620 Ra^{\frac{1}{4}} \qquad (3\text{-}11)$$

valid for differentially heated and cooled vertical walls that can be modeled as isothermal, with $0.3 < Ra < 6x10^{10}$. The heat transfer coefficient can then be determined as $h = Nu_H\, k/H$ where k is the thermal conductivity of air evaluated at the average temperature. Results are plotted in Figure 3-11.

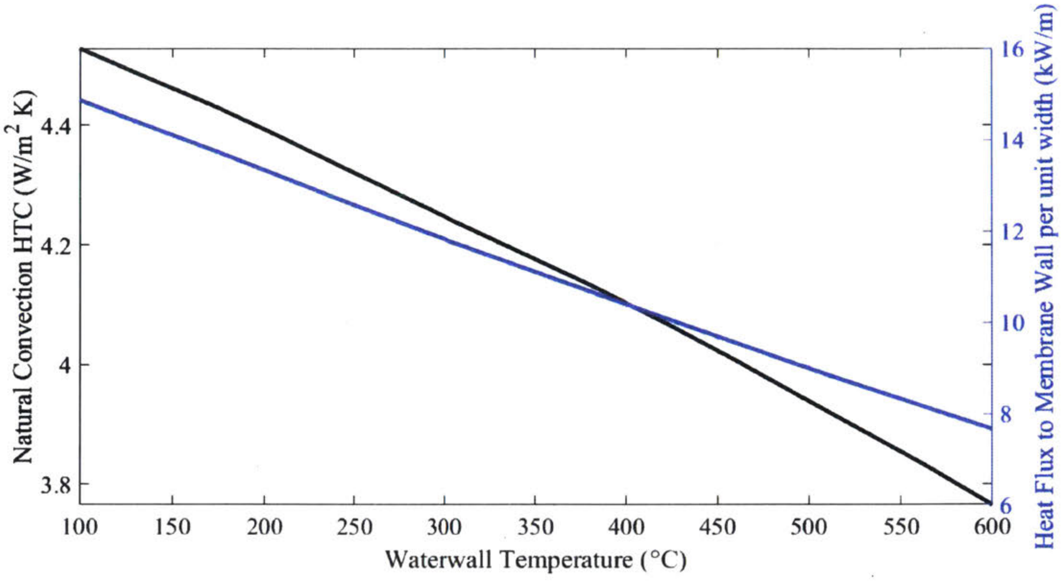

Figure 3-11. Approximate heat transfer coefficient for natural convection between the contained silicon and membrane wall. Rate of heat transfer per unit width of membrane wall is defined according to temperature difference between bulk fluid temperature and membrane wall temperature.

To compare this natural convection heat transfer coefficient to radiative heat transfer, a radiative heat transfer coefficient must first be estimated. Due to the large temperature difference between the graphite surface and the water wall, the radiative heat transfer coefficient $\bar{h}_{rad}$ cannot be linearized. Rather, the coefficient is approximated as,

$$\bar{h}_{rad} = \frac{\sigma\left(\overline{T_1}^4 - \overline{T_2}^4\right)}{\frac{1-\epsilon_1}{\epsilon_1} + \frac{1}{F_{1-2}} + \frac{1-\epsilon_2}{\epsilon_2}} / (\overline{T_1} - \overline{T_2}) \qquad (3\text{-}12)$$

where the graphite surface is denoted by a subscript of 1, and the membrane wall by subscript 2, ϵ is emissivity, σ is the Stefan-boltzmann constant, and $F_{1\text{-}2}$ is the view factor between the graphite surface and membrane wall. By considering both the membrane wall and the graphite surface as isothermal, at their respective average temperatures, this is a highly approximate value used solely to compare the significance of natural convection versus radiation heat transfer. By this isothermal assumption, the view factor is that of parallel plates, $F_{1\text{-}2} = 1$. The emissivity of graphite (ϵ_1) at 1400°C is 0.87 and that of the membrane wall ϵ_2 is 0.80. [137,138], where we invoke the diffuse gray surface approximation in which the emissivity $\epsilon(\lambda, \mathrm{T})$ is independent of wavelength and temperature. Using the same values for $\overline{T_1}$ and $\overline{T_2}$ as above in calculating the natural convection heat transfer coefficient, $\bar{h}_{rad}$ is approximately $\approx$ 290 $\mathrm{Wm^{-2}K^{-1}}$. We conclude that natural convection is negligible compared to radiative heat transfer.

3.4.3. Radiation from Graphite Surface

In analyzing the heat transfer from the solid silicon, through the graphite container, we begin with a control volume analysis on a differential element containing silicon and graphite. The Poljak approach to the net-radiation method is adopted to derive energy balance equations describing the temperature distribution in the graphite and membrane wall[139].

An overall energy balance on the control volume enclosing silicon and graphite considers the energy quantities incident upon the surface, and energy quantities leaving the control volume. Illustrated in Figure 3-12, *G* is the incident radiative flux also known as irradiation, and *J* is the outgoing radiative flux also known as the radiosity.

An overall energy balance for $\mathrm{CV_1}$ is expressed as

$$0 = G_1(y)dA_1 - J_2(y)dA_1 + q|_x dA_1 \tag{3-13}$$

Upon substitution of Fourier's law, the energy balance equation becomes

$$0 = G_1(y)dA_1 - J_1(y)dA_1 - kdA_1\frac{dT_1}{dx} \tag{3-14}$$

Currently, there are three unknowns in Eqn. (3-14) : G_1, J_1, and $T_1(x)$. We may reduce the number of unknowns by defining J_1 in terms of $T_1(x)$ and G_1:

$$J_1(y)dA_1 = \epsilon_1\sigma T_1^4(y)dA_1 + [1 - \epsilon_1]G_1(y)dA_1 \tag{3-15}$$

where we have assumed diffuse-gray surfaces, and that radiative properties are independent of temperature. Eqn. (3-15) is simply a statement of energy conservation at the surface of CV_1, stating that all outgoing radiation must be the sum of emitted radiation and reflected radiation.

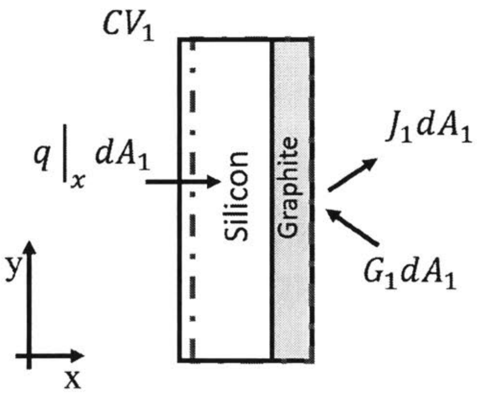

Figure 3-12. Energy balance of control volume analysis on contained silicon. Heat transfer by conduction, q, occurs through a differential cross-sectional area dA_1

Upon substitution of Eqn. (3-15), Eqn. (3-14) becomes

$$0 = G_1(y)dA_1 - [\epsilon_1\sigma T_1^4(y)dA_1 + [1-\epsilon_1]G_1(y)dA_1] - kdA_1\frac{dT_1}{dx} \tag{3-16}$$

Simplifying and solving for G_1, the resulting expression is

$$G_1(y) = \sigma T_1^4(y) + \frac{k}{\epsilon_1}\frac{dT_1}{dx} \tag{3-17}$$

3.4.4. Conduction through Membrane Wall

The membrane wall enhances heat transfer to the HTF by conducting incident radiation into the tube. The inner radius, r_i, of the tube is 38 mm, the thickness of which is 6.5 mm, chosen according to typical membrane wall tube dimensions[140]. To determine whether conduction in the x-direction of the strips is negligible compared to radiation, the Biot number (Bi) may be calculated, where Bi is defined as the ratio of internal resistance to external resistance. For the strips between the tubes, Bi is expressed as

$$Bi_x = \frac{\frac{\left(\frac{t}{2}\right)}{kA}}{\frac{1}{\bar{h}_{rad}A}} = \frac{h_{rad}t}{2k} \tag{3-18}$$

where t is thickness, A is strip area in the zy-plane, k is thermal conductivity, and $\bar{h}_{rad}$ is defined in Eqn. (3-12). The thickness is initially set to 15 mm and later optimized. The thermal conductivity is ≈27 $Wm^{-1}K^{-1}$, that of P92 steel around 500°C [141]. Using these values, the resulting Biot number is 0.08 << 1, indicating that resistance to conduction in the transverse direction is much less than resistance to radiation, and therefore we may assume the strip is isothermal in the thickness direction.

As illustrated in Figure 3-16, there will be conduction in both the y- and negative z-direction as a result of the HTF temperature difference along the z-direction. However, conduction in the y-direction will be much more significant than that in the z-direction, since the length for conduction in the z-direction (H) is much larger leading to a proportionally larger resistance. The height of the membrane wall, H, is 5 m. The length of the strip in y-direction, L_f, is initially set to 20 mm and later optimized. As a first approximation, we may ignore conduction in the z-direction and model the strips as fins with one-dimensional conduction.

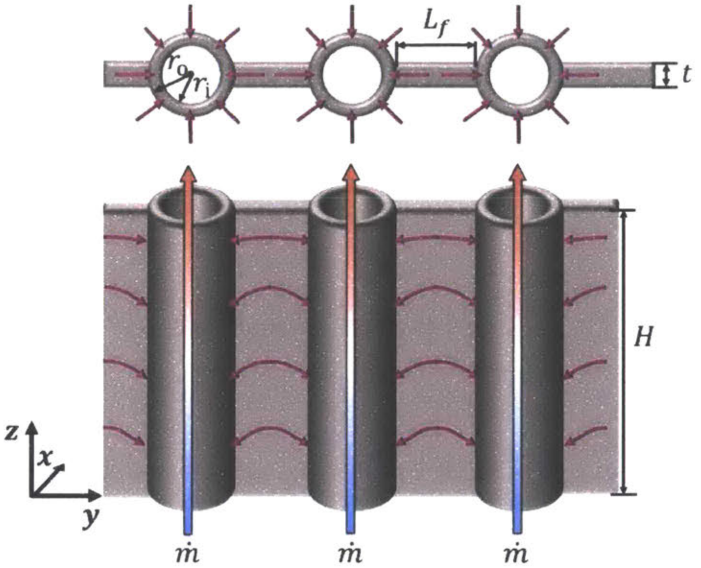

Figure 3-13. Conduction through membrane wall. As a result of forced convection, water will enter at a mass flow rate $\dot{m}$ with a higher temperature at the outlet than inlet, leading to higher temperatures in the fin along the direction of HTF flow.

3.4.5. Radiation to Membrane Wall

Similar to the control volume analysis of section 3.4.3, we begin with an overall energy balance considering the energy quantities incident upon the surface, and energy quantities leaving the control volume of the membrane wall, provided in Figure 3-14. As radiation is received on both sides of the membrane wall, the control volume contains only half the thickness by symmetry.

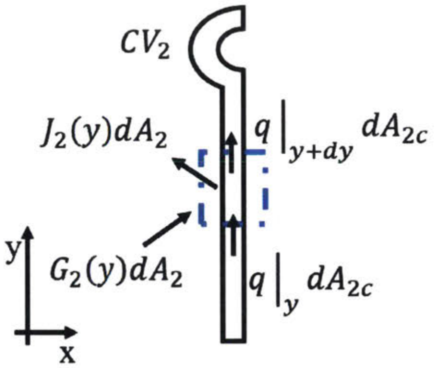

Figure 3-14. Energy balance of control volume analysis on membrane wall.

The energy balance for CV_2 is given by

$$0 = G_2(y)dA_2 - J_2(y)dA_2 + q|_y dA_{2c} - q|_{y+dy} dA_{2c} \quad (3\text{-}19)$$

where dA_2 is the differential surface area of CV_2 and dA_{2c} is the differential cross-sectional area of CV_2. After taylor expanding $q|_{y+dy}$ about y and substituting fourier's law $q = -k\ dT/dy$, Eqn. (3-19) becomes

$$0 = G_2(y)dA_2 - J_2(y)dA_2 + k_2\ dA_{2c}\frac{d^2T_2}{dy^2}dy \quad (3\text{-}20)$$

The radiosity can be defined in terms of T_2 and G_2 as

$$J_2(y)dA_2 = \epsilon_2\sigma T_2^4(y)dA_2 + [1-\epsilon_2]G_2dA_2 \quad (3\text{-}21)$$

Substituting this expression for radiosity into Eqn. (3-20) and rearranging, we obtain an expression for G_2 as a function of T_2.

$$G_2(y)dA_2 = \sigma T_2^4(y)dA_2 - \frac{k_2}{\epsilon_2}\, dA_{2c} \frac{d^2T_2}{dy^2} dy \qquad (3\text{-}22)$$

3.4.6. Forced Convection

Forced convection heat transfer characteristics in the case of water to supercritical water varies considerably along the length of the tube, due to the properties of water varying near the pseudocritical point as shown in Figure 3-15. The Nusselt number correlation applicable below and near the pseudocritical point is therefore different than the correlation applicable near the pseudocritical point and above.

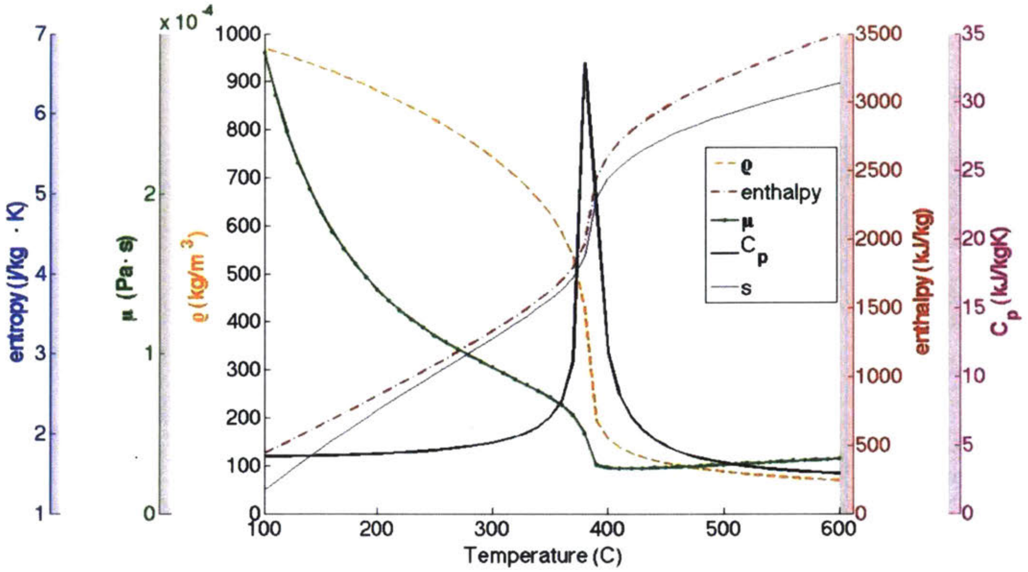

Figure 3-15. Properties of water upon transition to the supercritical state. Data from NIST Chemistry for water at 220 bar.

Within the temperature range of 100°C to 350°C, a standard Nusselt correlation may be used applicable to turbulent flow in smooth pipes within a Reynold's number range of $10^4 \leq Re_D \leq 10^6$ where the subscript denotes the diameter as the characteristic length, and for a Prandtl number (Pr) within $0.5 \leq \mathrm{Pr} \leq 200$. The Petukhov formula is used[142],

$$Nu_D = \frac{\left(\frac{f}{8}\right)Re_D Pr}{1.07+12.7\sqrt{\frac{f}{8}}\left(Pr^{\frac{2}{3}}-1\right)}\left(\frac{\mu_b}{\mu_w}\right)^{0.11} \qquad (3\text{-}23)$$

where μ_b is the dynamic viscosity evaluated at the bulk fluid temperature, μ_w is the dynamic viscosity evaluated at the wall surface temperature, and f is the friction factor estimated by the Filonienko relationship[143]:

$$f = (1.82 \log Re_D - 1.64)^{-2} \tag{3-24}$$

The correlations developed for supercritical water flow are highly dependent on heat flux, pressure, Reynold's number, mass flux and temperature. Here, a correlation by Mokry et al. is implemented to estimate the Nusselt number (Nu_b) of supercritical water valid for a mass flux G within 200-1500 kg/m^{2}s , heat flux q less than 1250 kW/m^2, pressure of 24 megapascals (MPa), and initial temperature between 320-350°C.

$$Nu_b = 0.0061\ Re_b^{0.904} \overline{Pr_b}^{-0.684} \left(\frac{\rho_w}{\rho_b}\right)^{0.564} \tag{3-25}$$

In Eqn. (3-25), $\overline{Pr_b}$ is the average Prandtl number of the bulk fluid, Re_b is the bulk Reynold's number, ρ_w is the fluid density at the wall temperature, and ρ_b is the fluid density at the bulk fluid temperature[18,144].

The wall temperature must be known to calculate properties in the above correlation for supercritical water. Therefore we estimate the temperature difference between the wall and bulk fluid temperature to be 50°C, then later confirm this assumption. The convection coefficient $\bar{h}$ can then be calculated as $\bar{h} = Nu_b(T)k(T)/2r_i$ in which k is the thermal conductivity of the fluid and r_i is the inner radius of the tube, 19 mm.

The variation in heat transfer coefficient with respect to temperature is shown in Figure 3-16 for different Reynold's number, using the Petukhov formula up to 340°C and the correlation by Mokry for temperatures above 340°C.

The Reynolds number and mass flux of HTF is a function of the mass flow rate $\dot{m}$, which depends on the length L through which water will be heated from 100°C to 570°C. Mass flux is defined as $G = \dot{m}/\pi r_i^2$ where the mass flow rate can be determined by an energy balance on the tube, resulting in the following differential equation

$$\dot{m}(h|_{z+\delta z} - h|_z) = q''2\pi r_i \delta z \qquad (3\text{-}26)$$

where h is fluid enthalpy, q'' is heat flux, and δz is a differential element along the tube. The change in enthalpy is defined as the difference in fluid enthalpy at the tube outlet and tube inlet, $\Delta h = h_o - h_i$, where h_o is the enthalpy of water at 570°C and h_i is the enthalpy at 100°C. Following integration and substitution for G, the required length of each tube can be simply expressed as a function of the mass flux,

$$L = \frac{2q''G}{r_i \Delta h} \qquad (3\text{-}27)$$

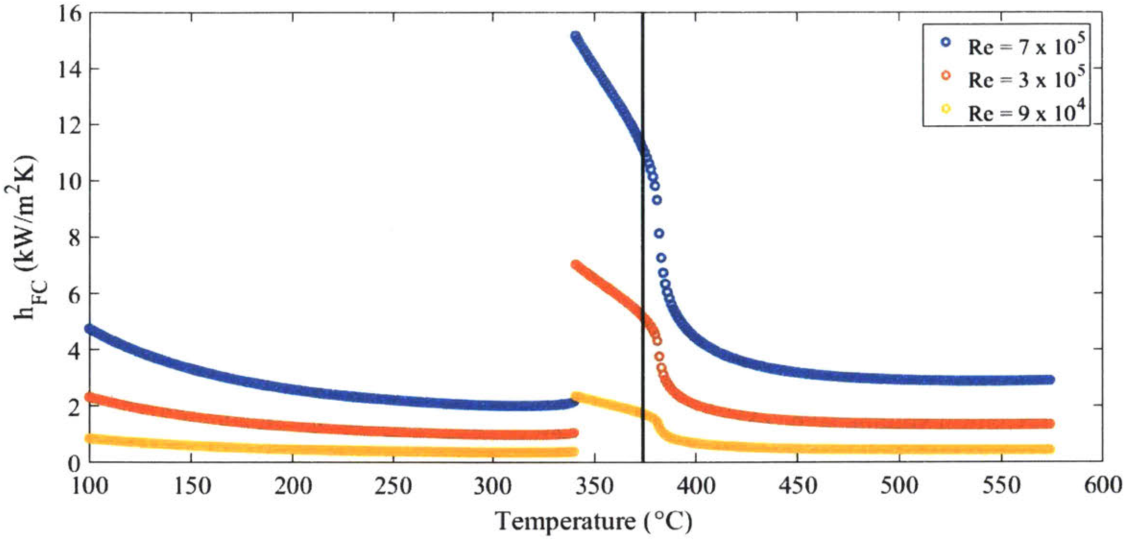

Figure 3-16. Forced convection heat transfer coefficient with respect to fluid temperature. Dotted line represents the temperature at which water transitions to supercritical state. Thermophysical properties of water at 24MPa from NIST Chemistry.

A Reynolds number of $3x10^5$ is initially assumed to estimate the convection coefficient, after which the heat flux can be evaluated, and thus mass flux and length of each tube determined. We average the resulting value along the length of the tube to obtain an estimated convection coefficient of 1,830 $Wm^{-1}K^{-1}$.

3.5. Radiation between Differential Elements

Thus far, we have considered radiation from the graphite surface and membrane wall separately, defining the irradiation for the control volumes defined in Figure 3-17. However, these equations are coupled through *J* and *G*.

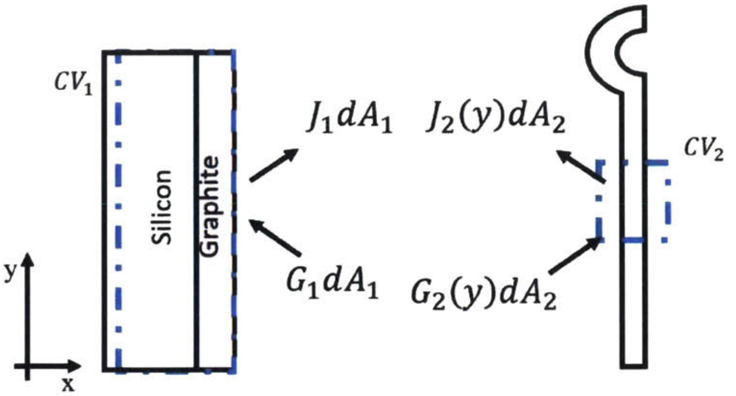

Figure 3-17. Control volume taken to perform an energy balance on contained silicon (CV_1) and fin (CV_2).

The irradiation of surface 1, $G_1 dA_1$, is equal to the radiosity of surface 2, $J_2 dA_2$, that arrives at element dA_1: This can be expressed as $G_1 dA_1 = J_2 dA_2 dF_{d2-d1}$ where dF_{d2-d1} is the view factor from differential element 2 to differential element 1. By reciprocity, $dA_2 dF_{d2-d1} = dA_1 dF_{d1-d2}$ and thus:

$$G_1 dA_1 = J_2 dA_1 dF_{d1-d2}. \tag{3-28}$$

The view factor between two differential areas, specifically from d_1 to d_2, is generally defined as

$$dF_{d1-d2} = \frac{\cos\theta_1 \cos\theta_2}{\pi S^2} dA_2 \tag{3-29}$$

where S is the length of the line between the differential surface element dA_1 and dA_2, θ_1 is the angle from the normal of differential element dA_1 to the line of length S, and likewise for θ_2 from the normal of dA_2. The geometry is provided in Figure 3-18. Since in this case, the generating lines of the differential elements are parallel, $\theta_1 = \theta_2$.

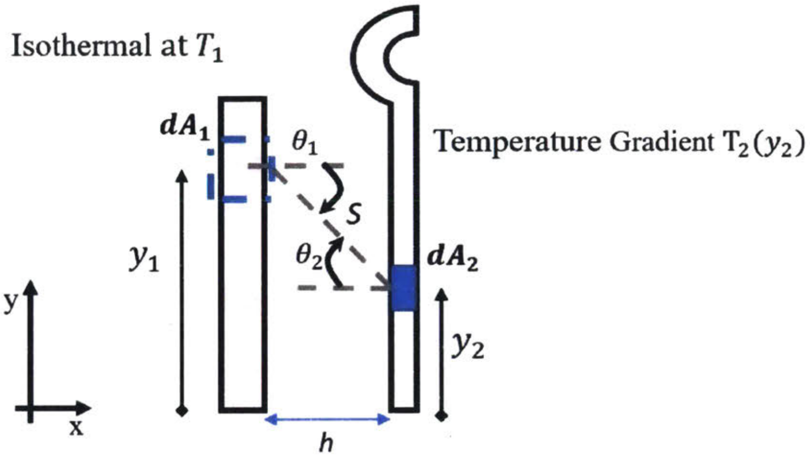

Figure 3-18. Geometric variables for derivation of view factor between a finite area and differential area.

By geometric relations, the view factor can be expressed as

$$dF_{d1-d2} = \frac{(\cos\theta)^2}{\pi S^2} dA_2 \tag{3-30}$$

where $\cos\theta = \frac{h}{S}$ and $S^2 = [h^2 + (y_2 - y_1)^2]$. Depending on the magnitude of temperature variation along each differential element, the view factor from one element to the other may be integrated up to a length within which the element is approximately isothermal. For example, if the graphite wall is found to be isothermal within a length of l, we can integrate the view factor as

$$dF_{1-d2} = \int_0^l \frac{h^2}{\pi[h^2+(y_2-y_1)^2]^2} dy_1 \tag{3-31}$$

To rigorously evaluate the heat transfer rate, we must consider the temperature variation of both the graphite surface and the membrane wall. If there is a large temperature gradient along the membrane wall in either the *y*- or *z*-direction, differential elements must be considered in evaluating the view factor, with the size of these finite elements determined by continuously decreasing them until convergence of temperature is reached. Likewise for the graphite surface.

However, we can argue that the view factor is approximately 1 by the following logic: even if the mass flow rate was set such that the largest system temperature difference in the membrane wall resulted along the direction of flow (i.e. 570°C - 100°C), this temperature difference still remains much smaller than the smallest temperature difference between the graphite surface and membrane wall (i.e. ~1300°C versus 570°C). In other words, whether the graphite surface sees the water wall at 100°C or 570°C, the heat transfer rate between the two bodies is roughly the same. Hence, we may assume that the membrane wall and graphite surface is isothermal and thus the view factor $F_{2\text{-}1}$ between the two bodies is approximately equal to that for infinite parallel plates, $F_{2\text{-}1} = 1$, as long as the distance between the graphite and membrane wall is much less than the length of each.

3.6. Approximate Heat Transfer Model during Discharge

As previously stated, the current objective is to estimate the rate of heat transfer obtainable from the contained silicon to the HTF (water, in this example) given the constraint of minimizing system cost. Such an estimate does not require solving for the precise temperature distributions within the system, which involves the fourth-order nonlinear differential equations of Section 3.4; rather, the lower bound of heat transfer can be estimated to determine the upper bound of system cost.

To summarize and expand upon, the approximations we consider in estimating the lower bound of heat transfer include:

(i) Steady-state conditions, all of silicon is in solid state
(ii) Material properties of membrane wall are temperature independent
(iii) Diffuse-gray surfaces
(iv) Strips between tubes are isothermal along *x*-direction, justified by $\mathrm{Bi}_x << 1$
(v) Local convection heat transfer coefficient between the tube and water is uniform on inner surface and an average value for the coefficient along the tube is taken
(vi) View factor between graphite surface and membrane wall is ~1 by arguments of Section 3.5
(vii) Negligible contact resistance between metal strips and tube, i.e. fin base temperature is equal to tube surface temperature
(viii) Temperature of HTF varies incrementally along the length of the tube from 100°C to 570°C

Approximation (viii) may be clarified by the depiction in Figure 3-19. Both the membrane wall and silicon unit (silicon + graphite container) are discretized in the *z*-direction such that there is a negligible temperature difference of 10°C between the inlet and outlet HTF through each differential segment of the tube.

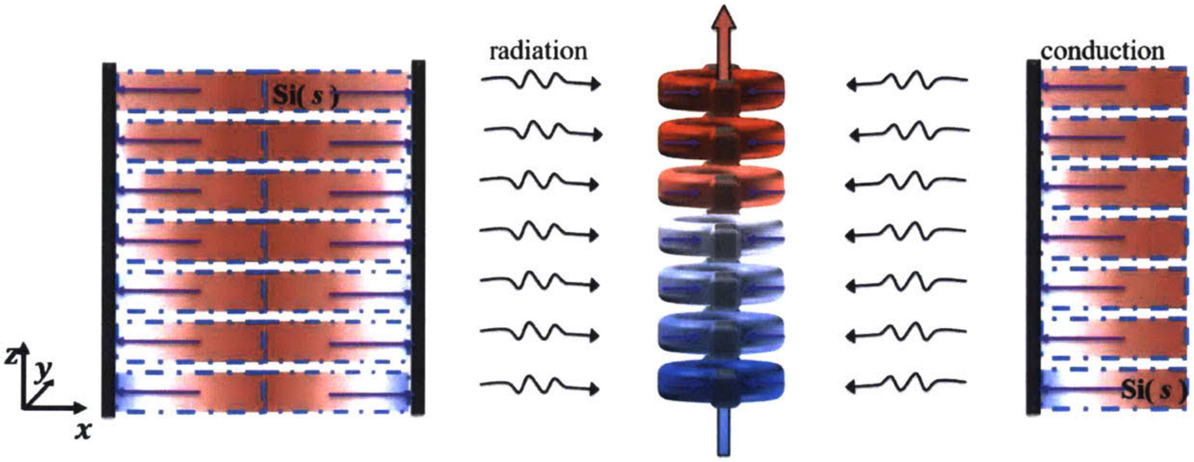

Figure 3-19. Discretized silicon unit and membrane wall. The *z*-direction is direction along which water flows and is heated to supercritical temperatures. For each discrete control volume, denoted by blue dashed lines, the energy transfer from silicon must be equal to the energy transferred to the HTF. Conduction, purple arrows, through solid silicon is radiatively transferred to the membrane wall, which is finally transferred to the HTF via forced convection.

3.6.1. System of Equations

Considering the aforementioned approximations, the lower bound of the heat transfer rate between the graphite surface and membrane wall is now expressed as

$$Q_{1-2} = \frac{\sigma T_1^4(z) - \sigma T_2^4(z))}{\frac{1-\epsilon_1}{A_1\epsilon_1} + \frac{1}{F_{1-2}A_1} + \frac{1-\epsilon_2}{A_2\epsilon_2}} \qquad (\text{3-32})$$

where the graphite surface is denoted by a subscript of 1, and the water wall by subscript 2; σT_1^4 is the blackbody emissive power of the graphite surface, where σ is the Stefan-boltzmann constant and ϵ is emissivity; σT_2^4 is the blackbody emissive power of the membrane wall. As illustrated in Figure 3-20, A is area of the emitting body also equal to the *projected* area of the absorbing body ($A_1 = A_2$).

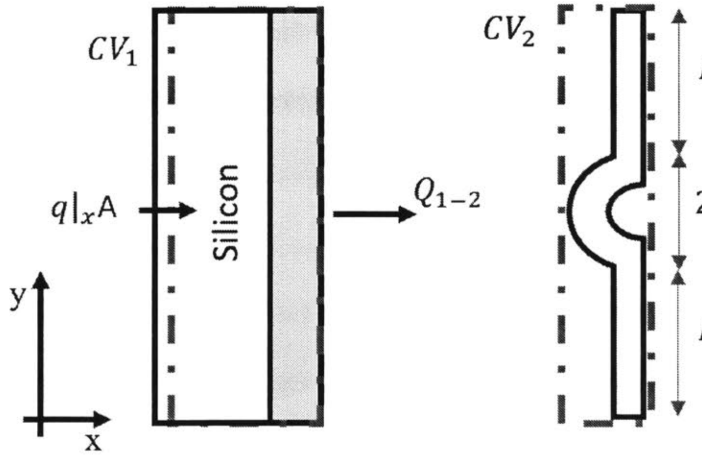

Figure 3-20. Control volume considered to approximate rate of heat transfer, Q_{1-2}, from contained silicon to membrane wall.

The temperatures T_2 and T_1 is currently unknown, though can be solved for through the following coupled energy balance equations

$$\mathrm{A}\frac{T_{Si}-T_1(z)}{\frac{l_{\mathrm{Si}}}{k_{\mathrm{Si}}}+\frac{l_{\mathrm{gr}}}{k_{\mathrm{gr}}}}-\ A\frac{\sigma\left(\mathrm{T}_1^4(z)-T_2^4(z)\right)}{\frac{1-\epsilon_1}{\epsilon_1}+\frac{1}{F_{1-2}}+\frac{1-\epsilon_2}{\epsilon_2}}=0 \qquad (3\text{-}33)$$

$$A\frac{\sigma\left(\mathrm{T}_1^4(z)-T_2^4(z)\right)}{\frac{1-\epsilon_1}{\epsilon_1}+\frac{1}{F_{1-2}}+\frac{1-\epsilon_2}{\epsilon_2}}-\pi r_i\frac{T_2(\mathrm{z})-T_{HTF_b}(z)}{\frac{r_i\ln\left(\frac{r_o}{\mathrm{r_i}}\right)}{\mathrm{k_t}}+\frac{1}{\mathrm{h}}}=0 \qquad (3\text{-}34)$$

which state that the rate of heat transfer by conduction through silicon and graphite must be equal to the rate of heat transferred radiatively from the graphite surface (Eqn. 3-33) further equal to the rate of heat transferred by conduction through the tube and forced convection to the HTF (Eqn. 3-34) Here, T_{Si} is the phase change temperature of silicon, k_{Si}, k_{gr}, and k_t are the thermal conductivity of silicon, graphite, and membrane wall, respectively, with all other variables defined as before. The known values and initial estimates discussed thus far include:

Total thickness of silicon in y-direction	$l_{Si} = 40\ cm$
Thickness of graphite container in y-direction	$l_{gr} = 15\ cm$
Thermal conductivity of solid silicon at 1414°C [101]	$k_{si} = 20\ W/mK$
Thermal conductivity of graphite at 1400°C[145]	$k_{gr} = 50\ W/mK$
Thermal conductivity of tube, P92 type steel[141]	$k_t = 27\ W/mK$

Average forced convection heat transfer coefficient	$\bar{h} = 1{,}832 \frac{W}{m^2K}$
Emissivity of graphite[137]	$\epsilon_1 = 0.87$
Emissivity of membrane wall, P92 type steel[138]	$\epsilon_2 = 0.80$

The projected area A is

$$A = 2r_o + 2L_s \tag{3-35}$$

where r_o is the outer radius of the tube and L_s is half of the tube spacer length. The dimensions of the spacers between the tubes is a design parameter, and can be chosen such that the spacers are not only isothermal in the x-direction, but also in the y-direction. Although we wish to achieve a large Q, increasing A will decrease efficiency after a certain length. By modeling the spacers as fins, characterized by the dimensionless fin parameter mL_s defined in Eqn. (3-36) below, we may determine L_s such that the spacers efficiently conduct heat to the tube.

$$mL_s = \surd(L_s^2\bar{h}_{rad}P/k_tA_c) \tag{3-36}$$

A value of $mL_s \leq 1$ is an indicator of the fin being an efficient heat dissipater such that the fin is isothermal, where in this case the fin must effectively conduct the radiation incident upon the fin into the tube. Therefore, up until some length, a longer spacer will adversely affect the performance yet that is not reflected in the expression for the rate of radiative heat transfer from the graphite surface to membrane wall since $Q_{1-2} \propto A$.

Here, $\bar{h}_{rad}$ is the heat transfer coefficient due to radiation from the graphite emitter previously defined in Eqn. (3-12), P is the perimeter of the fin per unit depth subject to radiation (2), and A_c is the cross sectional area normal to conduction ($t/2$).

The fin model is most commonly applied when an approximate, constant heat transfer coefficient is known. Therefore, mL_s is typically only a function of geometry, i.e. $mL_s \propto L_s/\sqrt{t}$. With increasing fin thickness, mL_s will decrease and hence a fin of increasing thickness and constant length corresponds to a fin approaching or maintaining isothermal conditions. Likewise, a long fin corresponds to an inefficient fin. However, in the case considered here, mL_S is largely dependent upon $T_2^4 - T_1^4$ (via $\bar{h}_{rad}$), which itself is further dependent upon L_s as a larger length leads to a higher rate of radiative heat transfer to the fins and thus higher T_2.

The rate of heat transfer given by Eqn. (3-32) can be determined by guessing reasonable dimensions for the spacer thickness and half-length such as 15 mm and 20 mm, respectively. The temperatures T_1 and T_2 are then solved for numerically by the coupled conservation equations, and mL_s is evaluated. This is done multiple times to maximize A while maintaining an mL_S of around 1. For clarity, a process flow diagram is provided in Figure 3-21.

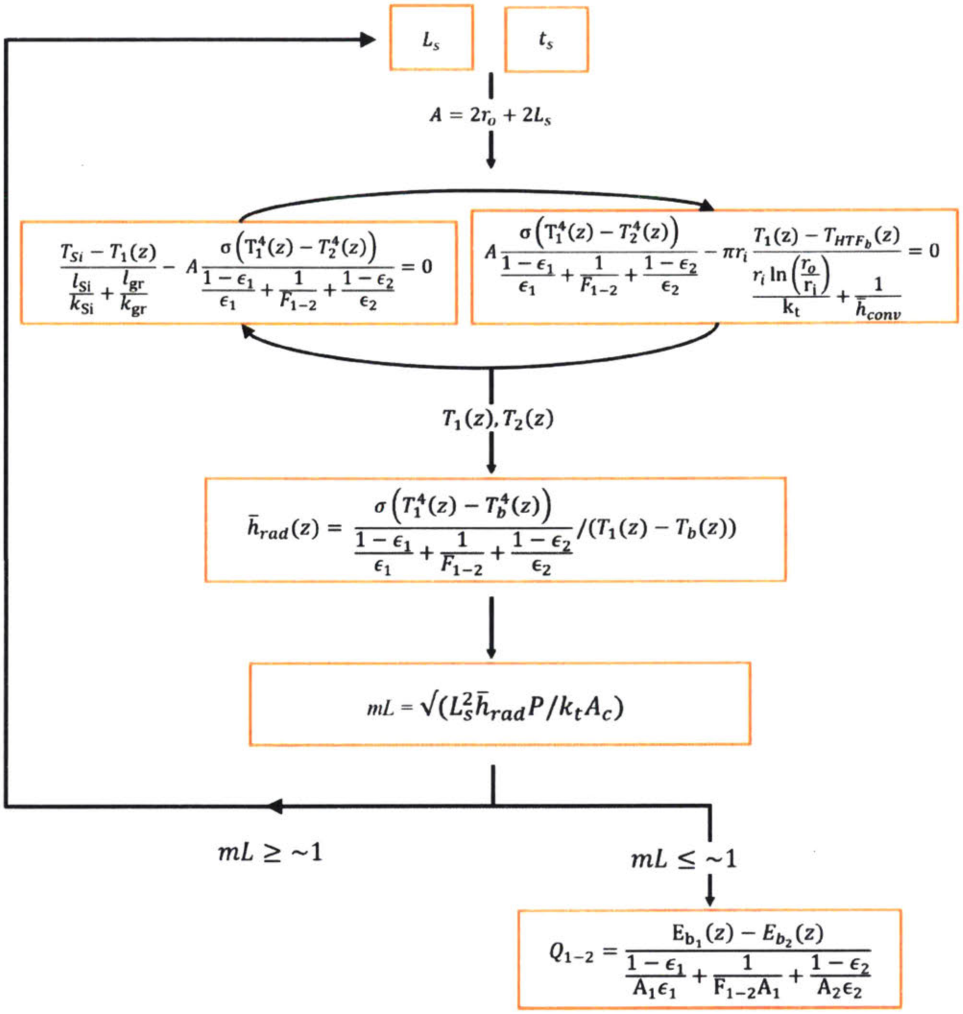

Figure 3-21. Process flow diagram implemented numerically to estimate rate of heat transfer in units of watts per meter, per control volume.

The trend of mL_s is plotted with respect to spacer half-length and thickness in Figure 3-22. The final length of the spacer is 60 mm and the thickness 20 mm, resulting in an mL_s of ~1 to ~1.4 and $Bi_x \sim 0.04$ to 0.1 along the length of the membrane wall. Considering the length of the spacer is comparable to the diameter of the tube (where the tube outer diameter is 51 mm), the fins provide a significant portion of the heat flux, and are thus a critical system design parameter.

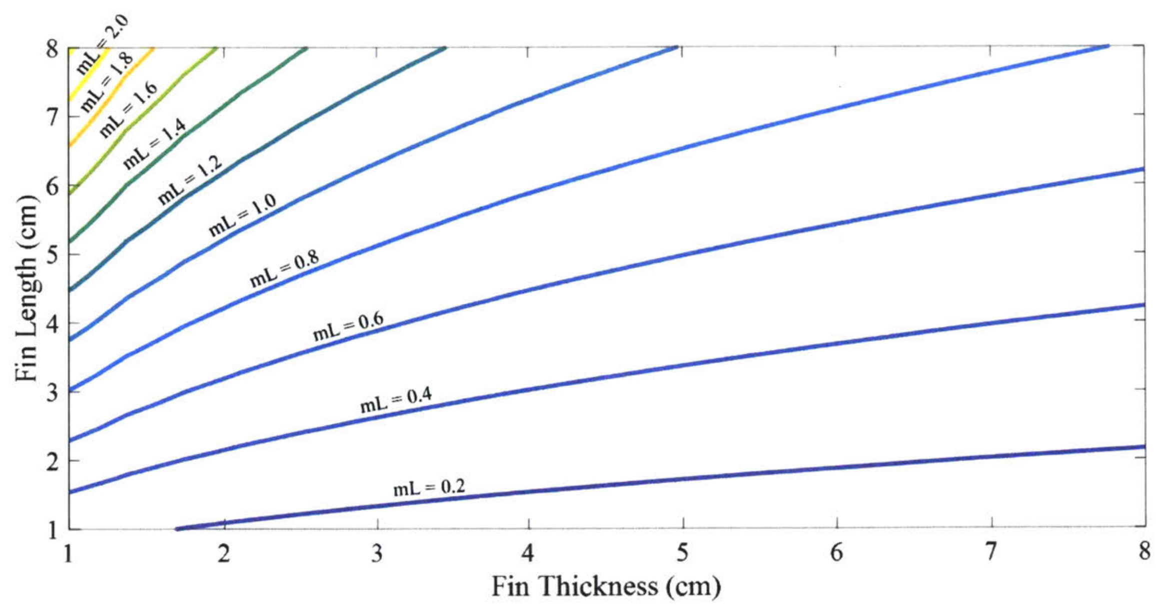

Figure 3-22. Contour plot of fin parameter with respect to fin thickness and length. The HTF temperature is fixed at the mean inlet and outlet temperature, with T_1 and T_2 solved through the coupled conservation equations.

3.6.2. Radiative TERS Performance versus Supercritical Boilers

In supercritical boilers, the heat flux provided to the water wall is not uniform, due to the nature of combustion in a pulverized coal (PC) boiler. In fact, circulating fluidized bed (CFB) boilers have been pursued to provide a more uniform heat flux in supercritical boilers. A more uniform heat flux profile reduces thermal stresses on the water wall, resulting in increased lifetime of the wall, reduced fracture of tubes, and lower maintenance costs. In Figure 3-23, we compare the performance of TERS to a typical supercritical boiler.

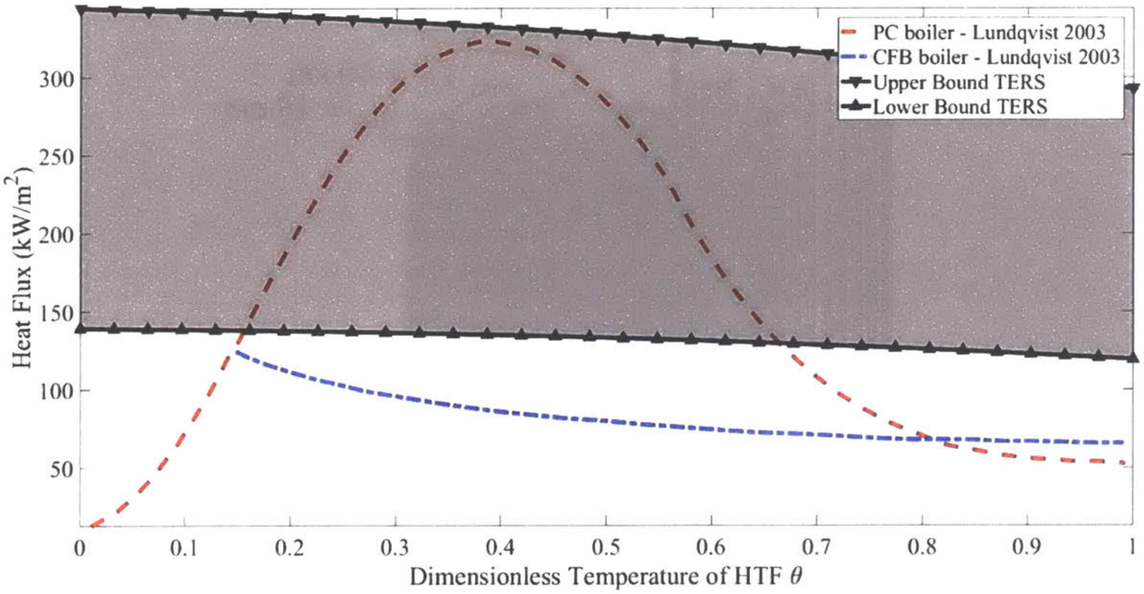

Figure 3-23. Optimized heat flux to heat transfer fluid during discharge. Dimensionless temperature is defined as $\theta = (T(x) - T_o)/(T_f - T_o)$ where T_o is the initial temperature and T_f is the final temperature of the fluid, 100℃ and 570℃ respectively for the calculated heat flux. The lower bound of heat transfer is calculated assuming all of silicon is in solid state with T_{Si} = 1414°C (end of latent heat discharge); upper bound of heat transfer is calculated assuming all of silicon is in molten state with T_{Si} = 1500°C (start of discharge). Performance of TERS is compared to that of a pulverized coal (PC) boiler and circulating fluidized bed (CFB) boiler, data acquired from Lundqist[146].

Given this lower bound of heat flux, we can determine the length of each tube by solving Eqn. (3-27) assuming an average mass flux of 210 kg $m^{-2}s^{-1}$. This results in a length of 40 m, which can be accomplished compactly through a serpentine design for a silicon unit of height 5 m, as depicted in Figure 3-24. The total number of tubes N is constrained by the total mass flux G_T required to produce 100 MWe and the average mass flux per tube, i.e. $N = G_T/G$ where G_T is equal to $(Q/\eta)/\Delta h$. This results in N≈320.

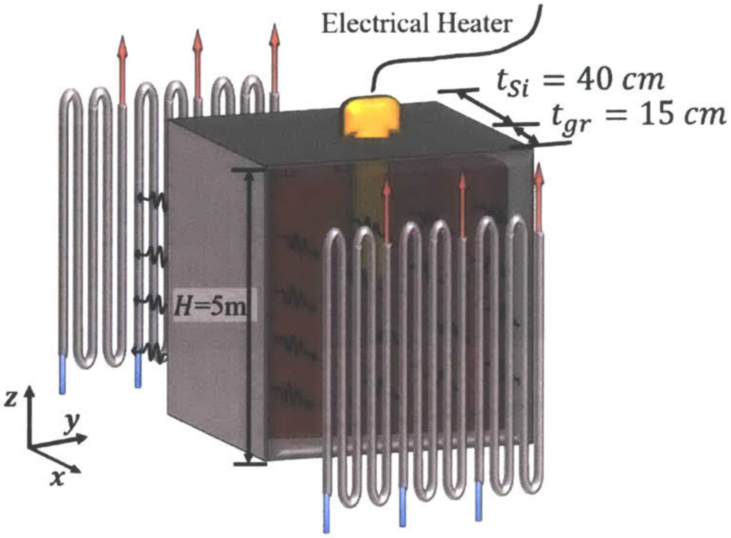

Figure 3-24. Final design and dimensions of radiation based thermal energy storage system.

The radiation based design of TERS is similar to heat transfer within a boiler, however combustion is not a requisite, thus avoiding emissions entirely during the electricity generation process. There are numerous advantages in implementing the above design for energy storage in fossil-fuel based power plants, described in Chapter 1 Section 1.1.2 and Chapter 2 Sections 2.1 and 2.3. In addition, radiation from the contained silicon is capable of supplying a comparable rate of heat transfer to the membrane wall as in PC boilers, and a more uniform heat flux to the membrane wall, increasing lifetime of the membrane wall.

3.7. Heat Transfer Analysis of Storage Conditions

To avoid heat loss through radiant energy emanating from the silicon container during hours in which discharge is not desired, insulation such as firebrick is placed between the bank of water tubes and Si container. An alternative option for insulation are radiant shields composed of low emissivity, high reflectivity materials such as type 316 polished stainless steel, nickel, chromium or tantalum. Radiation shields are an attractive option as less raw material is required compared to insulating firebrick leading to lightweight structures that can be easily be moved in and out of place. However, the issue of metal oxidation resulting in increased material emissivity remains a challenge. Oxidation can be circumvented by water-cooling the shields, though this may decrease efficiency since heat transfer through the shields increases as shield temperature decreases.

To evaluate a practical form of insulation which presents an immediate solution, an insulating composite of firebrick and microporous ceramic (collectively called insulating barrier herein) is considered as an example. Upon discharge of the thermal energy stored in silicon, the insulating barrier is removed and heat is transferred to the bank of water tubes (i.e. membrane wall), absorbed by the finned pipes and transferred to the water through forced convection. All following calculations are performed considering silicon is in molten form, thus having a thermal conductivity of around 50 $Wm^{-1}K^{-1}$.

Regardless of the form of insulation placed between the silicon and membrane wall, there will remain a temperature gradient between the two, and thus heat will be transferred from the silicon to the membrane wall and surrounding air until thermal equilibrium is reached. The volumetric heat capacity of silicon is much larger than that of the membrane wall, so we can expect that at thermal equilibrium the membrane wall will reach temperatures above 600°C if both bodies are in an isolated system. Furthermore, the pressure in the enclosure (P) will rise with temperature (T) approximately as $P(t) = m_{air}RT(t)/V$ where t is time here, m_{air} is the mass of air in the enclosure, and V is volume. Here, we have assumed that the enclosure is perfectly insulated, illustrated in Figure 3-25. Heat loss through the enclosure can be avoided by insulating the walls or building the enclosure out of insulating refractory bricks. Modeled as an isolated system, both the mass and volume are constants, where neither energy nor matter can be exchanged with the environment hence leading to an increase in pressure with increasing temperature. A rise in pressure is not detrimental if a high pressure vessel is used as the enclosure, but that does drive system cost to increase.

There are a number of ways to circumvent a temperature rise above which the membrane wall can handle, and a pressure rise within the enclosure. For example, heat transfer fluid may flow through the tubes during storage to provide heating for residential purpose, or to preheat feedwater prior to entering the boiler furnace. This results in radiation based TERS having numerous applications and markets it can excel in. Another method is convective cooling of the pipes, either actively or passively. Whereas residential water heating requires TERS to be near the residence, convective cooling does not limit the location of TERS. Pressure within the enclosure can be maintained at atmospheric pressure by a simple vent such that the system is now open. To minimize system cost, passive cooling with a ventilated enclosure will be demonstrated here as an example method of maintaining adequate temperatures and pressures during storage hours if feedwater preheating or industrial/residential water heating is not desired. A simple analysis of feedwater preheating follows.

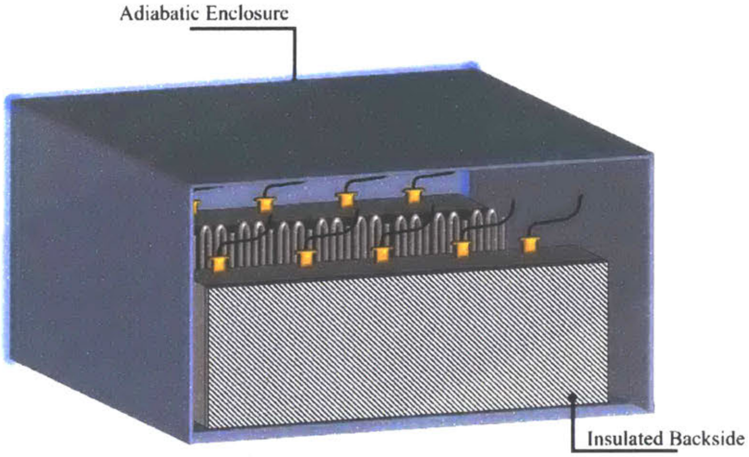

Figure 3-25. Isolated system including membrane wall, silicon unit, backside insulation, and enclosure. Silicon units facing enclosure wall are insulated on the backside, and of half thickness compared to silicon units providing both frontside and backside radiation to membrane walls.

3.7.1. Displacement Ventilation of Enclosure

Passive cooling involves displacement ventilation (also known as natural ventilation), which refers to buoyancy driven flow resulting in the displacement of air in an open system by another fluid of lower density, a well-studied topic in the field of fluid mechanics[147–150]. In this case, the enclosure in which the membrane walls and silicon units are contained can have a lower port open at all times near the floor of the enclosure and positioned near every bank as shown in Figure 3-26Figure 3-33. Ceiling ports are located above each membrane wall. The ceiling ports should be able to open and close, remaining open during hours of storage or system charging. Cool air will enter through the bottom port, displacing warmer air through the top port, and convectively cooling the pipes to some extent. Because molten silicon will be continuously providing a heat flux to the insulating barrier, we can model the barrier as a vertical heated plate, which will be of importance in the discussion of steady state conditions in Section 3.7.2.

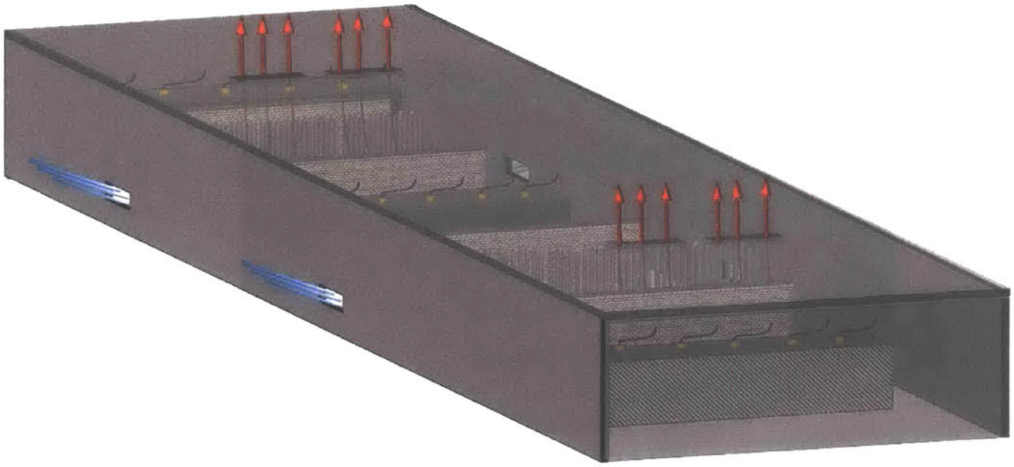

Figure 3-26. Open system harnessing buoyancy-driven flow for passive cooling during storage hours. Walls of the enclosure are assumed to be insulated, though not illustrated. Ceiling ports close during hours of discharge, and remain open during hours of charging or storage.

The design parameters for buoyancy-driven displacement ventilation include the area of port openings A_H, the discharge coefficient of the opening c_d describing energy loss associated with flow through the opening, and the vertical distance h between the lower and upper port. The displaced volume flux across each opening follows[147]

$$\dot{V} = \left(\frac{g(\rho_{ext}-\rho_{int})}{\rho_{int}}\frac{h}{2}\right)^{\frac{1}{2}} c_d A_H \tag{3-37}$$

where ρ_{ext} is the density of air outside the vessel, ρ_{int} is the average density of the air inside the vessel which is displaced, and g is the gravitational constant. We may then estimate the rate of heat transfer across the ports as $Q_{disp} = \rho_{int} c_p \dot{V}(T_{SS} - T_{ext})$ where c_p is the average specific heat of air displaced, T_{SS} is the steady state temperature of air between the membrane wall and insulating barrier, and T_{ext} is the external environment temperature (i.e. temperature of air outside the enclosure). The heat transferred by displacement ventilation represents a heat loss, however it also helps maintain the membrane wall below the maximum temperature without any external power input if other options such as residential water heating or preheating is not utilized.

For the following calculations, we assume a discharge coefficient c_d of 0.5 for a sudden opening which represents sharp expansion of flow upon discharge. For reference, a c_d of 1.0 represents a smoothly evolving flow through the opening, without energy loss[151]. The area of the port A_H is w^2 where w is the width of the port, a design parameter illustrated in Figure 3-27. To minimize the total dimensions of TERS, including the enclosure, a height h of 6 m is considered. The environment temperature T_{ext} is assumed to be 25°C.

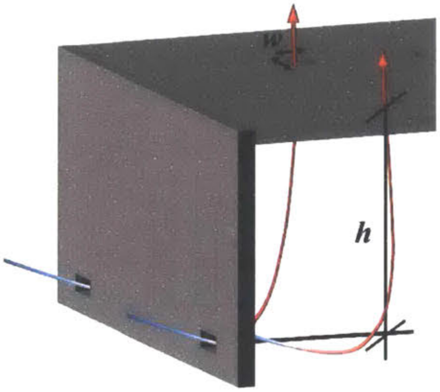

Figure 3-27. Parameters for buoyancy-driven displacement ventilation.

Heat transfer coefficient correlations for displacement ventilation in rooms is highly dependent on factors such as room size, enclosure geometry, presence of forced air movement, opening size, etc[152]. Nonetheless, the actual heat transfer coefficient is not expected to deviate much from general correlations developed for natural convection on a vertical surface in a displacement ventilated room. For the following calculations, we assume that the flow from the bottom to upper port is confined to the membrane wall. If the insulating barrier is relatively close to the membrane wall (relative to the height), such that we can no longer assume that the upper and lower port only have significant effect on the membrane wall, then we can expect some convective cooling of the insulating barrier as well. To estimate the average heat transfer coefficient ($\overline{h_c}$) by natural convection across the membrane wall, the following correlation is implemented[153]

$$\overline{h_c} = 1.823\,\Delta T^{0.293}/H^{0.121} \tag{3-38}$$

where $\Delta T = T_2 - T_\infty$, the average difference between the membrane wall surface temperature and air temperature. The above correlation is valid for vertical walls of an enclosure filled with air in which displacement ventilation occurs.

3.7.2. System of Equations

Initially, firebrick by itself was considered as the insulating barrier. However, firebrick does not present a high enough thermal resistance to maximize storage efficiency. Therefore, we consider a slab of firebrick facing the silicon unit in series with a slab of microporous insulation. The maximum temperature of the microporous insulation considered is 1000°C, hence the use of firebrick as the initial resistance to reduce the temperature microporous insulation would be subject to.

Similar to the method of Chapter 3.6, we can solve a set of coupled equations describing the heat transfer from the silicon unit to the environment as illustrated in Figure 3-28. By solving these coupled equations, the necessary thickness of the insulating barrier can be determined. To solve these however, requires $\overline{h_c}$ and ΔT to be known. The fluid temperature is expected to increase as heat is transferred to the fluid, and thus ΔT is expected to decrease, resulting in a temperature gradient across the membrane wall in the z-direction. To determine the upper limit of required insulating barrier thickness, we neglect multi-dimensional conduction and assume a uniform membrane wall temperature.

Now, the firebrick and microporous insulation thickness is constrained by the interface temperature being less than 1000°C, rather the temperature of the membrane wall. Because microporous insulation is so thermally insulating, with a thermal conductivity $k_{MS} \sim 0.044$ $Wm^{-1}K^{-1}$ at a mean temperature of 800°C, the membrane wall will be below 600°C given a microporous insulation thickness on the order of centimeters[154]. Initially, $\overline{h_c}$ is estimated as 3 $Wm^{-1}K^{-1}$ then later checked once the membrane wall temperature is known. By symmetry, the center plane of the membrane wall in the xz-plane is adiabatic. Therefore, any radiation incident upon the membrane wall must be transferred to the air surrounding the membrane wall by convection.

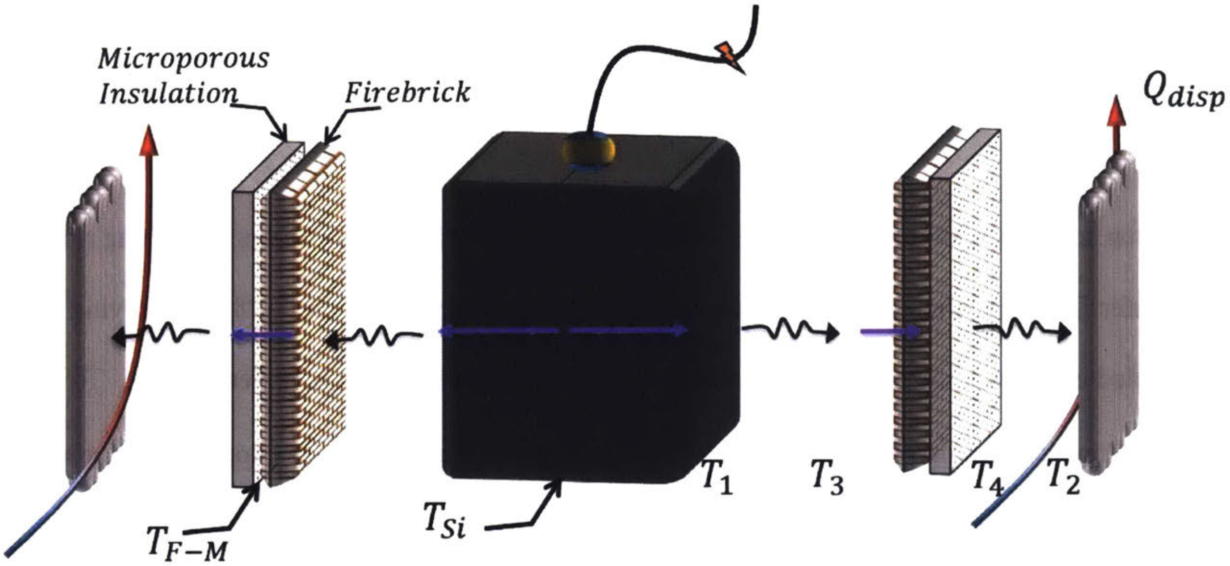

Figure 3-28. Path of heat transfer during hours of storage. T_{Si} is the temperature along the center of the silicon unit. $T_{F\text{-}M}$ is the interface temperature between microporous insulation and firebrick, assuming negligible contact resistance.

In the following calculations, we assume that the view factor between the silicon unit and insulating barrier is one, and that the view factor between the insulating barrier and membrane wall is also one. This is justified by all three bodies being close to isothermal and if the length of each body is much larger than the height, to be further discussed below. We also assume negligible contact resistance between the microporous insulation and Firebrick, which further gives us an upper bound on the required barrier thickness and thus upper bound on system cost. We do not expect that including a gap between the microporous insulation and firebrick will have a substantial effect on reducing heat transfer, considering the thermal conductivity of microporous insulation is already on the order of the thermal conductivity of air.

The following set of equations is solved for the temperature of the membrane wall (T_2 as before) given a firebrick thickness t_{FB} and microporous insulation thickness t_{ms}:

$$A\frac{T_{Si}-T_1}{\frac{l_{\mathrm{Si}}}{k_{\mathrm{Si}}}+\frac{l_{\mathrm{gr}}}{k_{\mathrm{gr}}}} - A\frac{\sigma(T_1^4-T_3^4)}{\frac{1}{\epsilon_1}+\frac{1}{\epsilon_3}-1} = 0 \tag{3-39}$$

$$A\frac{A\sigma(T_1^4-T_3^4)}{\frac{1}{\epsilon_1}+\frac{1}{\epsilon_3}-1} - \frac{(\mathrm{T}_3-T_4)}{\frac{t_{FB}}{k_{FB}}+\frac{t_{ms}}{k_{ms}}} = 0 \tag{3-40}$$

$$\frac{(\mathrm{T}_3-T_4)}{\frac{t_{FB}}{k_{FB}}+\frac{t_{ms}}{k_{ms}}} - A\frac{\sigma(T_4^4-T_2^4)}{\frac{1}{\epsilon_4}+\frac{1}{\epsilon_2}-1} = 0 \tag{3-41}$$

$$A\frac{\sigma(T_4^4-T_2^4)}{\frac{1}{\epsilon_4}+\frac{1}{\epsilon_2}-1} - \overline{h_c}A(T_2 - T_\infty) = 0 \tag{3-42}$$

Here, the unknowns are T_1, T_2, T_3, and T_4 (ref. Figure 3-28). The average fluid temperature T_∞ is varied from 27°C – 227°C, and depends on the performance of convection heat transfer between the air and membrane wall, and the performance of displacement ventilation. Future work may consist of experimentally testing the performance of displacement ventilation for cooling of the membrane wall. The thermal conductivity of insulating firebrick is denoted as k_{FB}, and A_c is the cross sectional area of firebrick normal to conduction in the y-direction. A specific insulating firebrick by BNZ Materials (IFB 2660) is chosen here due to its capability of thermal cycling. The firebrick has a thermal conductivity k_{FB} of around 0.27 – 0.33 $\mathrm{Wm^{-1}K^{-1}}$ for mean temperatures of

540°C-1100°C, and maximum temperature of 1427°C in an oxidizing atmosphere[155]. The emissivity of firebrick (ϵ_3) is around 0.9 and the emissivity of microporous insulation (ϵ_4) is 0.95. The area A of each body is another design parameter, to be further discussed below. For an example case, the length of each body is taken as 15 m, the height is 5 m, and $A = A_c$. After the first iteration of solving the above coupled equations, we find that the natural convection heat transfer coefficient is more so between 5 $Wm^{-2}K^{-1}$ and 6 $Wm^{-2}K^{-1}$ for the considered dimensions of the insulating barrier. A heat transfer coefficient of 5.5 $Wm^{-2}K^{-1}$ is used to produce the following figures.

The advantage of increasing the thickness of microporous insulation is that of reduced heat flux to the membrane wall, and therefore increased efficiency. However, the disadvantage is that microporous insulation is expensive, thus increasing system cost with increasing thickness. Another disadvantage is that of increased system size. The interface between firebrick and microporous insulation must be below 1000°C, which means the firebrick thickness must also increase with microporous insulation due to the difference in thermal conductivity. This can be seen in Figure 3-29, for T_∞ = 27°C. A microporous insulation thickness of 5 cm is used in the following calculations, chosen based on minimizing cost. The tradeoff between thickness and efficiency will be discussed in the following section. As a factor of safety, we limit the maximum interface temperature to 950°C.

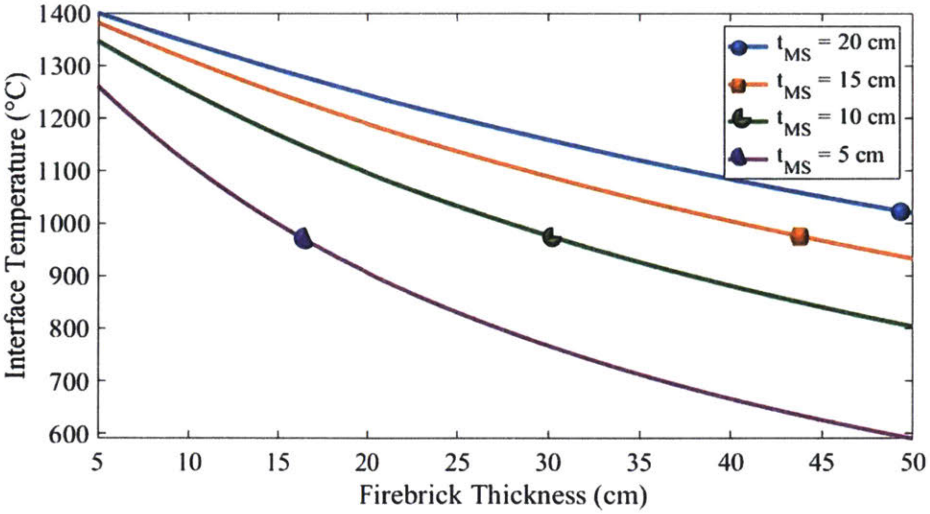

Figure 3-29. Effect of increasing resistance to conduction by microporous insulation on interface temperature with respect to firebrick thickness. The firebrick thickness must increase with increasing microporous insulation to ensure an interface temperature below 950°C. Calculations for $T_{\infty} = 27$°C.

To estimate the steady state temperature of air in the enclosure after the top ports have been opened, the rate of heat transfer from silicon to the membrane wall and surrounding air must be known. This depends on parameters such as the average fluid temperature T_{∞}, which itself effects the required thickness of firebrick. The effect of varying average fluid temperature on the membrane wall and interface temperature is shown in Figure 3-30, with respect to firebrick thickness. To calculate the steady state temperature of air in the enclosure, an average fluid temperature T_{∞} of 27°C is assumed in the following. Referring to Figure 3-30b, this fluid temperature corresponds to a firebrick thickness greater than 16 cm to satisfy the interface temperature requirement. A firebrick thickness of 22 cm for a microporous insulation thickness of 5 cm is used in the following calculation of steady state temperature.

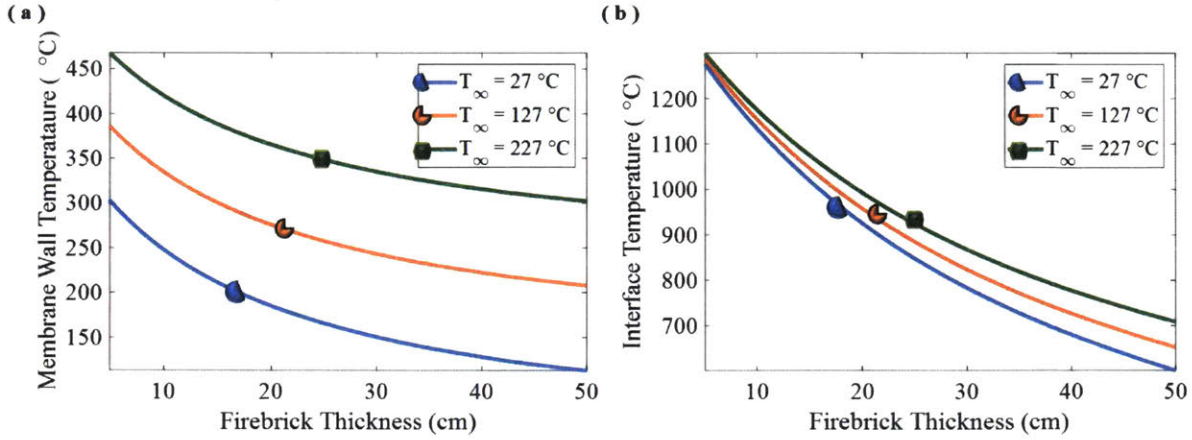

Figure 3-30. Effect of average fluid temperature on heat transfer. (a) Temperature of membrane wall versus thickness of firebrick insulation. (b) Interface temperature versus thickness of firebrick insulation. Temperature is determined given a thickness by solving the aforementioned coupled conservation statements. Points calculated considering a microporous insulation thickness of 5 cm.

The steady state temperature is reached once the lower front of cool air, which enters through the bottom port, ascends to the top upon displacing fluid of higher temperatures. Depending on the distance between the insulating barrier and membrane wall, the heat flux from the barrier will induce mixing of the air between the two bodies. This mixing leads to a more uniform distribution of the air temperature, which we will further assume to be uniform (Tss) and use it to estimate port size. An approximate steady state temperature can be solved for by equating the rate of heat transfer by convection across the membrane wall to the rate of heat transfer by displacement ventilation,

$$\overline{h_c}A(T_2 - T_\infty) = \rho_{int}c_p\dot{V}(T_{SS} - T_{ext}) \qquad (3\text{-}43)$$

Upon rearrangement, the final expression for steady state temperature between the firebrick and membrane wall is

$$T_{SS} = \frac{\overline{h_c}A}{\rho_{int} c_p c_d A_H} \left(\frac{g(\rho_{ext} - \rho_{int})}{\rho_{int}} \frac{h}{2} \right)^{-\frac{1}{2}} (T_2 - T_\infty) + T_{ext} \tag{3-44}$$

where ρ_{int} is evaluated at the mean temperature of T_4 and T_2. The larger the port, the larger the volumetric flux to the surrounding environment will be, and hence the smaller the resulting steady state temperature. If the port is too small, then the rate of heat transfer to the surrounding air will be larger than the mass flow rate leaving the enclosure, leading to higher internal temperatures. This trend can be seen in Figure 3-31. It is worth emphasizing that the performance of displacement ventilation is highly dependent upon the system in question, and the above calculation is but a rough estimate. To seriously consider natural convective cooling of the pipes, experimental evaluation must be performed.

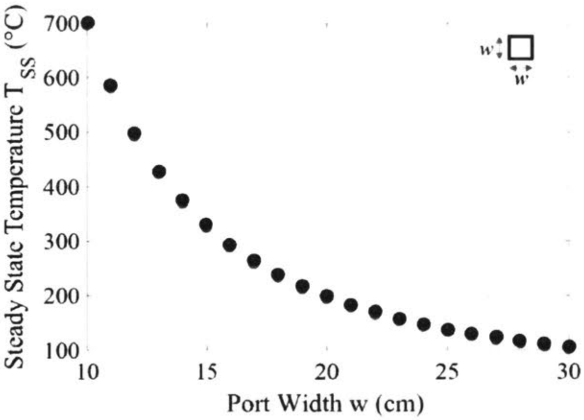

Figure 3-31. Steady state temperature of air between firebrick and membrane wall, with increasing port width. Calculations for T_{∞} = 27°C. Points calculated considering a microporous insulation thickness of 5 cm and firebrick thickness of 22 cm.

3.7.3. Feedwater Preheating

If we wish preheat feedwater during storage hours, thus reducing the amount of fuel necessary for consumption in the boiler, then the addition of Microsil insulation is unnecessary. Radiation from the firebrick to the membrane wall will heat the feedwater through forced convection. Given a mass flow rate, thickness of insulation, and pressure of the fluid, the final preheat temperature can be set by the duration in which the fluid is recycled through the system. For example, assuming the same mass flow rate as used in the discharge cycle (~0.38 kg/s) and thickness of firebrick, the temperature of the preheat fluid can be adjusted according to the duration of cycling. The same method as applied in Section 3.6.1 is applied here to solve for the rate of heat transfer, but including radiation to/from and conduction through the firebrick. We solve the coupled heat transfer equations to calculate the rate of radiative heat transfer from the firebrick to the membrane wall, and thus determine the temperature of the HTF as it cycles through the system during storage hours. The results in Figure 3-32 are for water at 24 MPa, though fluid of any pressure can flow through the system. Also of note is that any amount of feedwater may be diverted to our system; rather preheating the entire amount of water to be sent through the boiler, a fraction may be diverted. The same principle applies to heating water for industrial or residential purposes.

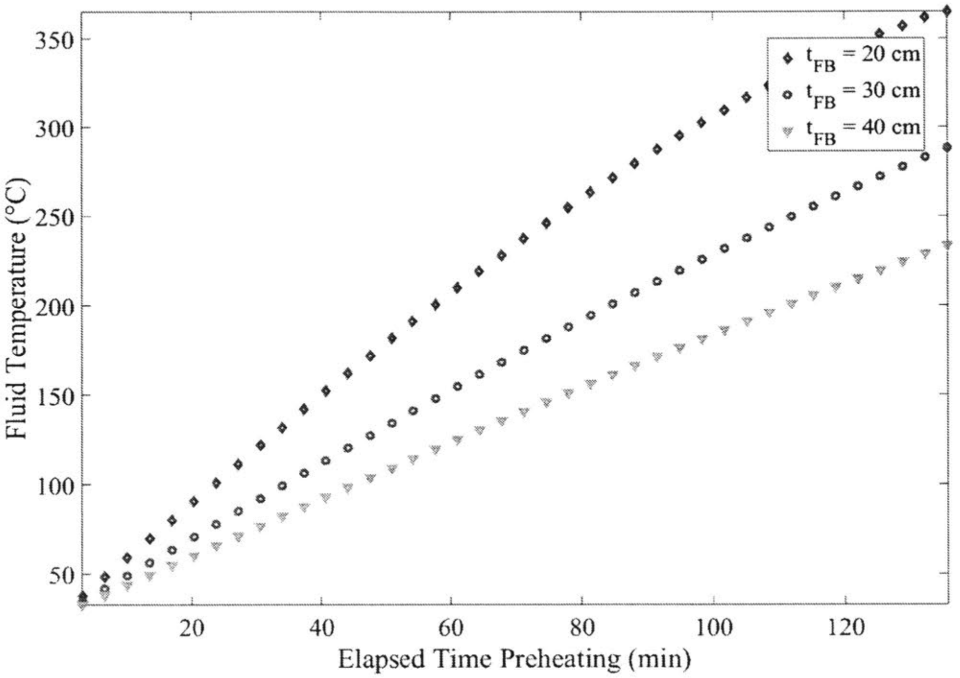

Figure 3-32 Example of customizable degree of feedwater preheating or hot water generation as a function of insulation barrier thickness and preheating duration. Water is at a pressure of 24 MPa and an initial temperature of 25°C. For a given mass flow rate, the elapse time preheating is simply determined by the number of cycles and length of convective heating per cycle.

3.8. System Efficiency and Dimensions

3.8.1. Storage Efficiency

The efficiency during storage, previously defined as $\eta = 1 - Q_{loss}/Q_{stored}$ can now be expressed in terms of the total energy lost between discharge cycles since resistive heating during charging is 100% efficient.

At the beginning of system operation, there will be some energy stored in the insulating barrier, given by $E_{IB} = \left(\rho c_p V\Delta T_m\right)_{FB} + \left(\rho c_p V\Delta T_m\right)_{MS}$ where the volume of firebrick V is $A_c{\cdot}t_{FB}$, that of microporous insulation (MS) is $A_c{\cdot}t_{MS}$, and ΔT_m is their respective temperature difference between mean temperature and initial ambient temperature. This energy will come from radiation emitted by the silicon, and thus an initial loss from the energy stored. However, as long as the insulating barrier remains within the enclosure during times of discharge, ΔT_m is not expected to significantly change between cycles and thus the energy stored in the firebrick is not lost.

Therefore, if we assume displacement ventilation is used, the only real system loss consistent between cycles is by heated air leaving the enclosure through ventilation:

$$\eta = 1 - \frac{Q_{loss}\mathrm{t}}{E_{st}} \qquad (3\text{-}45)$$

where t is the storage time, i.e. duration in which upper ports are open. For the operation of TERS following Figure 2-2, and a lower bound of power block efficiency 45%, the thermal energy stored according to Eqn. (2-1) is around $5.3\ x\ 10^9\ kJ$. The rate of heat transfer is the same as calculated in Section 3.7.2 through the system of equations. Given a duration of 12 hours in which the upper ports are open, the storage efficiency is calculated and plotted in Figure 3-33 with varying microporous insulation thickness to show the significance insulation plays on overall efficiency. The appropriate firebrick thickness necessary to meet interface temperature requirements can be determined from Figure 3-29.

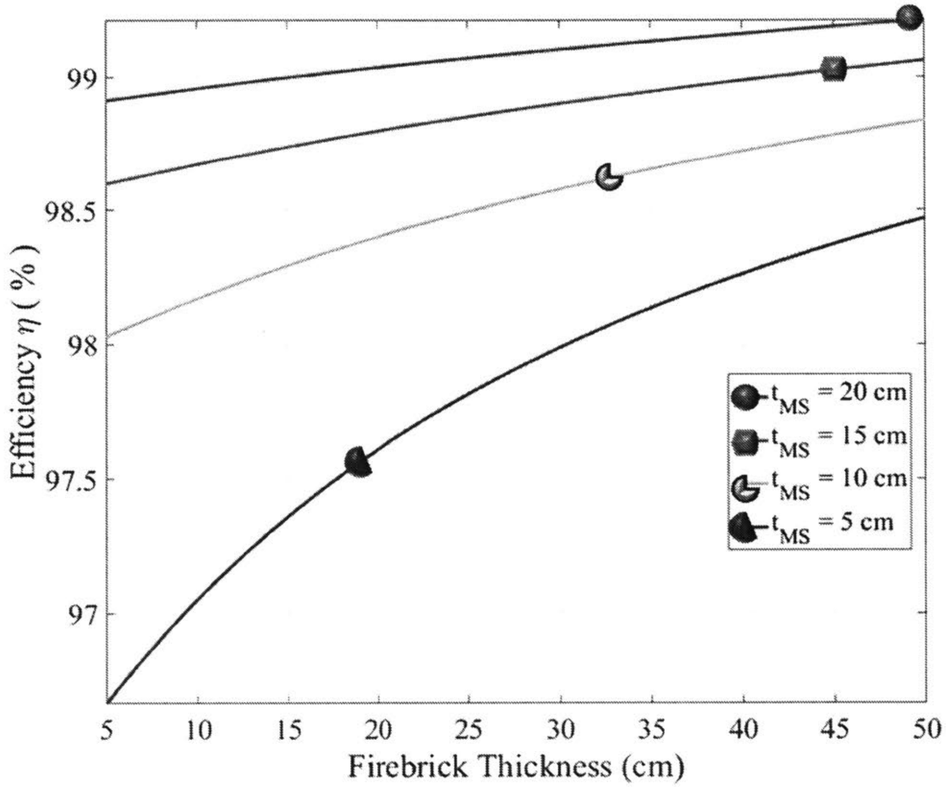

Figure 3-33. Thickness of insulation and storage efficiency with varying microporous insulation thickness. For low cost and ease of mobility, the thickness of the insulating barrier should be kept a minimum while maintaining high efficiency and adequate temperatures if the membrane wall. Calculations for T_∞ = 27°C though effect of temperature on efficiency is found to be negligible.

An even higher efficiency is achieved through preheating feedwater, as any heat leakage will be used for heating the water, hence leading to 100% storage efficiencies. This will also significantly reduce system cost as the insulating barrier only consists of firebrick.

3.8.2. Unit Sizing

The unit length L is a design parameter dependent on the strength of the container, and does not affect the rate of heat transfer so long as the view factor can still be approximated as 1. The total length of silicon required however is restricted by the storage capacity, thickness of silicon, and height. Thickness of silicon is restricted by the desired rate of heat transfer, as an increasing thickness (i.e. increasing resistance to conduction) results in a decreased rate of heat transfer.

The height H of 5 m considered here was chosen to ensure hydrostatic pressure of molten silicon against the graphite container would not be an issue. The resultant force due to hydrostatic pressure of molten silicon is $F_{yz} = 1/2(\rho_{Si} g H^2 2t_{si})$ in the yz-plane and $F_{xz} = 1/2(\rho_{Si} g H^2 L)$ for which we can determine the axial stress σ_{axial} in the walls to compare with isostatic graphite material properties. Using a length L of 15 m, for example, results in stresses much less than the strength of any typical isostatic graphite (i.e. tensile strength ~ 10^3 σ_{axial}).

To estimate system cost, dimensions of each component are assigned. For a height of 5 m, the total length of silicon necessary to satisfy storage capacity requirements according to Section 2.3 is ~ 555 m, or 37 silicon units of 15 m x 0.4 m x 5 m (length x width x height) dimensions excluding graphite. For 37 units, assigned 2 membrane walls per unit, there can be approximately

5 serpentine tubes per wall to satisfy a total of 320 tubes. For a membrane wall of 15 m, that leaves 3 m per tube of 40 m hydraulic length. Here, we define hydraulic length as the distance through which HTF flows between the inlet and outlet of the tube. The insulating barrier is designed to be the same length and height as the silicon unit (15 m x 5 m). In the following cost analysis, the firebrick thickness is 27 cm and the microporous insulation thickness is 5 cm, resulting in an interface temperature ~770°C and storage efficiency of 97%. A larger thickness of microporous insulation can be used, however the increase in cost should be considered. We compare different thicknesses of the insulation barrier with respect to cost and efficiency in Chapter 5. Aside from the silicon unit width and tube hydraulic length, the above dimensions are not meant to be limiting factors; they are solely given for the purpose of estimating system cost.

A sensitivity analysis is performed to determine limiting factors to achievable heat flux, and thus minimum system size. Results are provided in Figure 3-34. The thickness of silicon in the x-direction is chosen based on two primary factors: system length and heat flux. The thicker the silicon, the larger the resistance to conduction heat transfer, and thus the smaller the heat flux through the silicon. However, given a set volume of silicon based on desired storage capacity, a reduced thickness requires an increase in system length or increase in number of silicon units. The resistance to conduction through silicon is on the same order of that for conduction through graphite, as can be seen in Figure 3-34. The sensitivity to emittance is also plotted, however the choice of emitter is restricted to low-cost materials that can withstand high temperatures and bond well to the graphite container. Compared to other significant resistances, our system proves insensitive to forced convection.

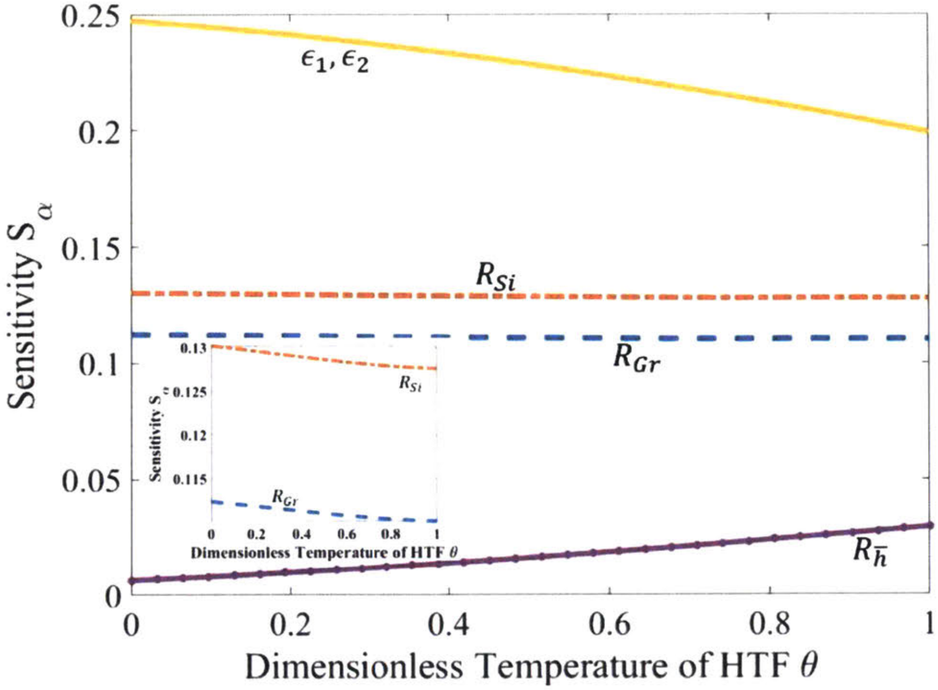

Figure 3-34. Sensitivity analysis of resulting rate of heat transfer to various parameters. Sensitivity parameters include emissivity of container and water wall (ϵ_1, ϵ_2), resistance to conduction through solid silicon R_{Si} defined as l_{Si}/k_{Si}, resistance to conduction through graphite R_{Gr} defined as l_{Gr}/k_{Gr}, and resistance to convection to the HTF defined as $1/\bar{h}$. Inset shows sensitivity variation of R_{Si} and R_{Gr}. The *x*-axis is once again the dimensionless temperature or equivalently, distance along *z*-direction of fluid heating. As θ approaches 1, the temperature difference between the silicon and waterwall decreases, which leads to variation in sensitivity to different resistances present in the system.

Chapter 4 Conduction based Thermal Energy Storage

4.1. Overview

It is useful to compare the above radiation based TERS to more common designs involving thermal energy storage. Such designs rely primarily on conduction and/or convection between the TES media and HTF, rather radiation, and have been extensively studied both theoretically and experimentally for low pressure applications. A large safety concern arises when considering a highly pressurized fluid flowing through a tube that is in contact with a molten metal such as $AlSi_{12}$. In the event that a HTF tube cracks, high pressure water in contact with the molten metal may result in an explosion. Thus, the radiative version of TERS described in Chapter 3 is more realistic to implement. The following analysis is performed to compare the cost of such a novel radiative TES system to the more common conduction based TES systems.

An example of a common TES system has been studied by Pirasaci and Goswami. Pirasaci and Goswami modeled a latent heat storage system for superheated vapor generation using the eutectic $NaCl-MgCl_2$. A schematic of the design is provided in Figure 4-1. This design is common for thermal storage systems using phase change materials. Although supercritical pressures have not been considered, Pirasaci and Goswami did indeed consider superheated vapor at 165 bar[156].

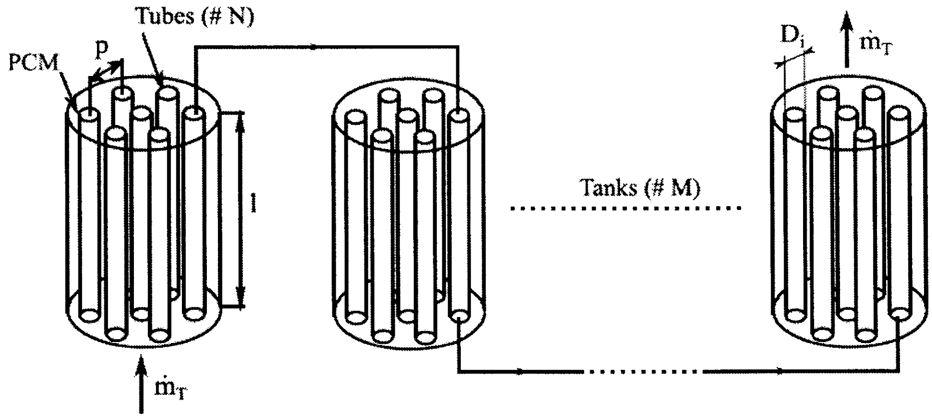

Figure 4-1. Schematic of latent heat thermal energy storage system commonly adopted in literature. Figure reprinted from Pirasaci and Goswami[156].

Similarly, Kotze et al. has studied a TES system using the eutectic $AlSi_{12}$ as a phase change material, with liquid metal heat transfer pipes used to charge the system, and water heat transfer pipes utilized during discharge. An illustration is provided in Figure 4-2. His system was designed for water pressures of 150 bar. Kotze et al. further tested their concept experimentally under discharge conditions, validating discharge operation using oil as the HTF rather water, and finding good agreement between their heat transfer model of the moving boundary problem and experimental results[132,157–159].

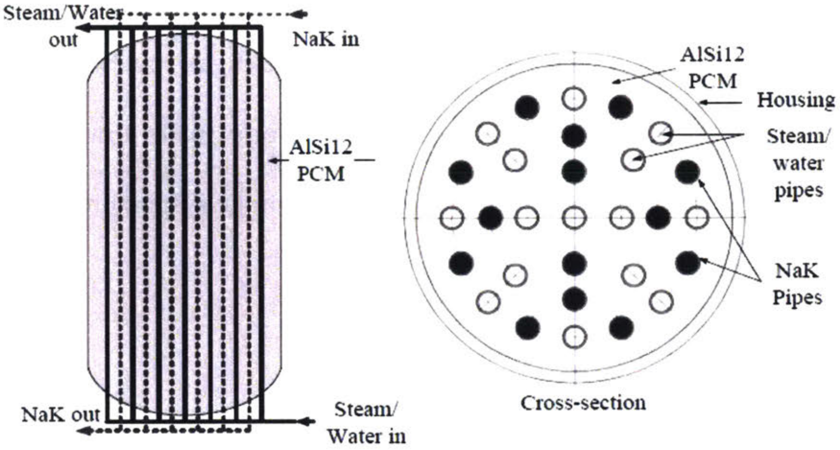

Figure 4-2. Design of thermal energy storage system utilizing liquid metal to charge the PCM, and producing superheated water vapor upon discharge. Figure reprinted from Kotze et al[132].

The vast majority of thermal energy storage previously or currently in practice are utilized with solar thermal power plants. Due to most phase change materials having a low thermal conductivity or corrosive nature, sensible heat media have been primarily used.

Specifically, two tank sensible TES systems are commonly adopted in liquid sensible systems, using molten salts as the storage medium. In some cases, the molten salt is also the HTF (also known as direct storage system). For example, at the Solar Two plant previously in the Mojave Desert in California, a molten salt composed of sodium nitrate and potassium nitrate was used, which has a melting temperature of 207°C and maximum stable temperature of 600°C. To maintain these temperatures during times at which solar radiation was not adequate, multiple 25kWe immersion heaters were used to heat the salt[160].

Using solid sensible media only requires a single tank. Typically, a heat exchanger for the HTF is embedded within the solid. Due to its low cost and high strength, much work has been done on using concrete as the sensible storage media, with efforts made towards high-temperature concretes and castable ceramics. A photo of the concrete storage system previously tested by DLR is provided in Figure 4-3.[161]

Figure 4-3. Photo of HTF tubes imbedded in concrete storage system at DLR[161]

4.2. Design

The different configurations of TERS suitable for TES mediums operating around 600°C are illustrated in Figure 4-4. For solid thermal energy storage media, such as concrete or firebricks, a configuration such as in Figure 4-4a can be adopted, where the HTF flows through the embedded heat transfer tubes upon discharge to produce supercritical water. Resistance heaters can be imbedded within the storage media for charging. The same configuration may be used for phase change materials in which the phase change temperature is not high enough to effectively radiate to the HTF, as in Chapter 3. To determine which medium would be suitable for electrically charging and producing supercritical water upon discharge, we compare thermal and economic characteristics of suitable materials including, but not limited to: silica fire bricks (SFB)[100], magnesia fire bricks (MFB)[100], carbonate salts (CS)[100], and the eutectic $Al_{0.88}Si_{0.12}$[102,157]. Solid sensible (SFB , MFB) and the eutectic phase change material are separately considered in the design of Figure 4-4a to estimate system cost.

In considering liquid sensible storage media, a configuration such as in Figure 4-4b can be adopted and is commonly known as indirect storage. Upon discharge, the liquid storage media is pumped from the hot tank to the cold tank, transferring heat to a HTF via an intermediate heat exchanger. Carbonate salts is considered here for evaluation of a liquid sensible media, having a relatively low material cost and high maximum temperature.

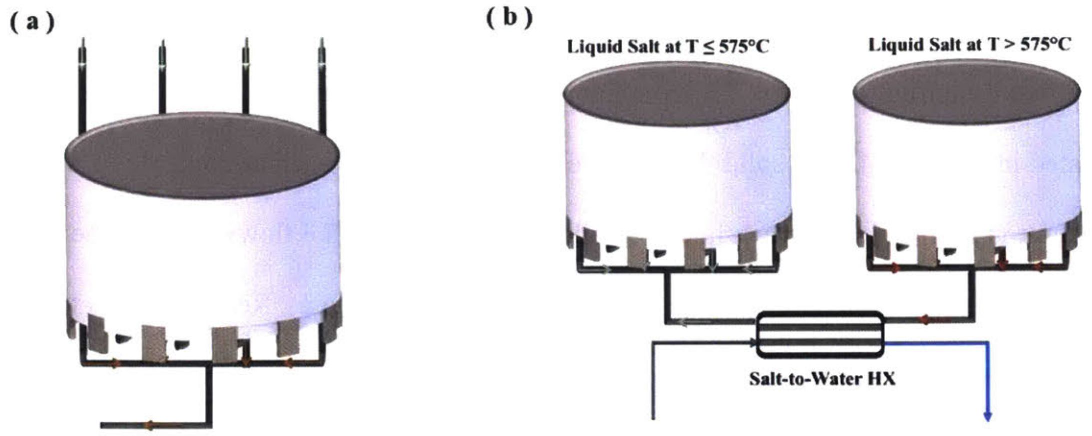

Figure 4-4. Heat Transfer Configurations for TERS Unit. (a.) A stationary design may be used for solid sensible storage materials and phase change materials. The heat transfer fluid is also the working fluid, i.e. water, which is heated to supercritical temperatures by flowing through tubes imbedded within the TES material. To reheat the TES material, electricity is sent through resistive heaters that are also embedded within. (b.) Liquid salts have better heat transfer characteristics by taking advantage of liquid-to-liquid heat exchanger, as shown. Here, water is again the working fluid and utilizes a counterflow heat exchanger to transfer thermal energy from the liquid salt to the water. Charging of the system occurs by resistive heaters within the tank containing liquid salt at temperatures at or below 570°C. Note, the direction of flow will reverse upon cycling. Blue arrows indicate heat transfer fluid (water), i.e. water in this case, temperatures below 570°C while orange arrows indicate fluid temperatures above 570°C.

The configurations of Figure 4-4 are not novel as discussed above[157,158,160,162]; the novel aspect that has yet to be evaluated in the literature is producing supercritical fluids without intermediate heat exchangers in the below configurations. Thermal energy, rather electrical, is normally used to charge such systems. If storing heat, rather electricity, was the desired operation then high temperature water could simply flow through the same tubes that water flows upon discharge.

The detailed configuration of Figure 4-4a is illustrated in Figure 4-5 for further clarity. The HTF tubes are immersed within the phase change media or solid sensible media, with electrical immersion heaters embedded in the storage media as shown. Upon discharge, HTF flows through the tubes and is heated to supercritical temperatures. Note that it is not necessary that the HTF be at high pressures. Supercritical conditions are considered here to maximize power plant efficiency.

A similar configuration is displayed in Figure 4-6, where operation is the same as described for Figure 4-5. However, by having a single tube with the appropriate thickness of storage media individually contained, a more flexible arrangement of the units (each unit having one HTF tube and contained PCM) can be achieved for existing power plants that are limited in footprint. There is a tradeoff between flexibility and system cost, as cost does increase as a larger amount of tank material is required compared to the first configuration. The heat transfer of both designs will be nearly identical, in which the heat propagates radially, greatly simplifying the analysis by axial symmetry.

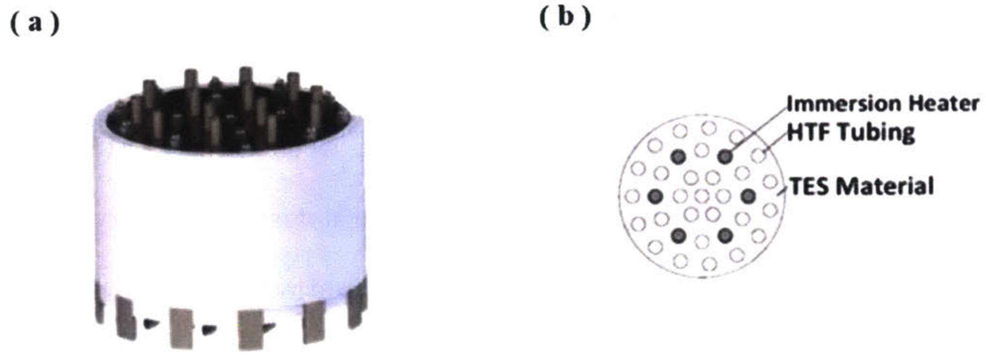

Figure 4-5. Illustration of conduction based TERS unit for solid sensible TES media or phase change materials. (a) TERS assembly minimizing cost and heat leakage, components enclosed within a single container. Projections of dimensions are not to scale. (b) Top view of assembly. The TES media surrounds the tube through which water/supercritical fluid flows, resulting in a shell-and-tube like configuration.

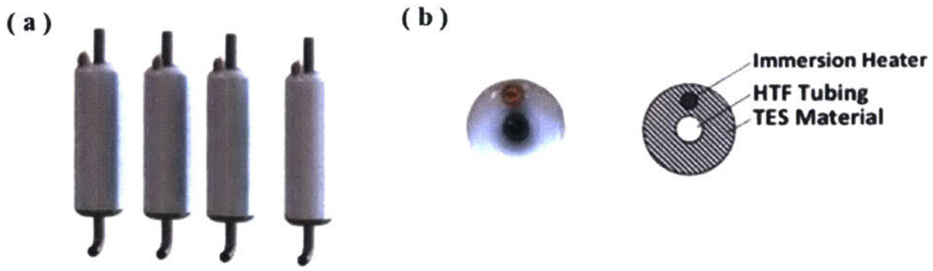

Figure 4-6. Illustration of conduction based TERS assembly for solid sensible or phase change storage media, designed for ease of retrofitting into existing sites. (a) Illustration of assembly consisting of multiple units, each of which have a HTF pipe and electric heater (b) Corresponding top view of TERS tubes and schematic diagram revealing inner working is provided—TES medium surrounds pipe in which heat transfer fluid flows (e.g. water to supercritical water) with immersion cartridge heater immersed in the TES medium.

4.3. Heat Transfer Characteristics

To determine the number of tubes required for TERS following Figure 4-5, and thus total material cost for the water tubes, the rate of heat transfer from the TES media to the water is determined with respect to system size. Unlike silicon where system size was limited by conduction only and not energy density, here volumetric energy density and therefore system size is also of concern. The size of the heat transfer domain considered for each medium is denoted as r_x in Figure 4-7. In estimating the rate of heat transfer, we make several of the same simplifying assumptions as applied in Chapter 3.6:

(i) Steady-state conditions, all of phase change material is in solid state

(ii) Material properties are temperature independent

(iii) Local convection heat transfer coefficient between the tube and water is uniform on inner surface and an average value for the coefficient along the tube is taken

(iv) Negligible contact resistance between tubes and storage media if stationary design considered

(v) Temperature of HTF varies incrementally along the length of the tube from 100°C to 570°C

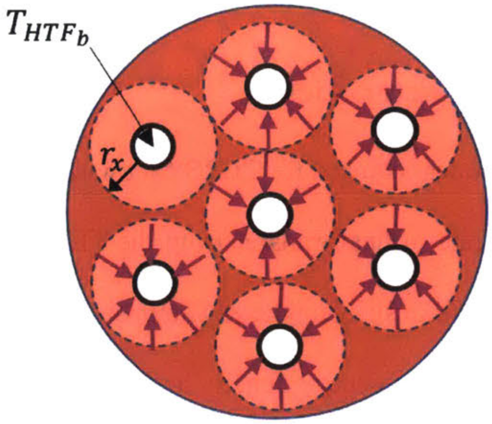

Figure 4-7. Illustration of heat transfer domain considered in conduction based TERS. For $AlSi_{12}$, conduction is only considered in the solid region which extends in the radial direction with time during phase change.

The rate of heat transfer $\dot{Q}$ from the solid thermal storage media to the HTF is simply $\dot{Q} = (T_{r_x} - T_{HTF_b})/R_{Total_i}$ in which R_{Total_i} is the total thermal resistance across the TES media to the water. This can be determined by a simple thermal resistance circuit as follows,

$$R_{Total_i} = \frac{1}{\bar{h}A_i} + \frac{\ln\left(\frac{r_o}{r_i}\right)}{2\pi k_t L} + \frac{\ln\left(\frac{r_x}{r_o}\right)}{2\pi k_{TES} L} \tag{4-1}$$

Here, A_i is the inner surface area of the tube ($2\pi r_i L$), L is the length of the tube, k_{TES} is the thermal conductivity of the chosen TES material, i.e. $AlSi_{0.12}$, SFB or MFB, and all other variables are as defined in Chapter 3.

As considered in Chapter 3, natural convective effects within the phase change material are neglected, resulting in a conservative estimate for the overall heat transfer coefficient. In general, the thermodynamics of energy storage during phase transitions from solid to liquid have been studied and the importance of convection versus conduction in the process has been discussed[127–129]. In the case of $AlSi_{0.12}$ and Si, this assumption is valid considering the high value of thermal conductivity they possess and consequently low Rayleigh number[130–133].

Because silicon has a much higher energy density compared to $AlSi_{0.12}$, SFB or MFB, a larger volume of material is required to satisfy the same storage capacity. The design radius r_x is increased up until too large of a thermal resistance exists, resulting in a low heat flux and hence low mass flux through the tube. This constraint on the radius results in more tubes required to satisfy storage capacity than required to meet power demand i.e. not all tubes will have HTF flowing through them simultaneously.

When calculating the rate of heat transfer through $AlSi_{0.12}$, the media is assumed to have already been discharged of latent heat (i.e. all in solid phase), thus giving us a lower limit of heat flux as previously performed for silicon. The lower limit of heat flux to the HTF is on average 430 kWm^{-2} considering $AlSi_{0.12}$ as the medium. For a tube length of 20 m and average mass flux of 230 kg $m^{-2}s^{-1}$, the resulting number of tubes is on the order of 10^3.

Both SFB and MFB prove to be unrealistic candidates, due to their low thermal conductivity. Having the lowest thermal conductivity, SFB is unable to provide an acceptable rate of heat transfer. As for MFB, an unreasonably small value of r_x is required to obtain high heat flux and adequate mass flux, resulting in a prohibitively large number of tubes required. For a tube length of 20 m and average mass flux of 230 kg $m^{-2}s^{-1}$, the resulting number of tubes using MFB as the storage media is on the order of 10^5.

From a heat transfer performance perspective, the eutectic alloy $AlSi_{0.12}$ may appear attractive. However, from a safety perspective, such a design is unfavorable and may not be implemented in practical settings.

Chapter 5 Cost Analysis

There are few sensible energy storage mediums that can withstand the high temperatures at which supercritical power plants operate (e.g. Cast steel, silica fire bricks, magnesia fire bricks, nitrate salts, carbonate salts), and even fewer that aren't economically devastating[79,163–165]. As for phase change materials, low thermal conductivity is a key road block. However, alloys of Al_xSi_{1-x} or even pure Si have high thermal conductivities giving rise to reasonable discharge times. For the conduction based model of TERS where the HTF tube is in direct contact with the thermal storage media, we define an upper temperature limit of 700°C to minimize the approach temperature and to avoid complicating the system with construction materials which must withstand higher temperatures. The lower temperature limit of $AlSi_{0.12}$ is 580°C according to the desired outlet HTF temperature. Since carbonate salts are ideal in molten form, the TES medium need not be in stationary form, and a counterflow heat exchanger may be used, allowing minimum temperatures such as < 200°C.

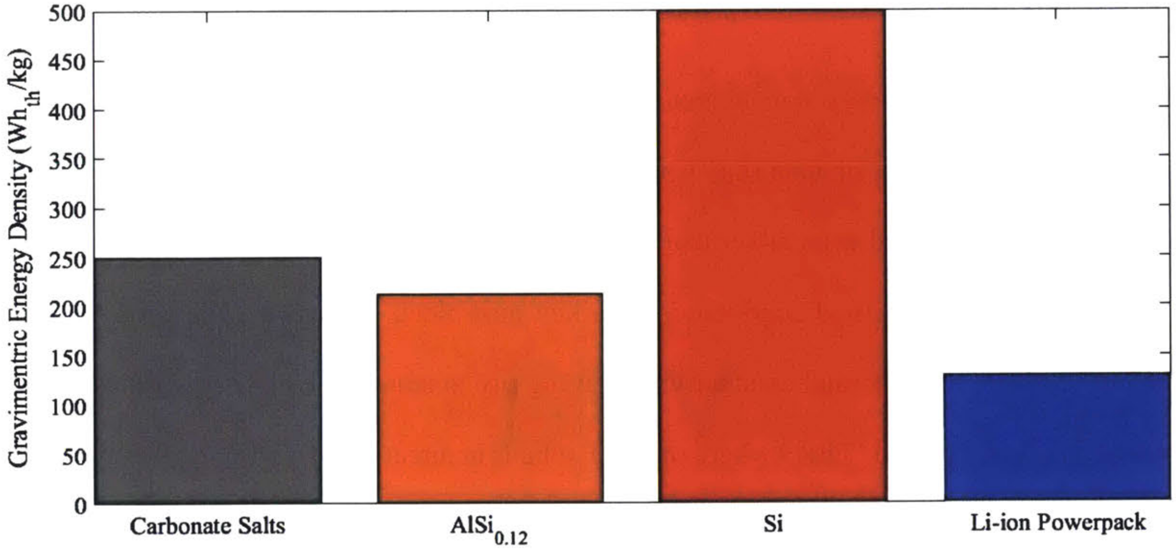

Figure 5-1. Comparison of gravimetric energy density between energy storage media. (23a.) In considering carbonate salts and $AlSi_{0.12}$, gravimetric energy density is defined as $[h_{fg} + c_p(T_h - T_{min}\ )]/3.6\frac{kJ}{Wh}$ where T_h is the maximum system operating limit of 700°C, defined by tank and piping material properties. For $AlSi_{0.12}$, T_{min} is 580°C and that of carbonate salts is 200°C. For Si, heat capacity was not considered in the analysis; the energy density was defined as $h_{fg}/3.6\frac{kJ}{Wh}$. The Li-ion Powerpack is a product by Tesla marketed for utility and business storage use. The energy density was calculated by taking the quotient of storage capacity (210 kWh) by Powerpack weight (1622 kg) excluding the inverter[40].

The total cost of TERS utilizing $AlSi_{0.12}$ consists of the following: container cost (composed of carbon steel with a 10 mm inner lining of alumina), cost of immersion heaters, raw material cost of $AlSi_{0.12}$, cost of HTF tubes composed of P92 steel, container insulation using AES wool, and a factor accounting for installation, instrumentation, etc. considered to be 18% of the total raw material cost. All material costs are specified in Table 8 at the end of this chapter.

Utilizing carbonate salts as the storage media introduces a cost for heat exchangers and salt pumps. This is included in total cost, along with a carbonate steel storage tank, immersion heaters and the 18% cost factor.

The total cost of TERS designed to harness radiative heat transfer will roughly consist of the cost for water tubing, composed of P92 steel as typical supercritical boilers implement, immersion heaters, silicon, raw material for the silicon container such as graphite, mobile insulation such as firebrick and an 18% cost factor. This includes 10% for balance of system including additional piping to existing infrastructure, valves, instruments, control wiring, etc[166]. An additional 2% cost factor to the capital investment is included for utilities, 4% for maintenance, and 2% for miscellaneous factors[167]. With increasing thickness of the insulating barrier, total cost will increase. By estimating the heat transfer performance of TERS according to the design parameters, an approximate cost of such a system can be determined resulting in a cost of ~10$/kWh$_e$ for a firebrick thickness of 27 cm and microporous insulation thickness of 5 cm. Total cost breakdown is depicted in Figure 5-2. Without microporous insulation, a firebrick thickness between 15 cm and 50 cm results in a total cost of ~7.8 $/kWh$_e$ to ~14.6 $/kWh$_e$.

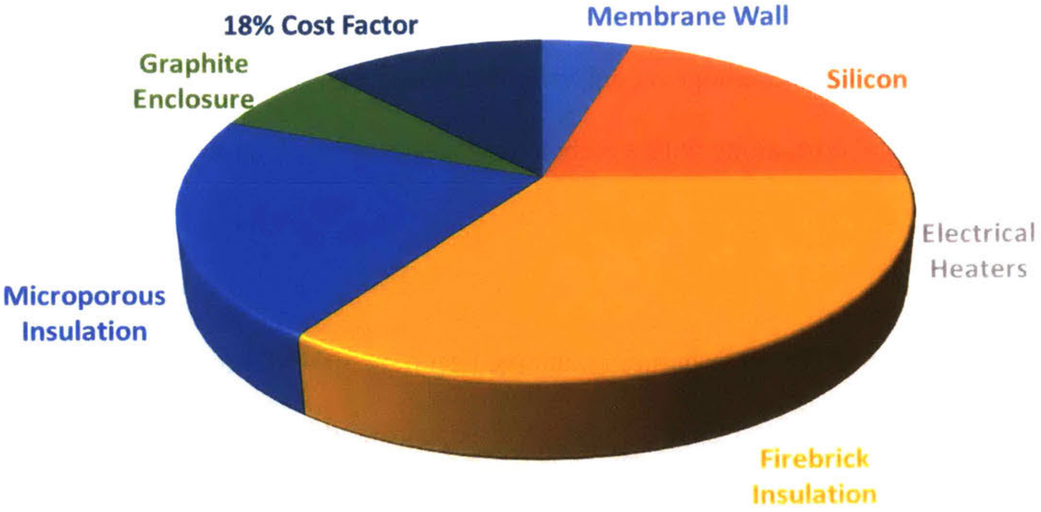

Figure 5-2. Cost breakdown of radiation based TERS having a storage efficiency of 97%. Total cost is roughly 10 USD/kWh$_e$.

As mentioned previously, there is a tradeoff between the cost and efficiency of the radiative based design for TERS if feedwater preheating is not utilized. A list of costs associated with increasing efficiency is provided in Table 7, including details of the corresponding insulating barrier. The 18% cost factor is not included in the total raw material cost, however all other components are indeed included.

Table 7. Radiative TERS Cost vs. Efficiency (feedwater preheating not considered)

t_{MS} (cm)	t_{FB} (cm)	Interface Temp.	Cost of FB (USD/kWhe)	Cost of Microporous Insulation (USD/kWhe)	**Total Raw Material Cost (USD/kWhe)**	**Storage Efficiency**
5	27	770°C	4.48	2.72	**8.58**	**97%**
10	40	850°C	6.63	5.44	**10.74**	**98%**
18	50	950°C	8.29	9.80	**12.40**	**98.7%**

One of the main hindrances to energy storage technologies being adopted is cost. Hence, the economics of TERS is compared to other common energy storage technologies in Figure 5-3. A firebrick thickness of 20 cm and feedwater preheating is considered in the technology comparison.

It can be seen that although the discussed design is in need of further development prior to implementation, such a system is indeed realistic and has the potential to mitigate and assist in healing the environment, while even potentially enhancing state of the economy per country. For all system efficiencies considered, the cost of radiative based TERS remains highly competitive with common storage methods such as PHS, CAES, and lithium-ion battery packs.

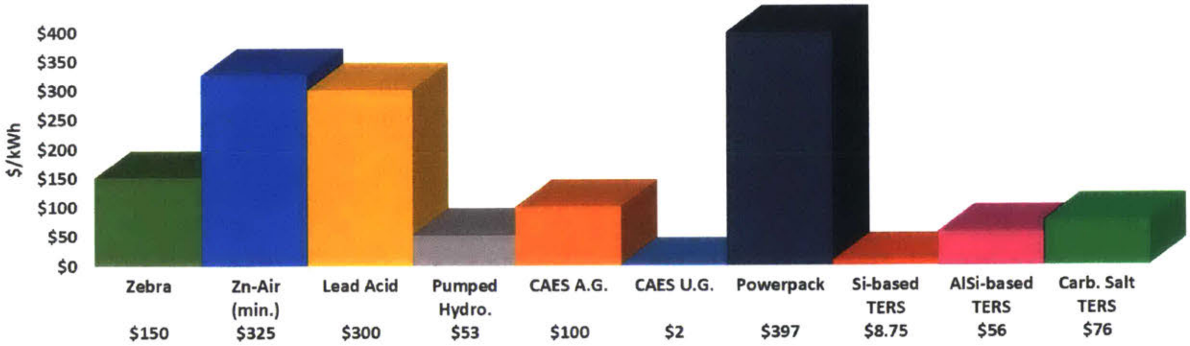

Figure 5-3. Cost comparison between estimated TERS versus a variety of energy storage systems. Rounded costs provided in table. The cost of Si-based, AlSi-based ($AlSi_{0.12}$ specifically) and Carbonate Salt-based TERS is determined by the methods described above. Technologies compared include compressed air energy storage (CAES)[39,41,62] underground U.G. (minimum cost) and above ground A.G. (maximum cost), pumped hydroelectric storage (PHS)[47,51,62], ZEBRA battery[38,47–49], Zinc Air battery (ZnAir) [39,75], lead acid battery[38,47,51,62], and Tesla Powerpack[40].

Table 8. Material and Technology Cost

Si[168]	2.97 USD/kg
Silica Firebrick[34,162]	1 USD/kg
Magnesia Firebrick [162]	2 USD/kg
Carbonate Salts[162]	2.4 USD/kg
Graphite[168]	0.37 USD/kg
Cartridge heater [169]	0.02 USD/watt
Alumina[170]	0.32 USD/kg
Carbon Steel[171]	0.465 USD/kg
P92 Steel[172]	1.25 USD/kg
Insulating Firebrick[155]	2.26 USD/kg
Microporous insulation[154]	21 USD/kg
Heat Exchanger for Carbonate Salt[166]	18 USD/kWh
Salt Pump for Carbonate Salt[166]	4.60 USD/kWh
ZEBRA Battery Min. – Max. Cost[38,47–49]	100-200 USD/kWh
Lead Acid Battery Min-Max cost[38,47,51,62]	200-400 USD/kWh
ZnAir Battery[39,75]	325 USD/kWh
PHS Min.-Max Cost[47,51,62]	5-100 USD/kWh
CAES Underground-Aboveground[39,41,51,62]	2-100 USD/kWh
Carbonate Salt TERS	~84 USD/kWh
$AlSi_{0.12}$ TERS	~55 USD/kWh

Chapter 6 Summary and Future Work

We present a novel method to heat supercritical fluid through radiative heating by a thermal energy storage unit. The type of water and desired end temperature is not meant to be a limiting factor; supercritical water is simply the example condition chosen for evaluation in this thesis. This radiative design is similar to heat transfer within a boiler, however combustion is not a requisite, thus avoiding emissions entirely during the electricity generation process.

Rather charging the system through solid-liquid or liquid-liquid heat exchangers, as is typically done, TERS will be charged via resistance heaters or other methods of electrical charging. This allows direct energy transfer from the power plant to TERS without an intermediate thermal process, such as having an additional fluid to transfer the heat as has been evaluated in the literature [132,157,158]. During times at which there is an excess of electricity production, typically at night time, the electricity can be sent to the TERS system rather being dumped or sold at reduced cost. Furthermore, having the option to charge TERS by means of combustion, thereby allowing continuous operation of the power plant, will reduce thermal stress in boilers that normally must "ramp" up and down to follow demand. With reduced stress follows an increase in boiler efficiency, thus reducing the amount of CO_2 emissions to some degree. Most notably, through charging with electrical heaters, TERS can solve the issue of renewable energy intermittency and have an irrevocably substantial impact towards the combat in climate change

Using high thermal conductivity and low cost phase change materials gives rise to the potential for dispatchable electricity using this system. Resistive heaters were discussed and considered in the cost estimates, however, additional forms of electrical heating are possible. Inductive heating may be used to charge TERS, thereby eliminating material compatibility concerns between the phase change material and heater. Additionally, for TES mediums that have high electrical resistance, it is possible to design the system such that it is charged by directly passing electricity through the medium, i.e. without an intermediate resistive heater. As the industry of silicon smelter is highly developed, in which electricity is used in an electric arc furnace, there is much promise that electrical heating of silicon is feasible.

Due to the safety issue of having a high pressure fluid in contact with a molten metal, e.g. as in the conduction based design of TERS, such thermal storage systems are most suitable for low pressure applications. For example, Rankine cycles that operate at lower pressures as in solar thermal power plants would gain benefit from the design. For high pressure cycles, the radiation based design is attractive since it does not require intimate contact between the heat transfer tubes and phase change material. Future work will investigate the radiative based thermal energy storage system as it proves most attractive for modern power plants operating at increased efficiency.

It is important to note that the above evaluation is more so a proof of concept, and there is much to be done in terms optimizing material compatibility. There remains the unavoidable trade-off between materials that can withstand supercritical temperatures and cost, hence the lack ultra-supercritical power plants in operation at the moment. However, that is not to say that it is impossible to have high temperature, cost efficient systems. To reach demonstration stage of TERS, much research must be done focusing on following key areas of concern:

- Foremost is material compatibility with molten silicon. At its phase change temperature, molten silicon is reactive and few materials are able to withstand the high temperatures. Using graphite as a container will result in a layer of silicon carbide at the interface of silicon and graphite. Eventually, this layer will continuously grow inwards, reducing the capacity of the system. In silicon smelter plants, refractory bricks with carbon linings are used, and silicon carbide is mechanically removed upon build-up.
- Volumetric expansion. Silicon is unique in that it expands upon solidifying. This must be taken into consideration when designing the container to ensure there is no detrimental damage on the container upon solidification and melting cycles of silicon. Furthermore, the container must be designed to withstand stresses imposed by molten silicon due to hydrostatic pressure.
- Heating method. Our current cost model included the cost of immersion heaters, which have been developed since the 1920's. However, the reliability of such heaters in molten materials is not proven. The same heating method used in electric arc furnaces may be used, though this may prove detrimental to cost as electrodes are consumed in the process of silicon smelter. There is also possibility to pass current directly through the molten material. Clearly, much research needs to be done.
- Oxidation. Graphite oxidizes in air at high temperatures. However, this can be avoided by coating the outer layer of graphite with silica or silicon carbide. Silicon also oxidizes in air. By containing the silicon in graphite, without any faces exposed to air, oxidation can be limited. However by having a closed container, volumetric expansion of silicon may cause problems with container durability.

- System design. Our conceptual design so far was aimed at providing a basis for cost estimation. Real systems can significantly depart from our conceptual design, depending on limitations we outlined above.

Appendix

The dependence of this temperature gradient on fin geometry is illustrated in Figure A-1 for the case of a known heat transfer coefficient as approximated in Section 3.4.2. Material properties used in the following calculations are the same as those provided in Chapter 3. By plotting the dimensionless temperature of the fin along the length of the fin, defined in Eqn. (A-1) it is clear that increasing mL results in a larger temperature gradient along the fin, which thus contradicts our approximation of an isothermal fin if the fin geometric parameters are such that mL is large.

$$\theta_f = \frac{T_2 - T_{fin}(y)}{T_2 - T_b} = \frac{\cosh\left(m\left(L_{fin} - y\right)\right)}{\cosh\left(mL_{fin}\right)} \tag{A-1}$$

The above equation is derived by a control volume analysis on the fin, resulting in the effective heat transfer coefficient provided previously in Chapter 3.6.

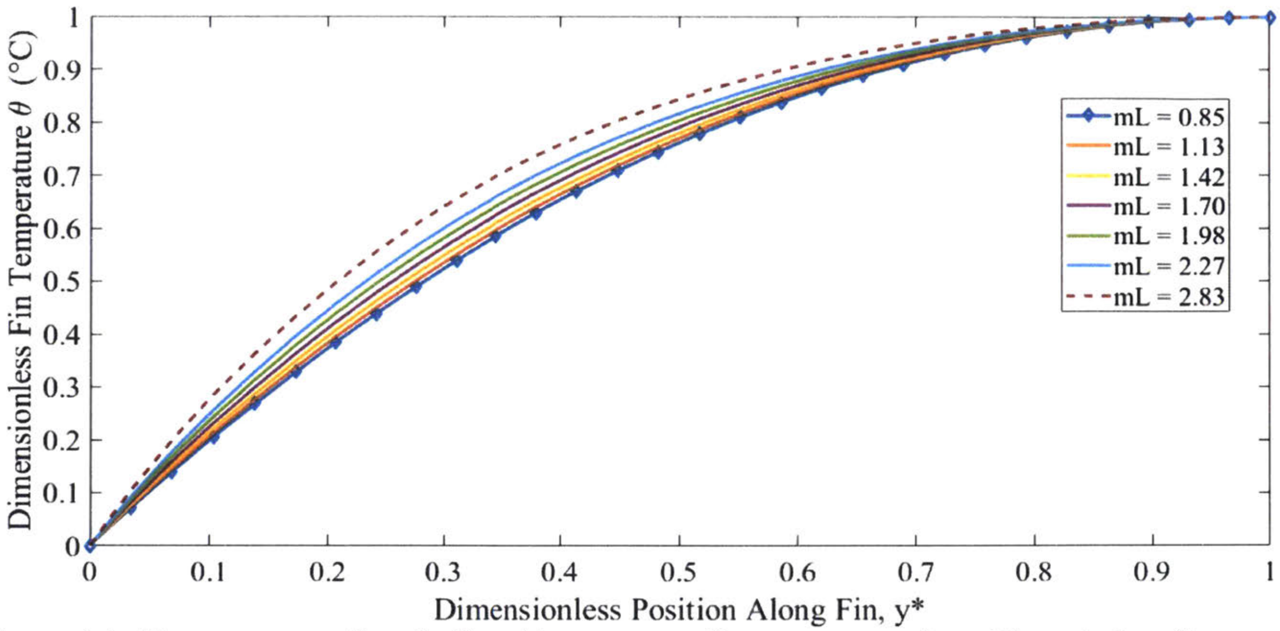

Figure A-1. Temperature gradient in fin with respect to fin parameter, mL_{fin}. Dimensionless fin temperature θ is defined as $\theta = (T(y) - T_b)/(T(L) - T_b)$, and dimensionless position is defined as y*=y/L where L is fin length. Fin thickness is 2 cm, base temperature is assumed to be 600°C, and T_2 is assumed to be 1300°C.

Bibliography

1. Lin, J. Energy storage—a cheaper and cleaner alternative to natural gas-fired peaker plants. *Prep. Calif. Energy Storage Alliance* (2011).
2. NYISO. *Hourly Loads 2017.* (2017).
3. Das, T., Krishnan, V. & McCalley, J. D. Assessing the benefits and economics of bulk energy storage technologies in the power grid. *Appl. Energy* **139,** 104–118 (2015).
4. Keatley, P., Shibli, A. & Hewitt, N. J. Estimating power plant start costs in cyclic operation. *Appl. Energy* **111,** 550–557 (2013).
5. Troy, N., Denny, E. & O'Malley, M. The relationship between base-load generation, start-up costs and generation cycling. in *Paper presented at the 28th USAEE/IAEE North American Conference 'Unveiling the Future of Energy Frontiers', New Orleans, December 3-5 2008* (International Association for Energy Economics, 2008).
6. Van den Bergh, K. & Delarue, E. Cycling of conventional power plants: technical limits and actual costs. *Energy Convers. Manag.* **97,** 70–77 (2015).
7. Linnenberg, S. & Kather, A. Evaluation of an integrated post-combustion CO2 capture process for varying loads in a coal-fired power plant using monoethanolamine. in *4th international conference on clean coal technologies* 18–21 (2009).
8. Kehlhofer, R., Hannemann, F., Rukes, B. & Stirnimann, F. *Combined-cycle gas & steam turbine power plants.* (Pennwell Books, 2009).
9. Nicolosi, M. Wind power integration and power system flexibility–An empirical analysis of extreme events in Germany under the new negative price regime. *Energy Policy* **38,** 7257–7268 (2010).

10. Genoese, F., Genoese, M. & Wietschel, M. Occurrence of negative prices on the German spot market for electricity and their influence on balancing power markets. in *Energy Market (EEM), 2010 7th International Conference on the European* 1–6 (IEEE, 2010).

11. Paraschiv, F., Erni, D. & Pietsch, R. The impact of renewable energies on EEX day-ahead electricity prices. *Energy Policy* **73,** 196–210 (2014).

12. Fanone, E., Gamba, A. & Prokopczuk, M. The case of negative day-ahead electricity prices. *Energy Econ.* **35,** 22–34 (2013).

13. Forsberg, C. Hybrid systems to address seasonal mismatches between electricity production and demand in nuclear renewable electrical grids. *Energy Policy* **62,** 333–341 (2013).

14. Bartels, J. Supercritical pressure steam power cycles. in *Proceedings of the American Power Conference* **16,** 166 (Illinois Institute of Technology., 1954).

15. Henry, A. & Prasher, R. The prospect of high temperature solid state energy conversion to reduce the cost of concentrated solar power. *Energy Environ. Sci.* **7,** 1819–1828 (2014).

16. Bugge, J., Kjær, S. & Blum, R. High-efficiency coal-fired power plants development and perspectives. *Energy* **31,** 1437–1445 (2006).

17. U.S. Energy Information Administration. *International Energy Outlook 2016*. (2016).

18. Pioro, I. & Mokry, S. Thermophysical properties at critical and supercritical conditions. *Heat Transf. - Theor. Anal. Exp. Investig. Ind. Syst.* 573–592 (2011). doi:10.5772/13790

19. Iverson, B. D., Conboy, T. M., Pasch, J. J. & Kruizenga, A. M. Supercritical CO 2 Brayton cycles for solar-thermal energy. *Appl. Energy* **111,** 957–970 (2013).

20. Al-Sulaiman, F. A. & Atif, M. Performance comparison of different supercritical carbon dioxide Brayton cycles integrated with a solar power tower. *Energy* **82,** 61–71 (2015).
21. Weinstein, L. A. *et al.* Concentrating solar power. *Chem. Rev.* **115,** 12797–12838 (2015).
22. ECOFYS. *International Comparison of Fossil Power Efficiency and CO2 Intensity-Update 2015.* (2016).
23. Agency, I. E. & IEA. *Technology Roadmap High-Efficiency, Low-emissions Coal-Fired Power Generation.* (2013).
24. Platts. *World Electric Power Plants Database. S&P Global* (2016).
25. Board, I. E. A. C. I. A. *Regional Trends in Energy Efficient Coal-fired, Power Generation Technologies.* (OECD Publishing, 1998).
26. Beér, J. M. High efficiency electric power generation: The environmental role. *Prog. Energy Combust. Sci.* **33,** 107–134 (2007).
27. SIEMENS. *Siemens Power Generation in China.* (2007).
28. Ciais, P. *et al.* Attributing the increase in atmospheric CO2 to emitters and absorbers. *Nat. Clim. Chang.* **3,** 926–930 (2013).
29. Trenberth, K. E. *et al.* Global warming and changes in drought. *Nat. Clim. Chang.* **4,** 17–22 (2014).
30. Watson, R. T., Patz, J., Gubler, D. J., Parson, E. A. & Vincent, J. H. Environmental health implications of global climate change. *J. Environ. Monit.* **7,** 834–843 (2005).
31. Solomon, S., Plattner, G.-K., Knutti, R. & Friedlingstein, P. Irreversible climate change due to carbon dioxide emissions. *Proc. Natl. Acad. Sci.* pnas-0812721106 (2009).

32. Bao, J., Sherwood, S. C., Alexander, L. V & Evans, J. P. Future increases in extreme precipitation exceed observed scaling rates. *Nat. Clim. Chang.* **7,** 128–132 (2017).

33. Zhu, Z. *et al.* Greening of the Earth and its drivers. *Nat. Clim. Chang.* **6,** 791–795 (2016).

34. Fyfe, J. C. *et al.* Making sense of the early-2000s warming slowdown. *Nat. Clim. Chang.* **6,** 224–228 (2016).

35. Chu, S. & Majumdar, A. Opportunities and challenges for a sustainable energy future. *Nature* **488,** 294–303 (2012).

36. Jinke, L., Hualing, S. & Dianming, G. Causality relationship between coal consumption and GDP: difference of major OECD and non-OECD countries. *Appl. Energy* **85,** 421–429 (2008).

37. Ibrahim, H., Ilinca, a. & Perron, J. Energy storage systems-Characteristics and comparisons. *Renew. Sustain. Energy Rev.* **12,** 1221–1250 (2008).

38. Yang, Z. *et al.* Electrochemical energy storage for green grid. *Chem. Rev.* **111,** 3577–3613 (2011).

39. Dunn, B., Kamath, H. & Tarascon, J.-M. Electrical energy storage for the grid: A battery of choices. *Science (80-.).* **334,** 928–935 (2011).

40. Tesla. Tesla Powerpack. Available at: https://www.tesla.com/powerpack. (Accessed: 9th February 2017)

41. Vazquez, S., Lukic, S. M., Galvan, E., Franquelo, L. G. & Carrasco, J. M. Energy storage systems for transport and grid applications. *IEEE Trans. Ind. Electron.* **57,** 3881–3895 (2010).

42. Liu, J. *et al.* Materials science and materials chemistry for large scale electrochemical

energy storage: From transportation to electrical grid. *Adv. Funct. Mater.* **23,** 929–946 (2013).

43. Park, M., Sun, H., Lee, H., Lee, J. & Cho, J. Lithium-air batteries: Survey on the current status and perspectives towards automotive applications from a battery industry standpoint. *Adv. Energy Mater.* **2,** 780–800 (2012).

44. Fan, F. Y., Carter, W. C. & Chiang, Y. Mechanism and kinetics of Li2S precipitation in Lithium–Sulfur batteries. *Adv. Mater.* **27,** 5203–5209 (2015).

45. Nazar, L. F., Cuisinier, M. & Pang, Q. Lithium-sulfur batteries. *MRS Bull.* **39,** 436–442 (2014).

46. Kerestes, R. J., Reed, G. F. & Sparacino, A. R. Economic analysis of grid level energy storage for the application of load leveling. *IEEE Power Energy Soc. Gen. Meet.* 1–9 (2012). doi:10.1109/PESGM.2012.6345072

47. Ferreira, H. L., Garde, R., Fulli, G., Kling, W. & Lopes, J. P. Characterisation of electrical energy storage technologies. *Energy* **53,** 288–298 (2013).

48. Chen, H. *et al.* Progress in electrical energy storage system: A critical review. *Prog. Nat. Sci.* **19,** 291–312 (2009).

49. Li, G. *et al.* An advanced Na-FeCl2 ZEBRA battery for stationary energy storage application. *Adv. Energy Mater.* n/a-n/a (2015). doi:10.1002/aenm.201500357

50. Zhang, J., Chen, C., Zhang, X. & Liu, S. Study on the environmental risk assessment of Lead-acid batteries. *Procedia Environ. Sci.* **31,** 873–879 (2016).

51. Kousksou, T., Bruel, P., Jamil, a., El Rhafiki, T. & Zeraouli, Y. Energy storage: Applications and challenges. *Sol. Energy Mater. Sol. Cells* **120,** 59–80 (2014).

52. Tokuda, N. *et al.* Development of a redox flow battery system. *Sei Tech Rev* 88–94 (1998).

53. Soloveichik, G. L. Battery technologies for large-scale stationary energy storage. *Annu. Rev. Chem. Biomol. Eng.* **2,** 503–527 (2011).

54. Prudent Energy, China; Previously VRB Power Systems, Inc.

55. Duduta, M. *et al.* Semi-Solid lithium rechargeable flow battery. *Adv. Energy Mater.* **1,** 511–516 (2011).

56. Desmond Ng, J. W., Gorlin, Y., Hatsukade, T. & Jaramillo, T. F. A precious-metal-free regenerative fuel cell for storing renewable electricity. *Adv. Energy Mater.* **3,** 1545–1550 (2013).

57. Dresselhaus, M. S. & Thomas, I. L. Alternative energy technologies. *Nature* **414,** 332–337 (2001).

58. Boom, R. W. Superconductive magnetic energy storage for electric utilities-a review of the 20 year Wisconsin program. in *Power Sources Symposium, 1990., Proceedings of the 34th International* 1–4 (IEEE, 1990).

59. Zhu, J. *et al.* Design, dynamic simulation and construction of a hybrid HTS SMES (high-temperature superconducting magnetic energy storage systems) for Chinese power grid. *Energy* **51,** 184–192 (2013).

60. Akhavan, M., Jensen, J. & Kitazawa, K. *Magnetic and Superconducting Materials.* (World Scientific Publishing Company, 2000).

61. Sebastián, R. & Peña Alzola, R. Flywheel energy storage systems: Review and simulation for an isolated wind power system. *Renew. Sustain. Energy Rev.* **16,** 6803–

6813 (2012).

62. Evans, A., Strezov, V. & Evans, T. J. Assessment of utility energy storage options for increased renewable energy penetration. *Renew. Sustain. Energy Rev.* **16,** 4141–4147 (2012).

63. Mahlia, T. M. I., Saktisahdan, T. J., Jannifar, a., Hasan, M. H. & Matseelar, H. S. C. A review of available methods and development on energy storage; Technology update. *Renew. Sustain. Energy Rev.* **33,** 532–545 (2014).

64. Hameer, S. & Niekerk, J. A review of large-scale electrical energy storage. *Int. J. energy Res.* 117901195 (2015). doi:10.1002

65. Datas, A., Ramos, A., Martí, A., del Cañizo, C. & Luque, A. Ultra high temperature latent heat energy storage and thermophotovoltaic energy conversion. *Energy* **107,** 542–549 (2016).

66. Seyf, H. R. & Henry, A. Thermophotovoltaics: a potential pathway to high efficiency concentrated solar power. *Energy Environ. Sci.* **9,** 2654–2665 (2016).

67. Gasanaliev, A. M. & Gamataeva, B. Y. Heat-accumulating properties of melts. *Russ. Chem. Rev.* **69,** 179–186 (2000).

68. Brady, L. E. Apparatus for utilizing the current force of water. (1885).

69. Washington, B. C. Water-power electrical plants in the United States. *J. Franklin Inst.* **148,** 161–181 (1899).

70. Ceder, G. *et al.* Identification of cathode materials for lithium batteries guided by first-principles calculations. *Nature* **392,** 694–696 (1998).

71. Bruce, P. G., Freunberger, S. a., Hardwick, L. J. & Tarascon, J.-M. Li–O2 and Li–S batteries

with high energy storage. *Nat. Mater.* **11,** 172–172 (2011).

72. Palomares, V. *et al.* Na-ion batteries, recent advances and present challenges to become low cost energy storage systems. *Energy Environ. Sci.* **5,** 5884–5901 (2012).

73. Xu, N., Li, X., Zhao, X., Goodenough, J. B. & Huang, K. A novel solid oxide redox flow battery for grid energy storage. *Energy Environ. Sci.* **4,** 4942 (2011).

74. Alotto, P., Guarnieri, M. & Moro, F. Redox flow batteries for the storage of renewable energy: A review. *Renew. Sustain. Energy Rev.* **29,** 325–335 (2014).

75. Li, Y. & Dai, H. Recent advances in zinc–air batteries. *Chem. Soc. Rev.* **43,** 5257–5275 (2014).

76. Kearney, D. *et al.* Overview on use of a molten salt HTF in a trough solar field. *NREL Parabol. Trough Therm. Energy Storage Work.* (2003).

77. Stekli, J., Irwin, L. & Pitchumani, R. Technical challenges and opportunities for concentrating solar power with thermal energy storage. *J. Therm. Sci. Eng. Appl.* **5,** 21011 (2013).

78. Zanganeh, G., Pedretti, a., Zavattoni, S., Barbato, M. & Steinfeld, a. Packed-bed thermal storage for concentrated solar power – Pilot-scale demonstration and industrial-scale design. *Sol. Energy* **86,** 3084–3098 (2012).

79. Tian, Y. & Zhao, C.-Y. A review of solar collectors and thermal energy storage in solar thermal applications. *Appl. Energy* **104,** 538–553 (2013).

80. Slocum, A. H. *et al.* Concentrated solar power on demand. *Sol. Energy* **85,** 1519–1529 (2011).

81. Arteconi, A., Hewitt, N. J. & Polonara, F. State of the art of thermal storage for demand-

side management. *Appl. Energy* **93,** 371–389 (2012).

82. Hasnain, S. M. Review on sustainable thermal energy storage technologies, Part I: heat storage materials and techniques. *Energy Convers. Manag.* **39,** 1127–1138 (1998).

83. Zhang, Y., Zhou, G., Lin, K., Zhang, Q. & Di, H. Application of latent heat thermal energy storage in buildings: State-of-the-art and outlook. *Build. Environ.* **42,** 2197–2209 (2007).

84. Dincer, I. On thermal energy storage systems and applications in buildings. *Energy Build.* **34,** 377–388 (2002).

85. Hamburg. Siemens presents thermal storage solution for wind energy. (2016).

86. 1414degrees. Available at: http://1414degrees.com.au/.

87. Forsberg, C. W. Sustainability by combining nuclear, fossil, and renewable energy sources. *Prog. Nucl. energy* **51,** 192–200 (2009).

88. International Energy Agency. Power Generation from Coal. *Power Gener. from coal* (2010).

89. Aptech, I., Kumar, N., Peter, B., Lefton, S. & Agan Dimo. Power plant cycling costs. *Contract* **303,** 275–3000 (2012).

90. Operator, N. Y. I. S. *NYISO Real-Time Market LBMP.* (2017).

91. Bradbury, K., Pratson, L. & Patiño-Echeverri, D. Economic viability of energy storage systems based on price arbitrage potential in real-time US electricity markets. *Appl. Energy* **114,** 512–519 (2014).

92. Jean, J., Brown, P. R., Jaffe, R. L., Buonassisi, T. & Bulović, V. Pathways for solar photovoltaics. *Energy Environ. Sci.* **8,** 1200–1219 (2015).

93. Dincer, F. The analysis on photovoltaic electricity generation status, potential and policies of the leading countries in solar energy. *Renew. Sustain. Energy Rev.* **15,** 713–720 (2011).

94. Kurokawa, K. *Energy from the Desert: Feasability of Very Large Scale Power Generation (VLS-PV).* (Routledge, 2014).

95. Shah, R., Mithulananthan, N., Bansal, R. C. & Ramachandaramurthy, V. K. A review of key power system stability challenges for large-scale PV integration. *Renew. Sustain. Energy Rev.* **41,** 1423–1436 (2015).

96. U.S. Energy Information Administration. *Power Plant Operations.* (2016).

97. Braff, W. A., Mueller, J. M. & Trancik, J. E. Value of storage technologies for wind and solar energy. *Nat. Clim. Chang.* **6,** 964–969 (2016).

98. Liu, Z. Y. *Annual report on the development of China's electric power industry.* (2011).

99. Xu, G. *et al.* Techno-economic analysis and optimization of the heat recovery of utility boiler flue gas. *Appl. Energy* **112,** 907–917 (2013).

100. Fernandes, D., Pitié, F., Cáceres, G. & Baeyens, J. Thermal energy storage: 'How previous findings determine current research priorities'. *Energy* **39,** 246–257 (2012).

101. Valencia, J. J. & Quested, P. N. Thermophysical Properties. (2013).

102. Wang, X., Liu, J., Zhang, Y., Di, H. & Jiang, Y. Experimental research on a kind of novel high temperature phase change storage heater. *Energy Convers. Manag.* **47,** 2211–2222 (2006).

103. Yamasue, E., Susa, M., Fukuyama, H. & Nagata, K. Thermal conductivities of silicon and germanium in solid and liquid states measured by non-stationary hot wire method

with silica coated probe. *J. Cryst. Growth* **234,** 121–131 (2002).

104. (Ltd), S. P. Southern Africa Analysis and Smelting. Available at: http://southernas.com/.

105. Jang, B. Y., Kim, J. S. & Ahn, Y. S. Induction melting process using segmented graphite crucible for silicon melting. *Sol. Energy Mater. Sol. Cells* **95,** 101–106 (2011).

106. Kimura, H. S. and A. I. and K. T. and S. Temperature dependence of the electrical resistivity of molten silicon. *Jpn. J. Appl. Phys.* **34,** 3426 (1995).

107. Iwai, K., Tamaoki, R., Sassa, K. & Asai, S. Development of an induction melting process for materials with low electrical conductivity or high melting point. *Metall. Mater. Trans. B* **24,** 259–264 (1993).

108. Alemany, C., Trassy, C., Pateyron, B., Li, K.-I. & Delannoy, Y. Refining of metallurgical-grade silicon by inductive plasma. *Sol. energy Mater. Sol. cells* **72,** 41–48 (2002).

109. Mühlbauer, A. Innovative induction melting technologies: A historical review. in *International Scientific Colloquium, Modelling for Material Processing* 13–20 (2006).

110. Carter, C. B. & Norton, M. G. *Ceramic materials: science and engineering*. (Springer Science & Business Media, 2007).

111. White, J. F., Ma, L., Forwald, K. & Sichen, D. Reactions between silicon and graphite substrates at high temperature: In situ observations. *Metall. Mater. Trans. B* **45,** 150–160 (2014).

112. Ciftja, A. Wettability of silicon with refractory materials: A review. (2008).

113. Eustathopoulos, N. Wetting by liquid metals—application in materials processing: The contribution of the Grenoble group. *Metals (Basel).* **5,** 350–370 (2015).

114. Deike, R. & Schwerdtfeger, K. Reactions between liquid silicon and different refractory materials. *J. Electrochem. Soc.* **142,** 609–614 (1995).

115. Stoddard, N., Wu, B., Maisano, L., Russell R., C. & Fernandez, J. M. 18th Workshop on Crystalline Silicon Solar Cells & Modules: Materials and Processes. *Lead. Edge Silicon Cast. Technol. BP Solar's Mono2 Wafers* 7–14 (2008).

116. Stølen, S. & Grande, T. *Chemical thermodynamics of materials: macroscopic and microscopic aspects.* (John Wiley & Sons, 2004).

117. Dezellus, O., Jacques, S., Hodaj, F. & Eustathopoulos, N. Wetting and infiltration of carbon by liquid silicon. *J. Mater. Sci.* **40,** 2307–2311 (2005).

118. Li, J. & Hausner, H. Reactive wetting in the liquid-silicon/solid-carbon system. *J. Am. Ceram. Soc.* **79,** 873–880 (1996).

119. Qian, W. Y. *et al.* pH-sensitive strontium carbonate nanoparticles as new anticancer vehicles for controlled etoposide release. *Int. J. Nanomedicine* **7,** 5781–5792 (2012).

120. Margiotta, J. C., Zhang, D., Nagle, D. C. & Feeser, C. E. Formation of dense silicon carbide by liquid silicon infiltration of carbon with engineered structure. *J. Mater. Res.* **23,** 1237–1248 (2008).

121. Fu, Z., Wang, C., Tang, C., Zhao, H. & Robin, J.-C. Oxidation behaviors of SiO2/SiC coated matrix graphite of high temperature gas-cooled reactor fuel element. *Nucl. Eng. Des.* **265,** 867–871 (2013).

122. Zhu, Q., Qiu, X. & Ma, C. Oxidation resistant SiC coating for graphite materials. *Carbon N. Y.* **37,** 1475–1484 (1999).

123. Chunhe, T. & Jie, G. Improvement in oxidation resistance of the nuclear graphite by

reaction-coated SiC coating. *J. Nucl. Mater.* **224,** 103–108 (1995).

124. Fu, Q.-G., Li, H.-J., Shi, X.-H., Li, K.-Z. & Sun, G.-D. Silicon carbide coating to protect carbon/carbon composites against oxidation. *Scr. Mater.* **52,** 923–927 (2005).

125. Viswanathan, R., Sarver, J. & Tanzosh, J. M. Boiler materials for ultra-supercritical coal power plants—steamside oxidation. *J. Mater. Eng. Perform.* **15,** 255–274 (2006).

126. Xiaowei, L., Jean-Charles, R. & Suyuan, Y. Effect of temperature on graphite oxidation behavior. *Nucl. Eng. Des.* **227,** 273–280 (2004).

127. De Lucia, M. & Bejan, A. Thermodynamics of energy storage by melting due to conduction or natural convection. *heat-transfer* **1000,** s2 (1990).

128. Lim, J. S., Bejan, A. & Kim, J. H. Thermodynamic optimization of phase-change energy storage using two or more materials. *J. Energy Resour. Technol.* **114,** 84–90 (1992).

129. Bejan, A. *Entropy generation minimization: the method of thermodynamic optimization of finite-size systems and finite-time processes.* (CRC press, 1995).

130. Bellecci, C. & Conti, M. Transient behaviour analysis of a latent heat thermal storage module. **36,** (1993).

131. He, Q. & Zhang, W. N. A study on latent heat storage exchangers with high temperature PCM. *World Renew. Energy Congr. VI* 1044–1047 (2000). doi:10.1002/er.683

132. Kotzé, J. P., von Backström, T. W. & Erens, P. J. Simulation and testing of a latent heat thermal energy storage unit with metallic phase change material. *Energy Procedia* **49,** 860–869 (2014).

133. Fortunato, B., Camporeale, S. M., Torresi, M. & Albano, M. Simple mathematical model of a thermal storage with PCM. *AASRI Procedia* **2,** 241–248 (2012).

134. Genium, P. Vaporization/Phase Change, Freezing: introduction, applications, and basic physical concepts. (1996).

135. Olson, D. A., Glicksman, L. R. & Ferm, H. M. Steady-state natural convection in empty and partitioned enclosures at high rayleigh numbers. *J. Heat Transfer* **112,** 640–647 (1990).

136. Bohn, M. S., Kirkpatrick, A. T. & Olson, D. A. Experimental study of three-dimensional natural convection high-Rayleigh number. *J. Heat Transfer* **106,** 339–345 (1984).

137. Neuer, G. Spectral and total emissivity measurements of highly emitting materials. *Int. J. Thermophys.* **16,** 257–265 (1995).

138. Sridharan, K., Allen, T., Anderson, M., Cao, G. & Kulcinski, G. *Emissivity of Candidate Materials for VHTR Applicationbs: Role of Oxidation and Surface Modification Treatments.* (University of Wisconsin, 2011).

139. Howell, J. R., Menguc, M. P. & Siegel, R. *Thermal radiation heat transfer.* (CRC press, 2010).

140. Li, C. Y. & Yan, W. P. The numerical calculation and analysis of burner zone membrane water-wall temperature field of a 600MW supercritical boiler under various operating conditions. in *Advanced Materials Research* **163,** 664–669 (Trans Tech Publ, 2011).

141. Williams, R. K., Graves, R. S. & McElroy, D. L. Thermal and electrical conductivities of an improved 9 Cr-1 Mo steel from 360 to 1000 K. *Int. J. Thermophys.* **5,** 301–313 (1984).

142. Petukhov, B. S. Heat transfer and friction in turbulent pipe flow with variable physical properties. *Adv. heat Transf.* **6,** 503–564 (1970).

143. Filonienko, G. K. Friction factor for turbulent pipe flow. *Teploenergetika* **1,** 40–44 (1954).

144. Mokry, S. *et al.* Development of supercritical water heat-transfer correlation for vertical bare tubes. *Nucl. Eng. Des.* **241,** 1126–1136 (2011).

145. Swank, W. D., Valentin, F. I., Kawaji, M. & McEligot, D. M. Thermal conductivity of G-348 isostatic graphite. *Nucl. Technol.* 1–7 (2017).

146. Lundqist, R., Schrief, A., Kinnunen, P., Myöhänen, K. & Seshamani, M. A major step forward—the supercritical CFB boiler. *PowerGen Int. 2003Las Vegas, NV* 1–22 (2003).

147. Gladstone, C. & Woods, A. W. On buoyancy-driven natural ventilation of a room with a heated floor. *J. Fluid Mech.* **441,** 293–314 (2001).

148. Linden, P. F. The fluid mechanics of natural ventilation. *Annu. Rev. Fluid Mech.* **31,** 201–238 (1999).

149. Li, Y., Sandberg, M. & Fuchs, L. Effects of thermal radiation on airflow with displacement ventilation: an experimental investigation. *Energy Build.* **19,** 263–274 (1993).

150. Mundt, E. Displacement ventilation systems—Convection flows and temperature gradients. *Build. Environ.* **30,** 129–133 (1995).

151. Batchelor, G. K. 1967 An Introduction to Fluid Dynamics. (1970).

152. Awbi, H. B. & Hatton, A. Natural convection from heated room surfaces. *Energy Build.* **30,** 233–244 (1999).

153. Novoselac, A., Burley, B. J. & Srebric, J. Development of new and validation of existing convection correlations for rooms with displacement ventilation systems. *Energy*

Build. **38,** 163–173 (2006).

154. MorganAdvancedMaterials. *WDS Ultra*.
155. BNZ Materials, I. IFB 2660.
156. Pirasaci, T. & Goswami, D. Y. Influence of design on performance of a latent heat storage system for a direct steam generation power plant. *Appl. Energy* **162,** 644–652 (2016).
157. Kotzé, J., Backstrom, T. Von & Erens, P. Evaluation of a latent heat thermal energy storage system using AlSi12 as a phase change material. *Marrakesch: SolarPACES* 1–7 (2012).
158. Kotzé, J., Backström, T. Von & Erens, P. A combined latent thermal energy storage and steam generator concept using metallic phase change materials and metallic heat transfer fluids for concentrated solar power. (2011).
159. Kotzé, J. P., von Backström, T. W. & Erens, P. J. High temperature thermal energy storage utilizing metallic phase change materials and metallic heat transfer fluids. *J. Sol. Energy Eng.* **135,** 35001–35006 (2013).
160. Medrano, M., Gil, A., Martorell, I., Potau, X. & Cabeza, L. F. State of the art on high-temperature thermal energy storage for power generation. Part 2-Case studies. *Renew. Sustain. Energy Rev.* **14,** 56–72 (2010).
161. Laing, D., Bahl, C., Bauer, T., Lehmann, D. & Steinmann, W.-D. Thermal energy storage for direct steam generation. *Sol. Energy* **85,** 627–633 (2011).
162. Gil, A. *et al.* State of the art on high temperature thermal energy storage for power generation. Part 1-Concepts, materials and modellization. *Renew. Sustain. Energy Rev.*

14, 31–55 (2010).

163. Winter, C.-J., Sizmann, R. L. & Vant-Hull, L. L. *Solar power plants: fundamentals, technology, systems, economics.* (Springer Science & Business Media, 2012).
164. Pfleger, N., Bauer, T., Martin, C., Eck, M. & Wörner, A. Thermal energy storage - overview and specific insight into nitrate salts for sensible and latent heat storage. *Beilstein J. Nanotechnol.* **6,** 1487–1497 (2015).
165. Kuravi, S., Trahan, J., Goswami, D. Y., Rahman, M. M. & Stefanakos, E. K. Thermal energy storage technologies and systems for concentrating solar power plants. *Prog. Energy Combust. Sci.* **39,** 285–319 (2013).
166. Herrmann, U., Kelly, B. & Price, H. Two-tank molten salt storage for parabolic trough solar power plants. *Energy* **29,** 883–893 (2004).
167. Anderson, J. Determining manufacturing costs. *Chem. Eng. Prog.* **105,** 27–31 (2009).
168. Tuck, A. C. 2016 USGS Minerals Resources Program. (2016).
169. Supply, O. WATLOW Cartridge Heaters.
170. Focus Economics. Alumina Price Outlook. Available at: www.focus-economics.com/commodities/base-metals/alumina.
171. MEPS. World Carbon Steel Prices.
172. Aesteiron Steel Pipes. Available at: http://aesteironsteelpipes.com/99-astm-a335-p92-alloy-steel-pipe. (Accessed: 9th February 2017)